Design and implementation of a high strain rate biaxial tension test for elastomeric materials and biological soft tissue

Aaron Graham

Submitted to the University of Cape Town
in partial fulfilment of the degree of
MSc in Mechanical Engineering

February 2019

Declaration

I, Aaron Graham , hereby:

(a) grant the University of Cape Town free license to reproduce the above thesis in whole or in part, for the purpose of research;

(a) declare that:

(i) the above thesis is my own unaided work, both in concept and execution, and that apart from the normal guidance from my supervisor, I have received no assistance apart from that explicitly stated in the Acknowledgements.

(i) I know the meaning of plagiarism and declare that all the work in the document, save for that which is properly acknowledged, is my own. This thesis/dissertation has been submitted to the Turnitin module (or equivalent similarity and originality checking software) and I confirm that my supervisor has seen my report and any concerns revealed by such have been resolved with my supervisor

(i) neither the substance nor any part of the above thesis has been submitted in the past, or is being, or is to be submitted for a degree at this University or at any other university.

I am now presenting the report for examination for the degree of M.Sc Eng (Mechanical) .

Signed by candidate

A.M. Graham

08 Feb 2019

Abstract

The mechanical properties of biological tissues are of increasing research interest to disciplines as varied as designers of protective equipment, medical researchers and even forensic Finite Element Analysis (FEA). The mechanical properties of biological tissue such as skin are relatively well known at low strain rates and strains, but there is a paucity of data on the high rate, high strain behaviour of skin - particularly under biaxial tension. Biaxial tensile loading mimics *in vivo* conditions more closely than uniaxial loading [1, 2], and is necessary in order to characterise a hyper-elastic material model[3]. Furthermore, biaxial loading allows one to detect the anisotropy of the sample without introducing noise from inter-sample variability - unlike uniaxial tensile testing.

This work develops a high strain rate bulge test device capable of testing soft tissue or polymer membranes at high strain rates. The load history as well as the full field displacement data is captured via a pressure transducer and high speed 3D Digital Image Correlation (DIC). Strain rates ranging from $0.26s^{-1}$ to $827s^{-1}$ are reliably achieved and measured. Higher strain rates of up to $2500s^{-1}$ are achieved, but are poorly measured due to equipment limitations of the high speed cameras used. The strain rates achieved had some variability, but were significantly more consistent than those achieved by high rate biaxial tension tests found in the literature. In addition to control of the apex strain rate, the bi-axial strain ratio is controlled via the geometry of the specimen fixture. This allowed for strain ratios of up to 2 to be achieved at the apex [1]. When testing anisotropic membranes, the use of full field 3D DIC allowed for accurate and efficient detection of the principal axis of anisotropy in the material.

No skin is tested, but instead three types of polydimethylsiloxane (PDMS, "silicone') skin simulant are tested. These simulants were chosen to fully encapsulate the range of mechanical behaviour expected from skin - they were chosen to have stiffness's, strain hardening exponents and degrees of anisotropy significantly above or below the behaviour exhibited by skin. This ensured that the device was validated over a wider range of conditions than expected when testing skin. A novel approach to specimen fixation and speckling for silicone membranes is developed, as well as a fibre reinforced skin simulant that closely mimics the rate hardening and anisotropic behaviour of skin. In addition to bulge tests, uniaxial tensile tests are conducted on the various simulant materials in order to characterise their low strain rate behaviour. The composite skin simulant is characterised using a modified version of the anisotropic skin model developed by Weiss *et al* (1996) [4], and the pure silicone membranes are characterised using the Ogden hyper-elastic model.

[1] i.e. the strain in the xx direction could be up to double the strain in the yy direction

Acknowledgements

My sincere gratitude goes to:

Dr Reuben Govender, my supervisor. He allowed me a great deal of independence in this project, for which I am grateful.

Mr Trevor Cloete, my co-supervisor. He was always willing to discuss ideas, no matter how impractical or off-topic. I greatly enjoyed our wide-ranging talks, and appreciate his openness to discussion on any topic.

Mr Pierre Smith and the workshop staff. For both my final year project and my MSc. project I submitted designs that required a large amount of difficult machining, and the workshop did an excellent job both times. Pierre always provided helpful advice, and this project could not have gone ahead without him and his staff.

The CERECAM staff and students[2], for always providing a welcoming environment to someone from another research group. A lot of my write-up and simulation was done there, and I cherish the discussions and advice that I got at CERECAM.

The BISRU (and EPPI) staff and students[3]. For helping with experiments, as well as providing banter and a sympathetic ear when things went wrong.

My parents, for never losing faith and always providing support and encouragement whenever required.

My E2 flatmates: for providing endless motivation, advice, inspiration and draft review. Particularly during the final stretch, your contributions were incredibly valuable

Freda, my girlfriend. For the encouragement, laughter, early morning runs and amazing company. For always being there to listen to the more technical points of my dissertation, even if they didn't make sense. For giving me valuable perspective, and keeping me company during late night writing sessions. Without you, this dissertation would have turned out very differently.

[2]Heidi and Dane in particular
[3]Dustin in particular

Contents

List of Figures

List of Tables

Direction and Naming Convention

List of Symbols and Abbreviations

Symbol	Description	Units
$\boldsymbol{X}$	Undeformed position (material/Lagrangian co-ordinate)	m
$\boldsymbol{x}$	Current position (spatial/Eulerian co-ordinate), and a function of $\boldsymbol{X}$ and t	m
$\boldsymbol{u}$	Displacement field ($\boldsymbol{x} - \boldsymbol{X}$)	m
$\boldsymbol{F}$	Deformation gradient, $\frac{\boldsymbol{\partial x}}{\boldsymbol{\partial X}}$	unitless
$\boldsymbol{C}$	Right Cauchy-Green deformation tensor ($\boldsymbol{F^T \cdot F}$)	unitless
$\boldsymbol{B}$	Left Cauchy-Green deformation tensor ($\boldsymbol{F \cdot F^T}$)	unitless
λ_i	i^{th} principal stretch (1+strain)	unitless
J	Volumetric strain ratio, det($\boldsymbol{F}$)	unitless
$\boldsymbol{T}$ or $\boldsymbol{\sigma}$	Cauchy stress. Stress in the spatial description, also known as "true stress". Note that many texts use $\boldsymbol{T}$ to refer to the Biot Stress, but in this dissertation $\boldsymbol{T}$ refers to the Cauchy stress	Pa
$\boldsymbol{P}$	First Piola-Kirchhoff stress. Also known as "engineering stress" or "nominal stress"	Pa
$\boldsymbol{S}$	Second Piola-Kirchhoff stress. Equal to the first Piola-Kirchoff stress pulled back to the reference configuration by $\boldsymbol{F}^{-1}$	Pa
$\dot{\phi}$	Rate of change of ϕ with time, $\frac{\partial \phi}{\partial t}$. ϕ being a generic quantity (mass, velocity, energy etc)	ϕ/s
$\ddot{\phi}$	Rate of change of $\dot{\phi}$ with time, $\frac{\partial^2 \phi}{\partial t^2}$	ϕ/s^2
E_Y	Young's modulus/Elastic modulus	Pa
μ	Shear modulus	Pa
ν	Poisson's ratio	unitless

Symbols that are in bold represent tensor quantities, and symbols that are not in bold represent scalar quantities.

Chapter 1

Introduction

1.1 Motivation

The mechanical properties of biological tissues are of increasing research interest:

> Designers of vehicles and protective gear include numerical models of humans in simulations of car crashes and other impact events. These simulations are used to improve the design of protective equipment, decreasing injury to the occupant or user of the equipment. Accurate material characteristics increase the validity of these simulations, improving the design of the protective gear.
>
> Increasing computational power is making forensic Finite Element Analysis (FEA) more feasible [5, 6]. Most forensic cases involve accidents, assaults or homicides - instances where damage to biological tissue is likely to have occurred at high strain rates.
>
> Medical research is making increasing use of computational simulation of the human body to understand diseases and injuries. Mechanical properties of human tissue are needed in order to accurately model how the body responds to loads.

Whilst the mechanical properties of biological tissue such as skin are well known at low strain rates and strains, there has been relatively little research done into high strain rate mechanical properties of skin. High strain rate testing of skin has tended to focus on uniaxial tensile tests, which have the advantage of being easy to conduct but poorly emulate *in vivo* conditions.

A review of the relevant literature highlighted the limited quasi-static biaxial tensile data on skin, and the lack of high strain rate biaxial tensile data.

1.2 Objectives

The objective of this dissertation is to develop a high strain rate (10 s^{-1} - 100 s^{-1}) biaxial tensile test apparatus and methodology. At a minimum, the apparatus should be capable of achieving strain rates of $10 - 100s^{-1}$ in membranes of elastomeric materials and biological soft tissue such as skin. If possible, it is desirable that the device be capable of achieving strain rates outside of this envelope in addition.

This methodology should be capable of characterising the membrane material's mechanical properties, including anisotropy and rate dependant effects.

1.3 Scope

No actual biological tissue (from human or animal sources) will be tested, and skin simulants such as silicone elastomers will be used for development of the test methodology and apparatus.

Only high strain rate bulge testing will be done, as this dissertation is part of a larger research project at BISRU. Quasi-static and intermediate rate bulge test apparatus are being concurrently designed by two other students as part of their MSc. dissertations. Future students will then use these designed devices and methodologies to test human and animal skin over a wide range of strains and strain rates.

The primary focus of this dissertation is experimental, and only limited numerical work will be done. Numerical simulations are done in order to aid in device design and improve understanding of experimental results.

1.4 Dissertation outline

A review of the relevant literature is conducted, with a focus on biaxial tensile testing and measurement of high strain rate tests in soft biological tissues and elastomeric materials.

The design of the apparatus is described, as well as the specimen preparation method. The experimental methodology is described in detail, as is the numerical modelling of the experiments.

The results are shown, and conclusions are drawn. A significant number of appendices are included - these appendices either provide greater detail to sections covered in the body of this report, or detail interesting results that are tangential to the body of this report.

Chapter 2

Literature Review

Contents

2.1 Introduction

Skin is a highly complex non-linear biological material. Skin has to be tough enough to protect the body from physical attack (abrasion, puncture, tearing etc), pliable enough to allow for free movement, impermeable enough to protect from biological attack, all whilst allowing for thermoregulation. As a result, skin is a non-linear, anisotropic material - pliant at low strains, increasingly stiff at high strains, anisotropic, highly tear resistant and nearly incompressible.

Skin is primarily made up of collagen and elastin fibres, with the collagen fibres providing the vast majority of the skin's strength [1], whilst elastin provides stiffness at low strains. Approximately 75% of skin's dry mass is made up of collagen fibres [7]. As with most biological tissues, the properties of skin vary significantly with age, subject and site on subject [8]. This (coupled with difficulty in obtaining test samples) makes the mechanical properties of skin particularly challenging to test.

2.2 Mechanical properties of skin

2.2.1 Anisotropy

Skin has lines of natural tension known as Langer's lines (after C. Langer, who discovered them in 1861). Langer's lines were discovered by piercing a cadaver with a circular awl - the circular holes distort to become elliptical, with the major axis of the ellipse being parallel to the direction of maximum tension in the skin [9].
Langer's lines have a strong influence on the anisotropy of skin, as the collagen fibres preferentially orient in the direction of Langer's lines. As a result, skin is stiffer, stronger and tougher in the direction of Langer's lines [10]. Additionally, it has been found that cuts (such as from a surgeon's knife) heal better when made parallel to Langer's lines [11].

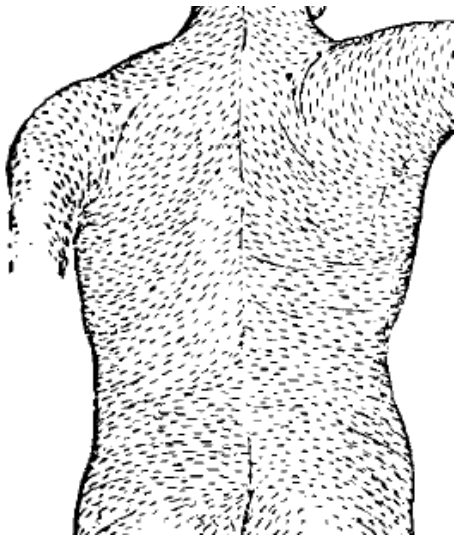

Figure 2.1 Langer's lines on a human back [9]

Uniaxial tensile tests of skin typically test for and quantify this anisotropy via a series of tests at 0, 45 and 90 degrees to Langer's lines [12], but a variety of other methods such as the crucifix biaxial tension test and the bulge test have been used [1].

Tonge *et al* (2014) directly measured the anisotropy of a series of skin samples, and found that the stiffness ratio was 1.35 ± 0.37 at low strains, and 4.42 ± 4.59 at high strains. Note the high degree of variability, particularly at high strains.

2.2.2 Non-linearity

In the relaxed state, the collagen fibres in skin are coiled and highly curved. The collagen fibres are initially loaded primarily in bending, leading to low initial macroscopic tensile stiffness. As the macroscopic strain increases, the collagen fibres gradually straighten out, transitioning from being loaded in bending to being loaded in direct tension. As a result, the tensile stiffness of skin increases greatly with strain.

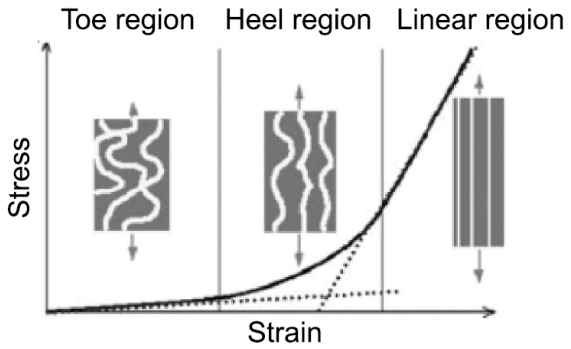

Figure 2.2 Stress strain curve for generic collagenous fibre[1]

Figures 2.2 and 2.3 show the stress strain curve for skin, with 3 distinct regions. In the toe region, the collagen fibres are still highly coiled, and loaded almost entirely in bending. As a result, the majority of the load is taken by the elastin fibres, and the stress:strain relationship is fairly linear - this apparent modulus is shown by line D. In the heel region, the collagen fibres are starting to straighten, and transition from being loaded primarily in bending to being loaded primarily in tension. This region is a non-linear transition from the toe region to the linear region. In the linear region, the collagen fibres have straightened out, and are loaded in direct tension. The macroscopic loading is almost entirely borne by the collagen fibres, with little stiffness due to the elastin - the apparent modulus of this region is shown by line B. In fig. 2.3 the transition from toe to heel region and heel to linear region occurs at approximately 10% and 35% strain respectively.

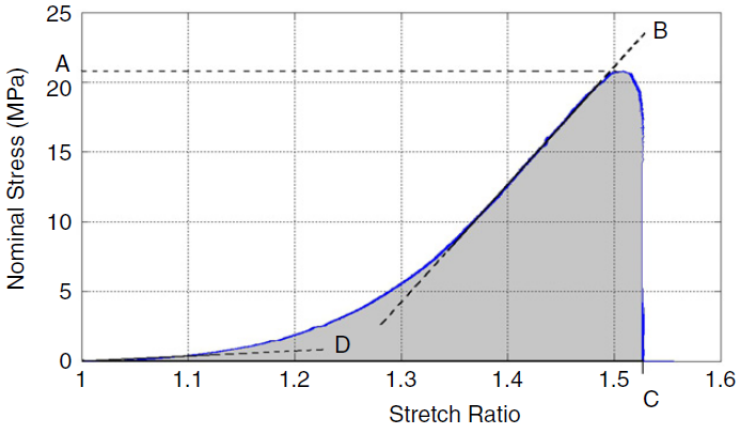

Figure 2.3 Typical stress stretch graph for uniaxial tension tests on human skin conducted by Gilchrist *et al* (2012) [13].

2.2.2.1 Re-alignment of collagen fibres

When under tensile strain, the collagen fibres in skin re-orient themselves to be parallel to the direction of maximum strain. This has several effects, one of which is the remarkable tear resistance of skin, and potentially the preconditioning effects observed in uniaxial tensile tests [14].

2.2.2.2 Preconditioning of test samples

In order to achieve consistent test results, skin samples have to undergo light ($\approx 3\%$ of UTS) cyclic loading prior to testing for both uniaxial tension tests and typical biaxial tension tests.

Figure 2.4 shows the test protocol used by [12] for uniaxial tensile tests of skin. Note step 6, the preconditioning by cyclic loading.

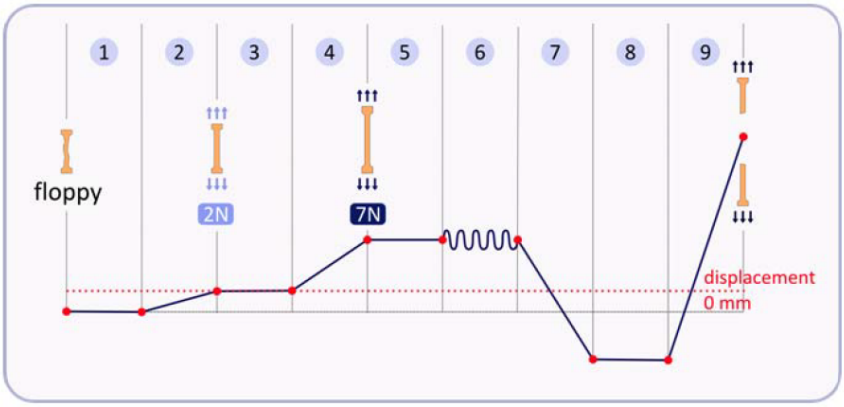

Figure 2.4 Test protocol for uniaxial tension test of skin by Gilchrist [12]. Note step 6, to minimise the variability due to preconditioning

The reason for the preconditioning effect is possibly the realignment of collagen fibres in the direction of tension[1]. Yang *et al* (2015) showed that the collagen fibres in skin under uniaxial tension undergo significant realignment in the direction of tension - the same property that gives skin its remarkable tear resistance[14] . Whilst both uniaxial and typical biaxial tension tests suffer from preconditioning effects, Tonge *et al* (2014) [1] showed that bulge testing of skin does not suffer from preconditioning effects. The reason for this is thought to be the constraining effect of the bulge test clamp mechanism, preventing re-alignment of collagen fibres at low strains. This mimics *in vivo* conditions more closely than typical uniaxial (or biaxial) tension tests.

The lack of preconditioning effects (and better simulation of *in vivo* conditions) is an important feature of bulge tests of skin - the primary purpose of mechanical testing of skin is ultimately to measure the *in vivo* properties of skin. This requires that the test methodology emulates the *in vivo* conditions of skin as closely as possible.

2.2.2.3 Tear resistance of skin

As a result of the re-alignment of collagen fibres in skin under strain, it is almost impossible to propagate a tear in skin [14]. The collagen fibres re-orient in the direction of the maximum tension, greatly increasing the stiffness in the direction of maximum tension and decreasing the stiffness in the transverse direction. As a result, the crack tip radius blunts rather than propagating, decreasing the stress concentration of the tear. This realignment is thought to occur during simple uniaxial tensile testing, resulting in greater UTS values than would be found during bulge testing or *in vivo* conditions.

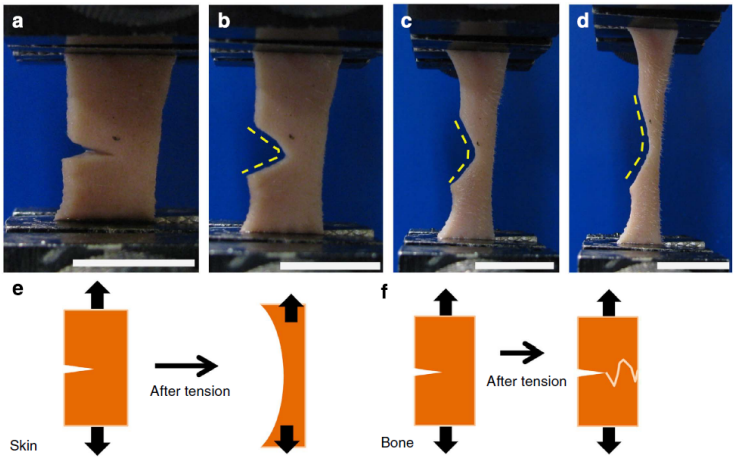

Figure 2.5 Attempted propagation of a tear in skin by Yang *et al* (2015), and comparison with crack propagation in bone [14]

2.2.3 Inter-sample variability

Skin has a high degree of both inter and intra subject variability [1], with nominally identical samples giving widely different results. It is not unusual for the standard deviation of a series of test results to be on the same order of magnitude as the mean [12, 15, 1].

2.3 Material models of skin

A wide variety of macro-scale non-linear constitutive models have been used to model the mechanical properties of skin, including isotropic models such as the Ogden Model (Ogden 1973 [3]), the Mooney-Rivlin model (Rivlin 1948[16]), and the neo-Hookean model (Flynn *et al* 2011 [17]).

One of the first anisotropic strain energy functions to capture both the nonlinearity and the anisotropy of skin was developed by Fung [18] in 1976. This model captured either transverse isotropy (5 parameters) or orthotropy (9 parameters), and could describe the mechanical behaviour of a wide range of collagenous soft tissues. A number of other models such as the fully integrated distributed fibre model (Lanir (1979)[19]), the Gasser-Ogden-Holzapfel model (Gasser *et al* (2006) [20]) and the Weiss model (Weiss *et al* (1998) [21]) have been developed, but only the Fung and Weiss models will be covered.

Macro scale tissue models have the advantage of allowing for efficient FEA implementation, but can be less accurate than micro-mechanical fibre models[1].

2.3.1 Isotropic Tissue models

2.3.1.1 Ogden Model

The Ogden material model is a general hyper-elastic model, expressing the strain energy density in terms of the principle stretches (λ_i), hydrostatic pressure (P) and volume ratio (J):

$$\mathbf{\Psi}_{Ogden} = \sum_{p=1}^{N} \frac{\mu_p}{\alpha_p} \left(\lambda_1^{\alpha_p} + \lambda_2^{\alpha_p} + \lambda_3^{\alpha_p} - 3\right) - P(J-1) \tag{2.1}$$

Where μ_p are shear moduli and α_p are dimensionless material constants representing strain hardening.In the incompressible case the volume ratio (J) will always be unity, and as such the strain energy for an incompressible Ogden material is given by:

$$\mathbf{\Psi}^{inc}_{Ogden} = \sum_{p=1}^{N} \frac{\mu_p}{\alpha_p} \left(\lambda_1^{\alpha_p} + \lambda_2^{\alpha_p} + \lambda_3^{\alpha_p} - 3\right) \tag{2.2}$$

The Ogden material model can capture a wide variety of isotropic hyper-elastic behaviour, particularly when one increases the N parameter. Shergold et al (2006) [22] showed that even for $N = 1$, the Ogden model can capture the majority of the uniaxial tensile behaviour of skin.

2.3.1.2 Mooney-Rivlin model

The Mooney-Rivlin material model gives the strain energy density in terms of the first two invariants of the Cauchy-Greene deformation tensor, and is commonly used for modelling rubber and other elastomers:

$$\mathbf{\Psi}^{inc}_{Mooney-Rivlin} = C_1(I_1 - 3) + C_2(I_2 - 3) = C_1(\lambda_1^2 + \lambda_2^2 + \lambda_3^2 - 3) + C_2(\lambda_1^2\lambda_2^2 + \lambda_2^2\lambda_3^2 + \lambda_3^2\lambda_1^2 - 3) \tag{2.3}$$

Where C_1 and C_2 are material constants.
Due to the incompressibility condition ($J = \lambda_1\lambda_2\lambda_3 = 1$), the above can be re-written as:

$$\mathbf{\Psi}^{inc}_{Mooney-Rivlin} = C_1(\lambda_1^2 + \lambda_2^2 + \lambda_3^2 - 3) + C_2(\lambda_1^{-2} + \lambda_2^{-2} + \lambda_3^{-2} - 3) \tag{2.4}$$

Note that setting ($N = 2, \alpha_1 = 2, \alpha_2 = -2$) in the incompressible Ogden model results in the incompressible Mooney-Rivlin material model.

2.3.1.3 Neo-Hookean model

Setting $(N = 1, \alpha_1 = 2)$ in the Ogden model results in the Neo-Hookean material model:

$$\mathbf{\Psi}^{inc}_{Neo-Hookean} = C_1(\lambda_1^2 + \lambda_2^2 + \lambda_3^2 - 3) = C_1(I_1 - 3) \tag{2.5}$$

Where C_1 is a material constant. This model performs reasonably in tension for relatively small strains, but poorly in compression[22].

2.3.2 Anisotropic tissue models of skin

2.3.2.1 Weiss model of a general anisotropic, hyper-elastic soft tissue

Weiss et al (1996) [4] developed a general anisotropic, hyper-elastic model for soft tissue. This model consisted of a Mooney-Rivlin term for the "matrix" (i.e. elastin in the case of skin), a transversely isotropic term for the collagen fibre reinforcements, and a simple compression law for the bulk deformation:

$$\Psi = C_1(I_1 - 3) + C_2(I_2 - 3) + F(\lambda) + \frac{1}{2}K[ln(J)]^2 \tag{2.6}$$

$$\frac{\partial F}{\partial \lambda} = \begin{bmatrix} 0 & \lambda < 1 \\ \frac{C_3}{\lambda}[e^{C_4(\lambda-1)} - 1] & \lambda < \lambda^* \\ \frac{1}{\lambda}(C_5\lambda + C_6) & \lambda \geq \lambda^* \end{bmatrix}$$

Note that this model considers collagen fibres to have zero compressive stiffness. λ^* represents the stretch ratio at which the collagen fibres are considered to be fully straightened. After this point, the stress:stretch relationship is considered to be linear, whilst the stress:stretch relationship is considered to be exponential prior to this point.

2.3.2.2 Weiss model of a general anisotropic, visco-elastic soft tissue

In 1998 Puso & Weiss [21] extended the work of Weiss et al (1996) [4] to include visco-elastic effects. The strain energy density function took the same form as above, but a quasi-linear Prony series was added to represent the viscous stresses:

$$\boldsymbol{S}(\boldsymbol{C}, t) = \boldsymbol{S}(\boldsymbol{C}) + \int_0^t 2G(t-s)\frac{\partial \Psi}{\partial \boldsymbol{C}(s)}ds \qquad G(t) = \sum_{i=1}^{N} S_i e^{\frac{t}{T_i}} \tag{2.7}$$

Note that S_i is the i^{th} Prony series co-efficient (a scalar), whilst $\boldsymbol{S}$ is the second Piola-Kirchoff stress (a 3x3 tensor). This model is included in LS-Dyna's list of material models as Mat_Soft_Tissue_Visco, and has been used to model various collagenous soft tissues such as tendons, fascia and ligaments [23].

2.3.2.3 Phenomonological model by Fung

In the 1970s Fung developed a new phenomenological for skin which captured non-linear orthotropic behaviour [18] in a plane stress state. This model required 9 material parameters, but could model

transverse isotropy with only 5 material parameters:

$$\begin{aligned}\boldsymbol{\Psi}_{Fung} &= f(\alpha, \boldsymbol{C}) + ce^{F(\alpha,\boldsymbol{C})} \\ f(\alpha, \boldsymbol{C}) &= \alpha_1 \boldsymbol{C}_{11}^2 + \alpha_2 \boldsymbol{C}_{22}^2 + 2\alpha_4 \boldsymbol{C}_{11}\boldsymbol{C}_{22} \\ F(\alpha, \boldsymbol{C}) &= \alpha_1 \boldsymbol{C}_{11}^2 + \alpha_2 \boldsymbol{C}_{22}^2 + \alpha_3 \boldsymbol{C}_{12}^2 + 2\alpha_4 \boldsymbol{C}_{11}\boldsymbol{C}_{22} + \gamma_1 \boldsymbol{C}_{11}^3 + \gamma_2 \boldsymbol{C}_{22}^3 + \gamma_4 \boldsymbol{C}_{11}^2 \boldsymbol{C}_{22} + \gamma_5 \boldsymbol{C}_{11}\boldsymbol{C}_{22}^2\end{aligned} \tag{2.8}$$

Note that $\boldsymbol{C}$ is the right Cauchy-Greene deformation tensor, with index 1 referring to the longitudinal axis of the animal and index 2 referring to the transverse axis. c, α, and γ are material constants with no physical meaning, and are extracted through least squares error fitting of experimentally determined mechanical behaviour of skin. Note that this model is not objective, unlike the isotropic models covered in section 2.3.1.

2.3.3 Micro-mechanical modelling of skin

Tonge (2014) modelled the mechanical response of skin at a micro scale, simulating individual collagen fibres. This approach yielded more accurate results when compared to macro scale continuum modelling of skin, but at the cost of significantly higher computational overheads[1]. This approach can be useful in a research context, but is generally not feasible outside of research, given the high computational costs. Until computational power significantly increases, micro-mechanical models of skin are unlikely to be feasible for most applications.

Constitutive equations to model the exponential stiffening of the collagen fibres have been developed (Bischoff *et al* 2000 [24]), (Tonge 2014 [1]). These equations are used within micro-mechanical models of skin to model the fibres embedded in the bulk tissue.

2.3.3.1 Modelling of fibres as sinusoidal elastica beams

Conminou and Yannas (1979) [25] showed that collagen fibres can be modelled as sinusoidal elastica beams, resulting in non-linear macroscopic behaviour from linear microscopic behaviour. This approach was used by Tonge (2014) [1] to model collagen fibres embedded within the elastin tissue of skin.
The undeformed collagen fibre was assumed to follow the sine wave $\boldsymbol{X}_2 = asin(b\boldsymbol{X}_1)$, have a radius R, and Young's modulus E_y. The rotation angle of the midline ($\Theta = arctan(\frac{\partial \boldsymbol{X}_2}{\partial \boldsymbol{X}_1})$) was approximated as $\Theta(\boldsymbol{X}_1) = abcos(b\boldsymbol{X}_1)$ for small angles.
Assuming that the radius:length ratio, micro-scale strain, and initial crimp are all small, analytical solutions can be derived for the deformed midline rotation angle ($\theta(\boldsymbol{X}_1)$), micro-scale stretch ratio ($\lambda(\boldsymbol{X}_1)$) and macro-scale stretch ratio ($\bar{\lambda}$) for a given force (F) applied in the e_1 direction to the tip of the beam.
Introducing the non-dimensional parameters $\alpha = \frac{F}{E_y R^2 \pi}$ and $\beta = b^2 R^2$ and setting the initial crimp angle $\Theta_0 = ab$, Comninou and Yannas showed that $\theta(\boldsymbol{X}_1)$, $\bar{\lambda}$, and $\lambda(\boldsymbol{X}_1)$ could be written as[25]:

$$\theta(\boldsymbol{X}_1) = \frac{\beta}{4\alpha(1+\alpha)+\beta}\Theta((X)_1) \tag{2.9}$$

$$\lambda(\boldsymbol{X}_1) = 1 + \alpha cos(\theta(\boldsymbol{X}_1)) \tag{2.10}$$

$$\bar{\lambda} = \int_0^L \frac{\lambda}{L}\frac{cos(\theta(\boldsymbol{X}_1))}{cos(\Theta(\boldsymbol{X}_1))}d\boldsymbol{X}_1 \tag{2.11}$$

In terms of the initial crimp angle Θ_0, α, and β, the macro scale stretch can be found by substituting eq. (2.9) and eq. (2.10) into eq. (2.11):

$$\bar{\lambda} = \frac{1}{L}\int_0^L \left[1 + \alpha cos\left(\frac{\beta}{4\alpha(1+\alpha)+\beta}\Theta_0 cos(b\boldsymbol{X}_1)\right)\right] \frac{cos\left(\frac{\beta}{4\alpha(1+\alpha)+\beta}\Theta_0 cos(b\boldsymbol{X}_1)\right)}{cos\left(\Theta_0 cos(b\boldsymbol{X}_1)\right)} d\boldsymbol{X}_1 \tag{2.12}$$

Figure 2.6 shows the dimensionless force vs macro stretch curves for a series of sinusoidal elastica beams with varying initial crimp angles. Note that each curve approximates the stress strain curve shown in fig. 2.2, with the initial crimp angle controlling the macro stretch at which the curve transitions from the toe region to the heel region, and from the heel region to the linear region.

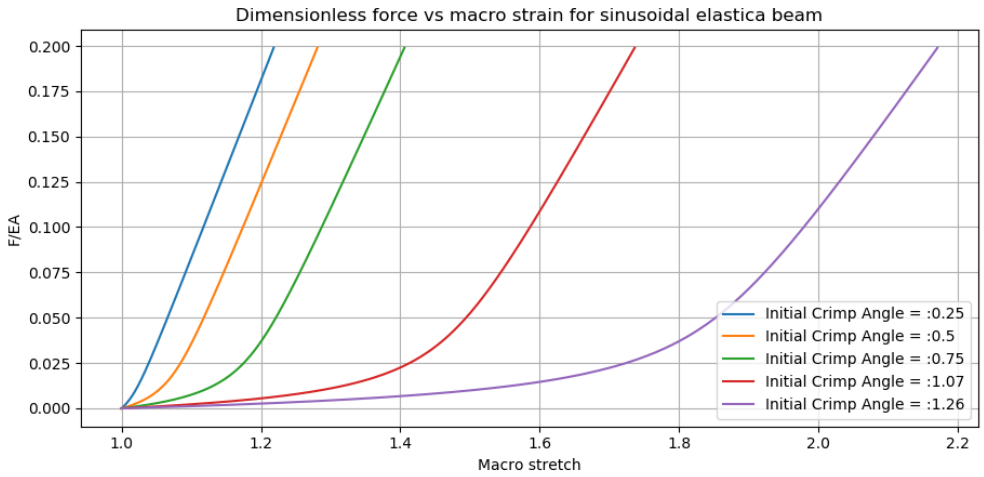

Figure 2.6 Dimensionless force:stretch curves for sinusoidal elastica beams with initial crimp angle ranging from 0.25 to 1.26

2.4 Test methodology

The properties of skin have been tested for using a wide variety of methods, including both *in vivo* and *ex vivo* methods. By necessity, *in vivo* tests have to occur over a relatively low range of strains, and cannot test to destruction. *In vivo* test methods include pipette aspiration, nanointentation, and bulge testing via suction. Due to the constraints on *in vivo* testing, and the aim of this dissertation, *ex vivo* test methods will be focussed on.

Ex vivo test methods in the literature have commonly consisted of uniaxial tension tests, uniaxial compression tests, planar tension tests and bulge tests. Given that the focus of this dissertation is the development of a high strain rate bulge test, bulge testing methodology are covered in their own section.

2.4.1 Uniaxial tension

Uniaxial tensile testing is advantageous in that it is a common engineering material test, and is easy to conduct, analyse and measure. Disadvantages of uniaxial tensile testing of skin are twofold:

1. Measuring anisotropic properties through uniaxial tensile tests requires multiple tests at varying angles with respect to Langer's lines in order to fully capture anisotropic behaviour. This in

turn requires relatively large amounts of sample material - a problem when skin samples can be hard to come by. Given the high level of inter- and intra-subject variability exhibited by skin, it can be difficult to detect whether the change in properties between uniaxial tensile specimens is due to orientation relative to Langer's lines or due to specimen variability. Figure 2.7 shows uniaxial tensile test dogbone samples used by [12], oriented at 0, 45 and 90 degrees to Langer's lines. Note the small number of available samples obtained from a cadaver.

Groves *et al* , 2012 [26] made use of circular test specimens for low strain rate non-destructive uni-axial tensile tests of murine skin, allowing for re-use of specimens. This, combined with the circular shape of the specimen, allowed for sequential tests in multiple directions on the same specimen. The advantages of this are twofold:

(a) The same specimen can be used multiple times, allowing for significantly more data to be extracted from a given amount of skin, compared to the approach shown in fig. 2.7.

(b) The mechanical properties of skin are highly variable between subjects, and even within subjects. Testing the same sample at different orientations guarantees that one's results (change in properties with orientation relative to Langer's lines) are not contaminated by the change in properties with location on the body. Whilst the lower 3 samples shown in fig. 2.7 are all nominally "lower back samples"[12], their properties are likely to vary somewhat, leading to increased scatter in the data.

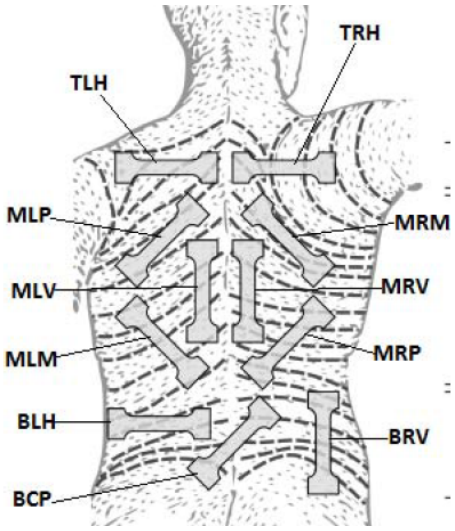

Figure 2.7 Uniaxial tensile test samples by Gilchrist *et al* (2012) , oriented at 0, 45 and 90 degrees to Langer's lines [12]

A disadvantage of the approach used by Goves *et al* is that the skin samples can only ever be tested to low strains, and it is possible that the properties of the skin samples tested will change with successive tests. Additionally, this approach is results in more complex boundary conditions than standard uniaxial tensile tests - making analysis significantly more difficult and requiring FEA for modelling of boundary conditions.

2. Uniaxial tensile tests of skin suffer from preconditioning effects, and are thought to poorly simulate *in vivo* conditions[1]. Skin is seldom loaded in uniaxial tension *in vivo*, but rather in biaxial tension. Yang *et al* (2015) [14] showed the remarkable tear resistance of skin due to the re-alignment of collagen fibres under uniaxial tensile loading. Transverse stresses in skin have a large impact on its behaviour, and simply testing in uniaxial tension in multiple directions is not sufficient to capture the properties of skin.

2.4.1.1 High strain rate uniaxial testing of skin

Whilst there has been a fair amount of quasi-static tensile testing of skin, there has been a paucity of high strain rate tensile testing of skin[12]. Part of the reason for this is the relative difficulty of high strain rate tests when compared to quasi-static tests. Additionally, high strain rate tests tend to destroy the specimen, whilst low strain rate tests in the elastic regime allow for reuse of specimens - a significant advantage, given the difficulty in obtaining test material.

Gallagher *et al* (2012) [12] tested skin from 3 human cadavers at dynamic strain rates, finding that the mechanical properties of human skin are highly dependant on the orientation with respect to Langer's lines, as well as the strain rate. Large variations in results were found, with the UTS ranging from 17.9 to 36.5 MPa, and the apparent modulus ranging from 56.8 to 141.11 MPa, in spite of test material coming from nominally similar sources.

Jacquemoud *et al* (2007) [15] tested uniaxial skin samples at mean strain rates of $55s^{-1}$, finding that the measured UTS was similar to that of quasi-static tests, but the elongation at break was approximately half of the quasi-static elongation at break. When testing at high strain rates, Jacquemoud *et al* (2007) found the local strain to be as much as double the macro (averaged over the gauge section) strain in places. This was as a result of the high strain rates and forces, as well as possible heterogeneity of the samples. This shows the difficulty in accurately testing biological tissues at high strain rates, and can be a significant source of error if not properly measured and accounted for.
It should be noted that the specimens tested did not appear to be loaded in pure tension. Figure 2.9 shows the displacement and strain field obtained - note that the displacement does not appear to be purely uniaxial.

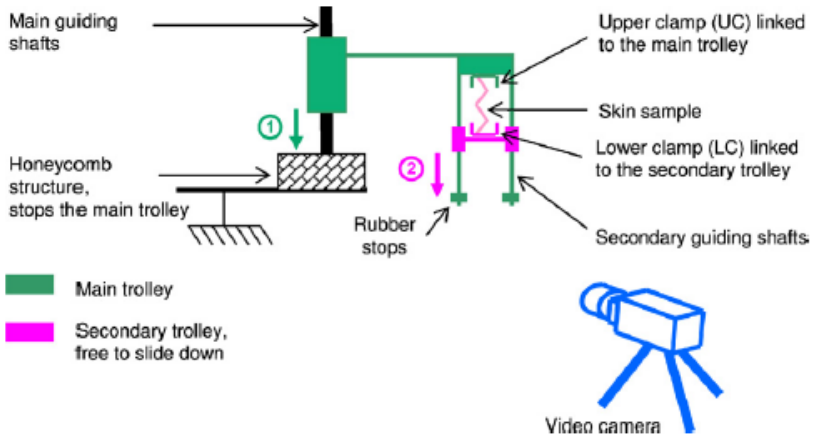

Figure 2.8 High strain rate tensile test apparatus used by Jacquemoud *et al* [15]

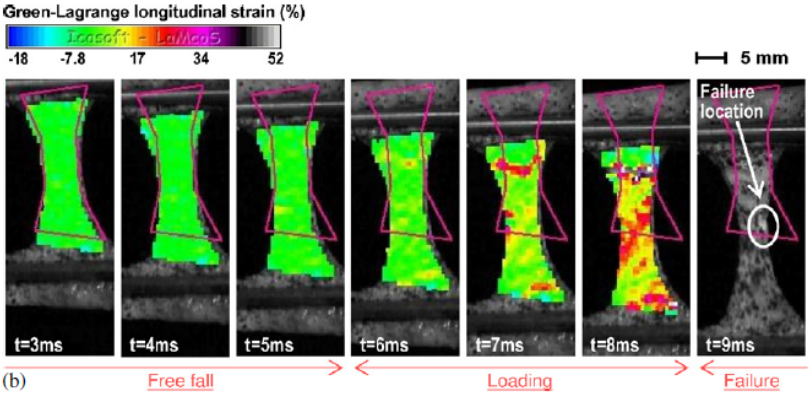

Figure 2.9 Green-Lagrange longitudinal strain field for high strain rate tests obtained by Jacquemoud et al [15]

2.4.2 Planar tension

Lanir and Fung (1974) [2] conducted quasi-static biaxial tension tests of rabbit skin using a biaxial crucifix specimen, as well as intermediate strain rate constrained uniaxial tensile tests.
The quasi-static biaxial tension tests were conducted by moving both the x and the y axis clamps outwards, stretching the skin biaxially. This method suffered from complex boundary conditions, but allowed for a more easily controllable strain rate (as it was displacement driven rather than force driven).
When testing at intermediate strain rates, one of the trolleys was fixed (allowing zero strain in the y direction) whilst the x trolley was moved outwards. This test differed from a standard uniaxial tension test in that the specimen was constrained in the transverse direction - leading to a plane stress state rather than a uniaxial stress state.
Like uniaxial tension tests, the skin samples exhibited preconditioning effects. The samples had to be preconditioned in biaxial tension, and uniaxial preconditioning appeared to have little effect on samples tested in biaxial tension.

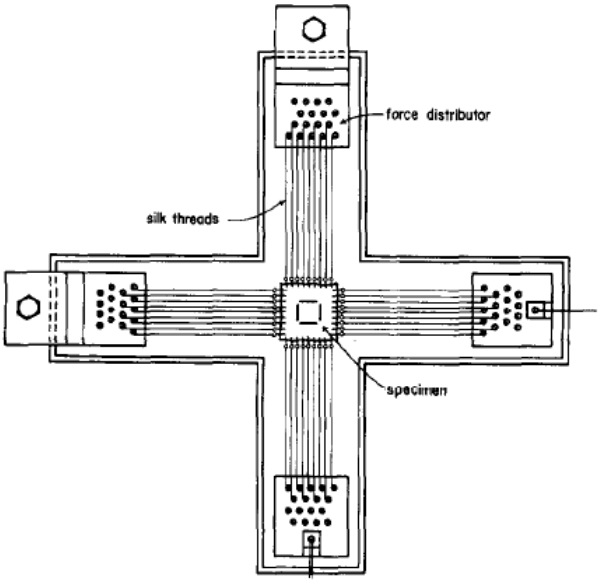

Figure 2.10 Biaxial tension test device used by Lanir and Fung (1974) [27]

This method has been used for biaxial tension testing of a variety of biological soft tissues including Aortic valve tissue [28] and the skin of bat wings [29] Biaxial tension testing of crucifix shaped specimens has the same limitations as uniaxial tension testing with regards to the effects of preconditioning[1, 2], as well as achievable strain rate.

2.4.3 Uniaxial compression

For an incompressible material, uniaxial compression results in a strain field which is nominally equivalent to biaxial tension, but produces a different stress state. Shergold *et al* (2006) [22] conducted a series of high strain rate uniaxial compression tests on skin using a Split Hopkinson Pressure Bar apparatus.

The Split Hopkinson Pressure Bar The Split Hopkinson Pressure Bar (SHPB) is an apparatus commonly used for high strain rate uniaxial compression tests. In this apparatus a strain wave is imparted to the input bar via a striker, and measured with a strain gauge. This strain wave is then partially reflected by the specimen, with the remainder transmitted to the output bar, where it is captured by a strain gauge. Summing the incident, reflected, and transmitted waves allows one to calculate the forces and velocities of the input and output bar [22]. From this information one can infer the stress and strain state of the specimen (depending on various assumptions made about the test)

This test apparatus is common for high stiffness specimens (such as various metals), but struggles to measure the properties of the specimen if the stiffness ratio between the specimen and the input/output bars is too low.

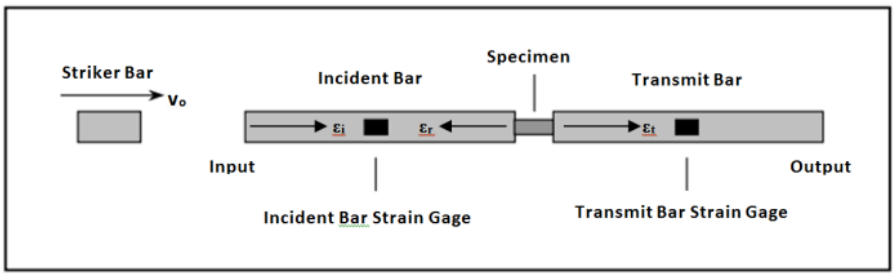

Figure 2.11 Split Hopkinson Pressure Bar apparatus

Compression tests by Shergold *et al* Shergold *et al* (2006) [22] conducted a series on high strain rate uniaxial compression tests on skin and silicone using a Split Hopkinson Pressure bar. This method is promising, however friction between the input/output bars and the specimen will result in lateral constraining of the specimen. This effect will be particularly strong for specimens undergoing high strains (such as biological soft tissue). This effect will invalidate the assumption of uniform uniaxial compression.

Extrapolating these results to obtain biaxial tensile results for skin relies on the assumption that skin is incompressible - any compressibility will result in the skin undergoing non-zero distortional strain, invalidating the assumption that uniaxial compression is equivalent to biaxial tension.

2.5 Bulge testing

Bulge testing of circular (or elliptical) membrane specimens allows for bi-axial tension at the apex of the bulge, whilst avoiding the edge effects associated with the crucifix shaped biaxial tension test. Bulge testing has been used for a wide variety of biaxial tension testing, including:

1. Testing biaxial material properties of metals [30]

2. Quality testing of paper [31]

3. Low strain rate testing of skin [1]

2.5.1 Quasistatic bulge testing of skin

Tonge (2014) bulge tested skin at low (quasi-static) strain rates and low strains, making use of saline solution as the driving fluid[1]. Figure 2.12 shows the quasi-static bulge test apparatus used by Tonge *et al*. Stereoscopic Digital Image Correlation (DIC) was used to measure the deformation of the membrane. This approach was promising in that it gave repeatable, accurate measurements without the effects of preconditioning (more accurately simulating *in vivo* conditions), but had the downside of increased complexity (when compared to more common methods of tensile testing).

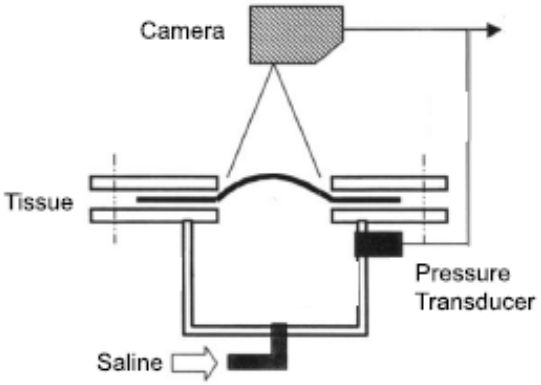

Figure 2.12 Quasi-static bulge test apparatus used by Tonge *et al* (2014) [1]

The force and cross-sectional area of a uniaxial tensile test can be measured relatively easily, as can the longitudinal strain. In contrast, the stress in a bulging membrane is a function of the pressure, curvature and membrane thickness. Calculating the stress in a bulging membrane requires measurement of the deformation field, calculating the curvature and thickness field from that, and then calculating the stress.

Particularly with thicker membranes, the bending stress can be a source of error if not accounted for, requiring more complex FEA models. Including the effects of bending significantly increases the difficulty of calculating stress and material parameters [1]. Quasistatic bulge tests are well understood, and have been widely used for various materials.

2.5.2 Dynamic bulge testing

2.5.2.1 Modified Split Hopkinson Pressure Bar apparatus

Dynamic bulge testing of membranes, much like dynamic uni-axial tests, is significantly more complex than quasi-static testing. Grolleau *et al* (2007) [32] developed a high strain rate bulge test for sheet metals using a modified SHPB with polymeric input bars and a water filled pressure cell which loaded the sheet metal specimen. This design was improved on in 2010 by Ramezani and Ripin [33], who used rubber as the driving fluid instead of water.

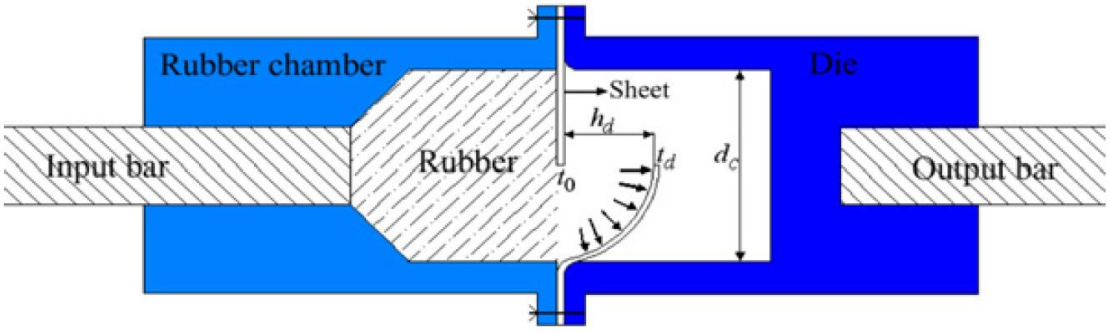

Figure 2.13 Modified SHPB bulge test developed by Ramezani and Ripin (2010) [33]

Figure 2.13 shows the modified SHPB bulge tester developed by Ramezani and Ripin (2010) [33]. Rather than directly contacting the specimen, the input bar transitions to a rubber pad, converting the (predominantly) uni-axial stress of the input bar to (predominantly) hydrostatic stress used to bulge the specimen. Much like a typical SHPB, force/pressure measurement is conducted by measuring strain in the input and output bars. Strain rates obtained at the peak of the dome were 160 and 215 s^{-1}, with input bar velocities of 11 and 14 m/s.

This work provides a promising method of high strain rate bulge testing of sheet metals, however is not suitable for biological materials for the following reasons:

1. Force measurement: Should the membrane under testing be of biological origin (such as skin), the forces involved will be much lower than the forces involved in the testing of sheet metals. As such, the strain waves in the input and output bars will be a lot lower - making force measurement more challenging. This would likely require the use of input and output bars with a low elastic modulus, however most materials with a low elastic modulus (such as polymers) are visco-elastic. This causes the strain waves to damp down, and makes measurement more difficult. Note that the force measurement of the output bar will include the inertial forces associated with the clamp mechanism. Given then relatively large mass of the clamp, these forces will likely obscure the forces associated with low bulge pressures.

2. Strain measurement: The strains are inferred from the final shape of the specimen in this test. This is suitable for materials such as mild steel with a large plastic strain regime relative to the elastic strain regime, but is not suitable for hyper-elastic materials. As such, this method is not suitable for soft biological membranes, and as such some form of optical measurement would be needed should this method be used for the testing of biological tissue. The Design of Apparatus section deals with this in more detail.

2.5.2.2 Shock tube as a high strain rate bulge test

More recently, Bentil et al (2016) [34] developed a dynamic inflation test for soft materials, making use of a shock tube apparatus to supply the pressure pulse. Polydimethysiloxane (silicone) was used as a soft tissue/skin simulant, and speckled with black, matte spray paint. Two high speed digital cameras and DIC software were used to record the deformation field of the silicone membrane [1]. This deformation field was compared to the recorded pressure history, and used to calculate the dynamic storage modulus and loss modulus of the silicone material.

[1] Note that the deformation measurement method used by Bentil *et al* is the same as the deformation measurement method used by Tonge *et al* (2014) [1].

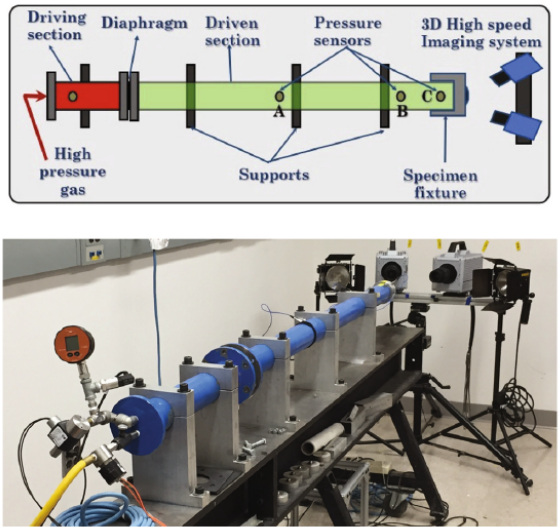

Figure 2.14 Experimental setup used by Bentil et al (2016) [34]

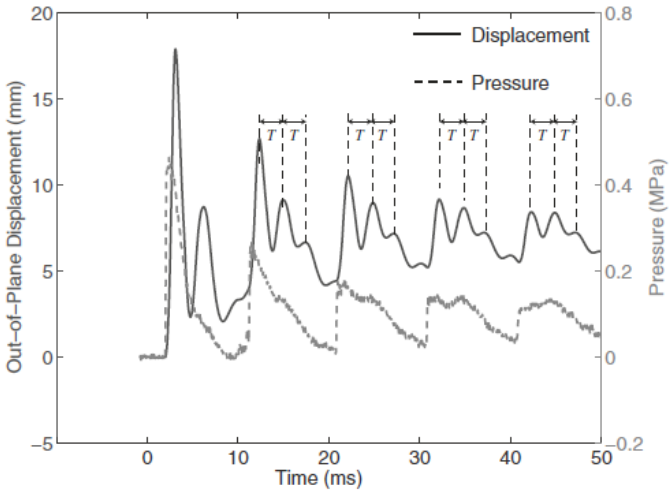

Figure 2.15 Pressure and out of plane displacement history for apex of shock driven membrane vs time [34]

This method was successful in determining the dynamic storage and loss moduli of the material with a high degree of accuracy, but was limited in that only limited control of the pressure profile was possible. Further comments on the suitability of this method to high strain rate bulge testing of skin are made in the Design of Apparatus section.

2.5.3 Modelling of membrane stress state

2.5.3.1 Sphere section deformation

For thin membranes made from isotropic materials and undergoing small strains, assuming that the membrane deforms as a sphere section can yield reasonable approximations without the use of FEA or more complex calculations. This assumption has been used extensively in modelling bulge tests, particularly of sheet metal [33, 35]. Strikwerda and Considine (1994) [31] showed that this assumption closely approximates the deformation of a membrane at low strains. If one makes these assumptions, and uses thin walled cylinder theory, the principal stretch ratios can be calculated in terms of bulge height, and the principal Cauchy stresses in terms of bulge height and driving pressure.

$$P = \frac{\sigma t}{R} \tag{2.13}$$

$$R = \frac{h^2 + r^2}{2h} \tag{2.14}$$

$$\theta = sin^{-1}\left(\frac{r}{R}\right) = sin^{-1}\left(\frac{2rh}{h^2 + r^2}\right) \tag{2.15}$$

The hoop stretch ratio at the apex can be approximated as:

$$\lambda_x = \lambda_y = \frac{R\theta}{r} = \frac{(h^2 + r^2)}{2hr} sin^{-1}\left(\frac{2rh}{h^2 + r^2}\right) \tag{2.16}$$

The thickness at the apex will be given by:

$$t = t_0 * \lambda_z \tag{2.17}$$

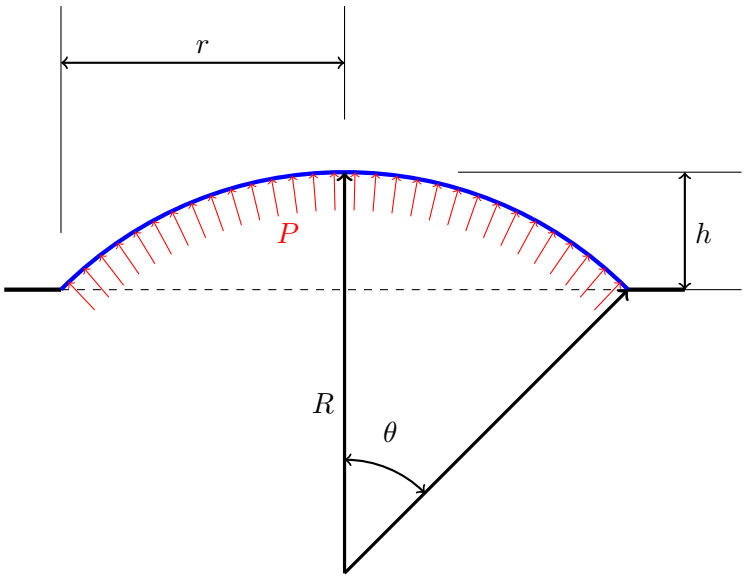

Symbols used:

r: radius of unstretched membrane

h: height of bulge at apex

R: radius of curvature of membrane

θ: half of arc angle of membrane

P: internal pressure

Figure 2.16 Cross section of a deformed, pressure driven membrane under the sphere section assumption

Using the above equations allows one to quickly generate rough figures for approximate design pressures required during the preliminary experimental design stage. Note that skin is not isotropic, the strains are not small, and the membrane will not necessarily be under equilibrium - particularly for a high strain rate test.

2.5.3.2 Deformation field for elliptical membrane boundary

If the membrane boundary is an ellipse (rather than a circle), eqs. (2.14) and (2.16) can be modified to take this into account, where r is no longer constant, but instead dependant on orientation (effectively fitting an ellipsoid to the bulge rather than a sphere). This modification gives an approximate indication of the strain state at the apex of the membrane, but is not expected to be accurate. It does not balance force and stress, and ignores the effects of Poisson's ratio. Jayyosi *et al* (2017) [36] showed that this approximation leads to errors of approximately 10-15% in the estimation of apex strain. The approximate major:minor axis strain ratio at the apex is inversely proportional to the square of the major:minor diameter ratio, and is shown in fig. 2.17.

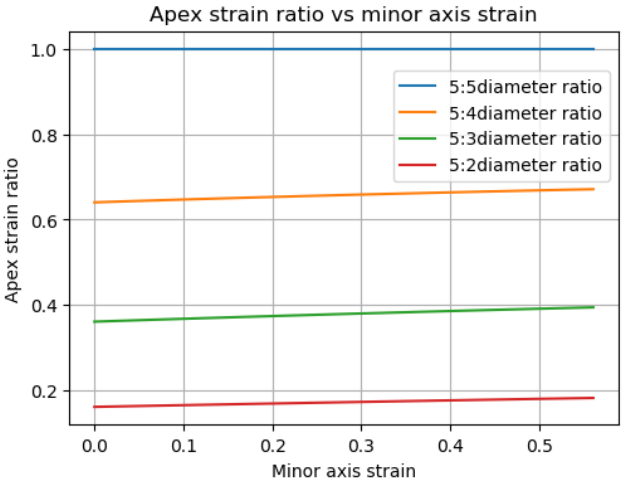

Figure 2.17 Principal strain ratio at apex of ellipse vs minor axis strain for various major:minor diameter ratios. Figure generated by author making use of equations described in section 2.5.3.1

2.5.3.3 Incompressible hyper-elastic sphere section deformation

Figure 2.18 shows the simulated principal Cauchy stress ($\boldsymbol{T}_{11}$) at the apex of the membrane vs driving pressure and principal stretch for a 2mm thick, 50mm diameter membrane bulging from flat to hemispherical. The stress state was modelled for B452 silicone, Sil8800 silicone, human skin, and pig skin. Mooney-Rivlin, Ogden, and Linear Elastic material models were used. Material constants were extracted from the work done by Shergold et al (2006) [22].

Material	**Material model**				
	Mooney-Rivlin		**Ogden**		**Linear Elastic**
	$C1$ (MPa)	$C2$ (MPa)	α	μ(MPa)	E_y(MPa)
B452 Silicone	0.5	0	3	0.4	0.6
Sil8800 Silicone	1.0	0.9	2.5	2.1	2.6
Human skin	0.3	0	9	0.11	0.495
Pig Skin	-	-	12	0.4	2.4

Table 2.1 *Material constants for silicone, human skin, and pig skin taken from Shergold* et al *(2006) [22]*

Note that each line represents a membrane bulged from flat to hemispherical. Linear-elastic models are clearly inaccurate at stretches beyond the infinitesimal. For low pressures, the Mooney-Rivlin and Ogden models give fairly similar pressure:stress results, but the Mooney-Rivlin model quickly struggles to capture the high degree of strain hardening that skin undergoes.

2.5.4 FEA modelling of a bulge test

The analytical solutions presented in previous sections all assumed zero acceleration. In higher strain rate tests, the forces due to acceleration become non-negligible, and can no longer be ignored. This is particularly true for materials with low specific stiffness such as soft biological tissue and elastomeric material.

Taking the force due to acceleration into account makes high strain rate membrane tests difficult to model analytically, particularly when the material is anisotropic and heterogenous. High strain rate membrane tests of steel have been successfully modelled using FEA by numerous researchers [33, 37]. Einstein *et al* (2003) [38] developed a dynamic FEA implementation of nonlinear, anisotropic, hyperelastic biological membranes, and Tonge successfully modelled low strain rate bulge tests of skin in 2014 [1] using FEA. Finite element modelling of high strain rate bulge testing of skin is thus anticipated to be entirely feasible, given appropriate material models.

2.5.5 Extraction of material parameters using Inverse iteration process

Given the difficulty involved in analytically modelling a bulge test, explicitly extracting material parameters from experimental data can be challenging. As a result, an inverse iteration material

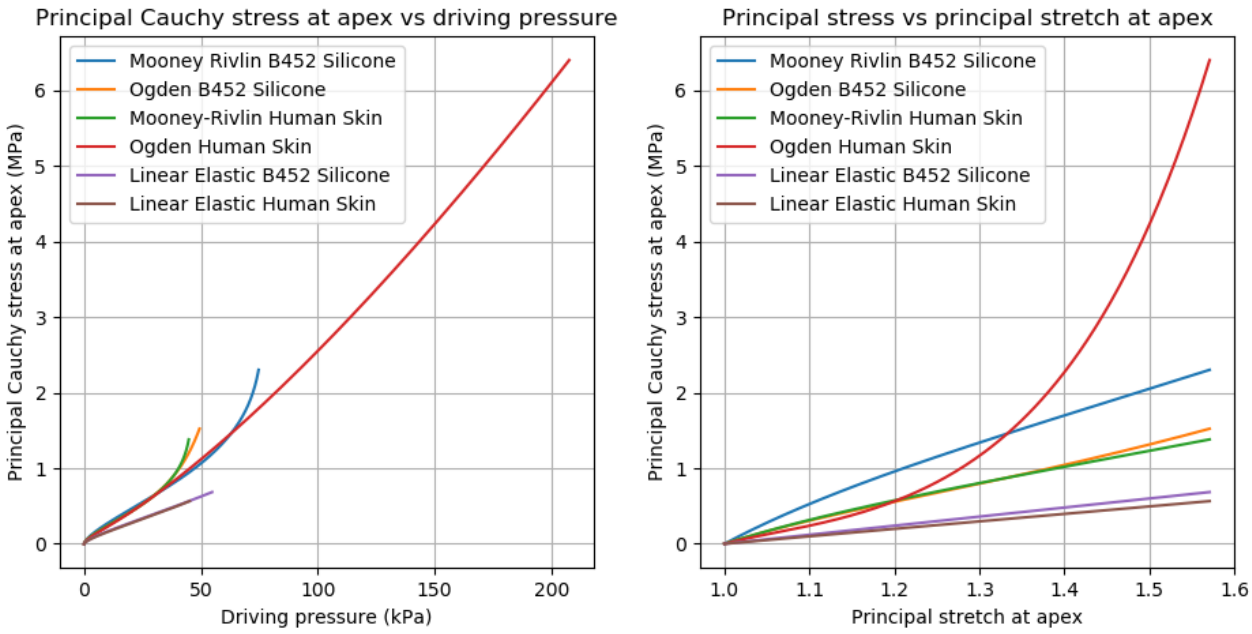

Figure 2.18 Principal Stress at apex of bulge vs driving pressure and principal stretch at apex for silicone and human skin. Plot generated by author using Python and extensions to equations shown in this section.

parameter extraction process is needed. The inverse iteration process works by modelling the test using FEA and an initial guess for the material parameters. The results predicted by the FEA are compared to actual experimental results, and a least squares optimisation is used to reduce the difference between the experimental and numerical results by changing material parameters [39].
DIC can be used to measure the full field deformation of a surface, and FEA to model the predicted deformation based on initial material parameters. The material parameters can then be optimised to reduce the difference between the predicted and experimental deformation field. This approach was successfully used by Tonge et al (2014) [1] to extract material parameters for skin undergoing quasi-static bulging, Curry (2017) [37] to extract material parameters for steel plates undergoing air-blast loading, and Seng *et al* (2015) [40] to extract material parameters for elastomeric materials under a variety of loading conditions.

2.6 DIC tracking of deformation

2.6.1 Background

Digital Image Correlation (DIC) is a non-contact [2] measurement method of generating a displacement field by tracking a pattern on a surface of interest. Whilst photogrammetry methods have existed since 1850 [41], one of the first practical proposals for computer based Digital Image Correlation was published in 1982 by Peters and Ranson [42], and shown to be feasible by Sutton et al in 1983 [43]. As sensor and computer technology improved, the accuracy and ease of 2D DIC measurements increased,

[2]Many DIC methods rely on tracking a speckle pattern which has been painted onto the object. In these cases it would be more accurate to describe DIC as a "minimal contact" measurement method, as the paint of the speckle pattern does contact the object/surface of interest.

to the extent that highly accurate hand held 2D DIC equipment is now available commercially [44]. DIC is currently used for a wide range of non-contact measurement applications on scales ranging from hundreds of metres to nanometres [41].

3D DIC requires more complex setup than 2D DIC, as at least two cameras are required, but results in more accurate measurements (as well as a full 3D displacement field). 2D DIC relies on all motion being in plane, and even small out of plane motion can result in significant inaccuracy [45]. 3D DIC compensates for these out of plane displacements however, resulting in accurate measurements of the nominally 2D deformation field [41].

The primary advantage of 3D DIC over other non-contact measurement methods is that DIC allows one to capture the full field deformation of the membrane, rather than more crude measurements such as the displacement of a series of points [41]. Given the frame rate, initial position and deformed position in each image, the full field deformation can be calculated in the form $\boldsymbol{x} = f(t, \boldsymbol{X})$. From this the deformation gradient $\boldsymbol{F} = \nabla \cdot \boldsymbol{x}$ can be calculated, as well as related strain measures such as the Greene-Lagrange and Cauchy-Greene strain tensors. In addition to the displacement and strain field, the velocity and acceleration fields can be calculated, allowing for measurement of dynamic effects such as vibrations.

If load data (such as pressure, force etc) is recorded, material properties can be inferred from the deformation field and the applied forces. This is covered further in section 2.5.5.

2.6.2 Principles of (3D) DIC

Figure 2.19 shows the basic arrangement and process of 3D DIC. The target specimen is marked with a random greyscale pattern [3], and two synchronised digital cameras are focussed on the area of interest. The cameras are calibrated, and the images are captured. Making use of the calibration data, DIC software calculates full field displacement from the captured images.

2.6.2.1 Calibration:

A calibration target is placed at the focal point of the cameras, and a minimum of 6 distinct images are captured. The dimensions of the calibration targets are known to a high degree of accuracy (on the order of microns), and are used to calculate the camera's parameters. Each camera has 6 parameters that need to be calculated (hence a minimum of 6 distinct images), 3 intrinsic and 3 extrinsic.

Parameter	Meaning
Focal length	The distance from the camera to the point at which the camera is focussed. Intrinsic to the cameras
Principal point	The centre of the image - the point of the focal plane which is nominally normal to the aperture. Intrinsic to the camera
Distortion parameter	Describes the radial distortion caused by the lens. A fish-eye lens would have a large negative distortion parameter for instance, whilst telephoto lenses tend to have large positive distortion parameters. Intrinsic to the camera
Orientation	Orientation of the camera relative to calibration target
Translation vector	Relative translation vector of camera
Rotation matrix	Relative rotation matrix of camera

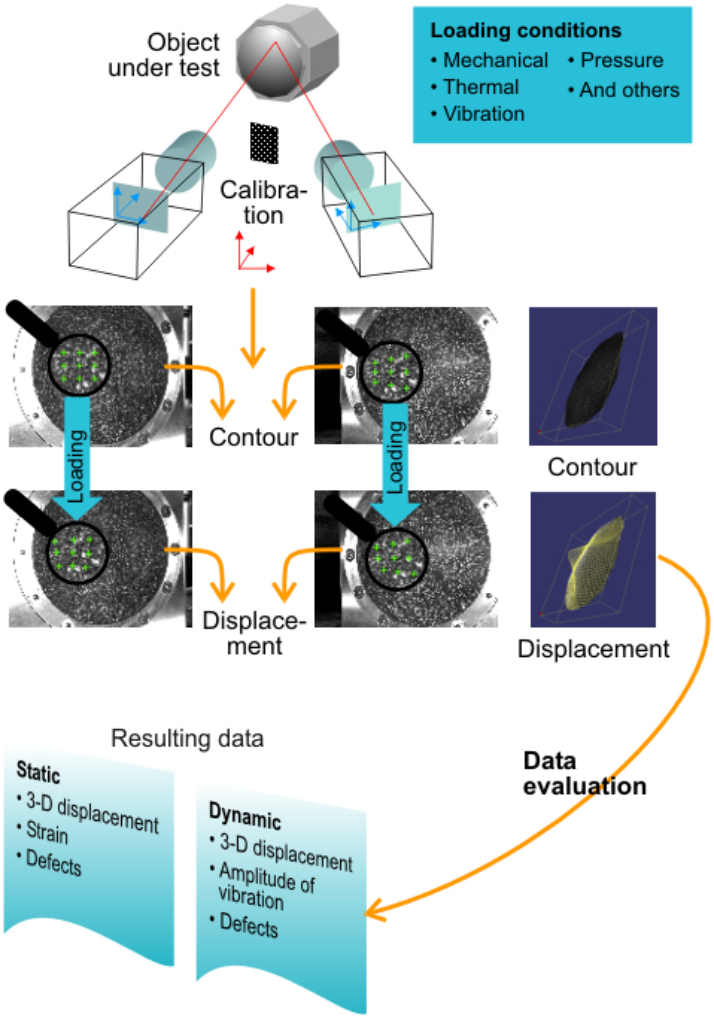

Figure 2.19 Digital Image Correlation Method by Dantec Dynamics [46]

[3] Some DIC methods make use of colour images, but in practise most commercial DIC software makes use of greyscale tracking

2.6.2.2 Displacement calculation:

Each image is divided up into a series of subsets (generally a square of m by m pixels, where m is an odd integer greater than 2), where each subset (henceforth referred to as a facet) needs to have a unique black and white speckle pattern (relative to neighbouring facets). A given facet in the reference configuration will have a reference grey value pattern $G(\boldsymbol{X})$, whilst that same facet in the current configuration will have a grey value pattern of $G(\boldsymbol{x}_t)$. In order to track the position of each facet, the algorithm attempts to keep the grey value pattern of each facet as close to constant as possible. This is done by minimising the square of the differences $\sum (G(\boldsymbol{x}_t) - G(\boldsymbol{X}))^2$ at each time-step. Schreier et al (2000) [47] showed that this method can result in matching accuracy of better than 0.01 pixels. Note that this method is particularly sensitive to changes in light level, and reflections can often lead to a localised loss of correlation.
This displacement calculation technique generates a continuous displacement field, rather than a series of discrete displaced points [41]. This is important, as it allows for more accurate calculation of spatial gradients (strains) than would be the case for a series of discrete points.

2.6.2.3 Speckle Pattern

Shape of pattern: In order to allow for high resolution deformation measurement, the speckle pattern needs to have a high information density. For this reason regular grid patterns make for poor DIC patterns, as they have sparse information per unit area. In comparison, random speckle patterns allow for a high information density per unit area [48]. Should the features be too small (for example half the size of a pixel), they will simply blur together and decrease the information density of the surface. Conversely, if the features are too large, there will be wasted pixels that do not contain useful information. As a general rule of thumb, features on a speckle pattern should be at least 2 pixels wide.

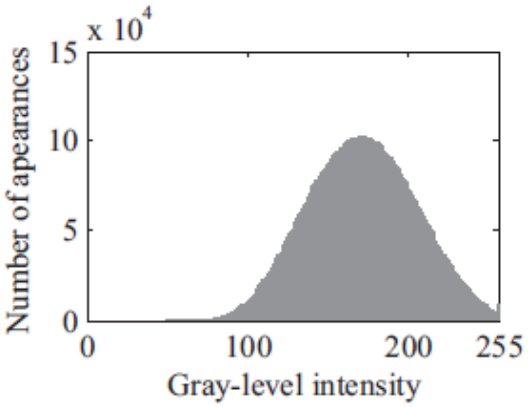

Figure 2.20 Example of a good grey level intensity profile by Park *et al* [48]

Park *et al* (2017) evaluated the effect of various speckle patterns (shown in fig. 2.21) on the results of DIC. Pattern (a) performs poorly due to an insufficient speckle volume, while pattern (c) performs poorly due to a speckle density that is too high. Pattern (b) has the correct speckle density. Figure 2.20 shows the grey level intensity profile for figure (b). Note that very few of the pixels are located at the extremes of the grey scale range.

Speckle Pattern material: Given that the DIC measurements measure the displacement of the speckle pattern itself, the speckle pattern material needs to closely adhere to the sample material. Additionally, the speckle pattern material needs to have negligible stiffness relative to the sample material in order to avoid affecting the deformation profile of the sample.

When measuring the deformation of metal plates, spray paint is a popular method of adding a speckle pattern. This method is fast, cheap and generates good speckle patterns, but can measure limited strains before the paint begins to flake, resulting in a loss of test data[49].

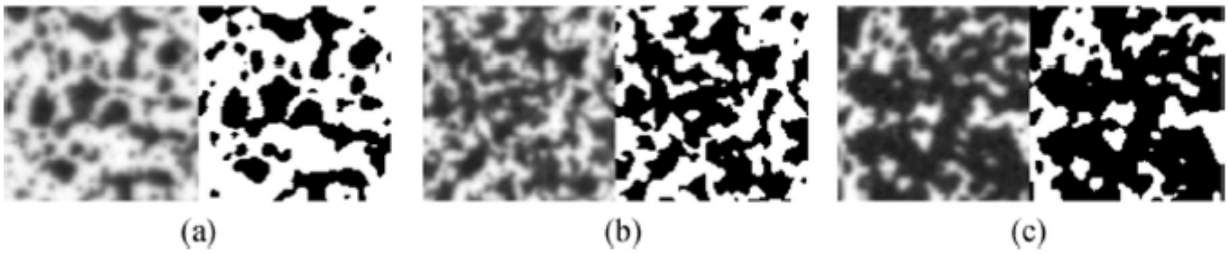

Figure 2.21 Proposed speckle patterns by Park etc al [48] for a 100x100 pixel region. The grey level intensity profile for pattern b is shown in fig. 2.20

Tonge et al (2014) [1] successfully generated a speckle pattern on skin by sprinkling graphite powder on the surface of the skin. This method was well suited to creating speckle patterns on elastomer materials or soft biological tissue as the effective stiffness of the graphite power was negligible, and there was no flaking of the powder. This method relied on the membrane being largely horizontal however, and is not suitable for high strain rate tests (the graphite powder relied predominantly on weight to remain "bonded" to the skin).
Novel speckle pattern techniques developed for use with elastomers at high strain rates are covered in chapter 4.

2.6.3 Lens selection and depth of field

If the specimen is expected to undergo motion normal to the focal plane of the camera(s) used to capture images, the depth of field of the camera becomes an important consideration. Should the object move out of the depth of field of the camera, focus will be lost and the accuracy of the images will drop. Consider a camera with lens focal length $\bar{f}$, relative aperture f, and ideal focal length s as shown in fig. 2.22. Let c be the diameter of the circle of confusion (size of a circle which is indistinguishable from a point by the camera sensor), and D_p be the diameter of the entrance pupil of the system. Let D_N be the distance from the camera to the near limit of focus, and D_F be the distance from the camera to the far limit of focus. The following formulae are adapted from the work of Sutton *et al* (2009) [4] [41],
Defining the hyperfocal distance H as being approximately $\frac{\bar{f}D_p}{c}$, the near and far focal limits are:

$$D_N \approx \frac{Hs}{H+s} \qquad D_F \approx \frac{Hs}{H-s} \qquad \text{for } s < H \tag{2.18}$$

Subtracting D_N from D_F gives the depth of field, resulting in:

$$D_F - D_N = \frac{Hs}{H-s} - \frac{Hs}{H+s} = \frac{2\bar{f}D_p s^2 c}{\bar{f}^2 D_p^2 - s^2 c^2} = \frac{2Nc\bar{f}^2 s^2}{\bar{f}^4 - N^2 c^2 s^2} \tag{2.19}$$

Where $N = \frac{\bar{f}}{D_p}$ is the relative aperture number.

This shows that for a given camera (i.e. fixed c), the depth of field is controlled by the focal length of the lens,the relative aperture number of the lens, and the distance from the camera to the subject. The focal length of the lens ($\bar{f}$) is intrinsic to a given lens, but the distance from the camera to the subject (s) and the f number can be changed relatively easily to increase the depth of field.

[4] These formulae are taken from the work of Sutton *et al*, but are based on optical phenomena that have been understood since medieval times.

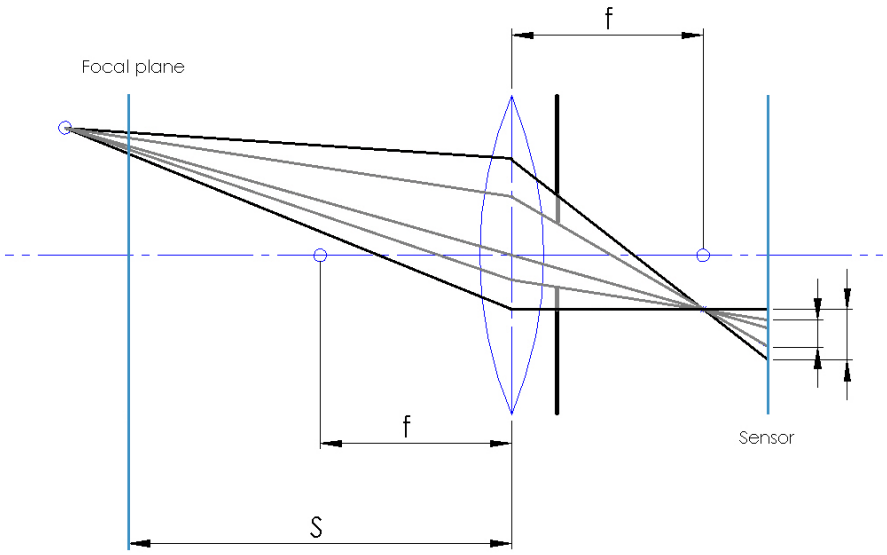

Figure 2.22 Effect of aperture diameter on blurring of out of focus objects, with grey rays representing a small aperture diameter, and black rays representing a large aperture diameter

Figure 2.22 shows the effect of aperture diameter on the circle of confusion in an image, all other factors being equal. Both of these options have trade-offs:

Increasing distance to subject: Increasing the distance between the subject and the camera increases the depth of field, but also increases the physical distance represented by each pixel (for a fixed field of view, doubling the distance will double the physical distance represented by each pixel). As a result of increasing the camera to subject distance, the effective resolution (in metres) of the DIC measurements will decrease.

Decreasing aperture diameter: Decreasing the relative aperture diameter (increasing the f number) will increase the depth of field, but reduce the amount of light entering the camera. This reduced light can be offset by:

1. Increasing the shutter time: Increasing the shutter time will allow more light to enter the camera, but will increase blurring of images. Additionally, the maximum shutter time is inversely proportional to the frame rate - high speed photography will require short shutter times.

2. Increasing the amount of light on the subject: Increasing the brightness of the light on the subject will increase the amount of light entering the aperture, allowing for higher f numbers. Where possible, this is preferable to increasing shutter time.

Note that c is traditionally taken to be equivalent to one pixel, but Van Mieghem *et al* (2017) showed that this is an overly conservative value for DIC purposes, and that adequate DIC results can be achieved with a less strict definition of c and images that would traditionally be considered unfocussed.

2.6.4 High speed 3D DIC

The DIC technique has no inherent limitation on the velocity and duration of the measured event, with the main limitations resulting from a difficulty in capturing sufficient high quality images. DIC has successfully been used to measure high speed events - Curry (2017) [37] captured the deformation field of steel plates undergoing air-blasts and buried explosions, using a frame rate of 30 000 fps, an exposure of 31 μ sec, and a resolution of 1024x76 pixels. Where robust cameras are not required, *Vision Research* offers cameras allowing for stereoscopic DIC at frame rates as high as 1000 000 fps (at a resolution of 128x32 pixels)[50]. As a result of the high frame rate and low exposure time, obtaining sufficient lighting is particularly challenging for high speed DIC - extra lighting is required. The tests conducted by Curry (2017)[37] required two custom build LED lights with diffusers in order to ensure sufficient lighting whilst avoiding localised over-exposure.

Chapter 3

Device Design

Contents

3.1 Design requirements of device

Basic sizing requirements

1. Apparatus to fit on Split Hopkinson Pressure bar trestles in BISRU lab, and to be useable on any sufficiently large flat surface (allowing for use in labs other than BISRU)
2. Apparatus to be useable by a single human within 90% of anthropomorphic data
   (a) Each individual part to weigh $\leq$ 15kg, and fit into standard sedan (allowing easy transport where necessary)
   (b) (Diss)assembly and operation by a single person to be possible
3. Apparatus to be powered either electrically or pneumatically:

Electrically powered: to be useable with 220/230V 50Hz electrical power

Pneumatically powered: to be usable with 10 bar workshop air, as well as with higher pressure gas cannisters.

Performance requirements

1. Humidity and temperature control not required:
   (a) Tests by Tonge *et al* showed negligible effects of humidity on skin [1].
   (b) Temperature has a significant effect on skin's properties [2], but temperature control is outside of the scope of this project. The device should be designed such that temperature control can be added by future users if needed.

2. Average strain rate of $10s^{-1}$ to $100s^{-1}$ to be achievable

   Variation in strain rate to be minimised

3. A range of biaxial strain ratios to be achieved at the specimen region of interest/gauge section:

   Equi-biaxial strain to be achieved

   Strain ratio up to 4 to be achieved

4. Specimen size to be up to 50mm diameter

5. Boundary conditions should minimise slippage of the membrane, and be easily repeatable between specimens.[1]

3.2 Initial concepts and design

A high strain rate biaxial tensile test similar to the low strain rate apparatus covered in section 2.4.2 was briefly considered, but decided against:

1. A major advantage of bulge tests is that preconditioning does not occur, and bulge tests are thought to be more representative of *in vivo* conditions [1].

2. Bulge tests have simple, consistent boundary conditions, unlike the complex boundary conditions of most planar tension tests.

3. Biaxial tension tests are relatively easy to control at low strain rates, but would be challenging to control at high strain rates. Some form of biaxial SHPB apparatus would likely be needed if high strain rates were to be achieved.
   (a) Uniaxial SHPB tension tests on soft tissue or elastomeric materials are challenging due to problems with clamping and force measurement.
   (b) Biaxial SHPB tensile testing is likely to be particularly difficult to synchronise and reliably operate, even for materials like mild steel.

[1] Tests by Bentil *et al* (2016) [34] appeared to have slipping at membrane boundaries, which is undesirable

For these reasons a high strain rate planar biaxial tensile test apparatus was not considered practical. Further concepts focussed on bulge testers adapted for high strain rates.

Two primary initial concepts for a bulge tester were considered:

1. A shock tube, where the bursting of a membrane triggered the start of a test, allowing high pressure gas to fill a cavity and pressurise the membrane
2. A free piston driven device, where a free piston pressurises a volume of air, which in turn causes the bulging of the membrane.

Previous bulge testing of skin has been done using saline solution as the driving fluid [1], but air was chosen as the driving fluid given the accelerations and velocities expected. Accelerating substantial volumes of water to high speeds will take large amounts of pressure. Previous high strain rate bulge testing of silicone has used helium as the driving fluid [34], but air was chosen due to ease of acquisition and use. Future iterations of this project may wish to use helium.

3.2.1 Shock tube

Advantages of building a shock tube include:

1. The BISRU laboratory has built shock tubes in the past, and has shock simulation code [2] suitable for the design of shock tubes.
2. A shock tube could potentially be used for other projects as well, such as cheaply simulating blast waves or similar events.
3. Shock tubes are generally mechanically simple and robust, with few moving parts.
4. Bentil *et al* (2016) [34] conducted high strain rate inflation tests on elastomers using a shock tube apparatus. This would allow comparison with external data

Disadvantages of building a shock tube include:

1. In order to increase the duration of the pressure wave supplied by a shock tube, it is necessary to increase the size of the shock tube reservoir. This in turn increases the size and weight of the device, making it difficult to satisfy the basic sizing design requirements. Figure 3.1 shows a typical shock tube pressure profile generated with a driving section 1209mm long. Note that the relatively flat pressure wave only lasts approximately $5ms$ even with a $1209mm$ driving section.
2. It is difficult to tailor the pressure profile of a shock tube. Once the pressure profile has been selected, it is difficult to change the profile between experiments. Short of major modifications, the only easily changeable variables are the initial pressures of the driving and driven sections of the tube.
3. This project aims to develop a dynamic bulge test with a strain rate as close to constant as possible. The pressure profile of a shock tube (shown in fig. 3.1) will look nothing like those shown in fig. 3.2. As a result, the strain rate resulting from a shock tube will be highly non-constant, dominated by dynamic effects, and difficult to modify.

[2] Written by a 4^{th} year Mechanical Engineering student, Benjamin Alheit (2017)

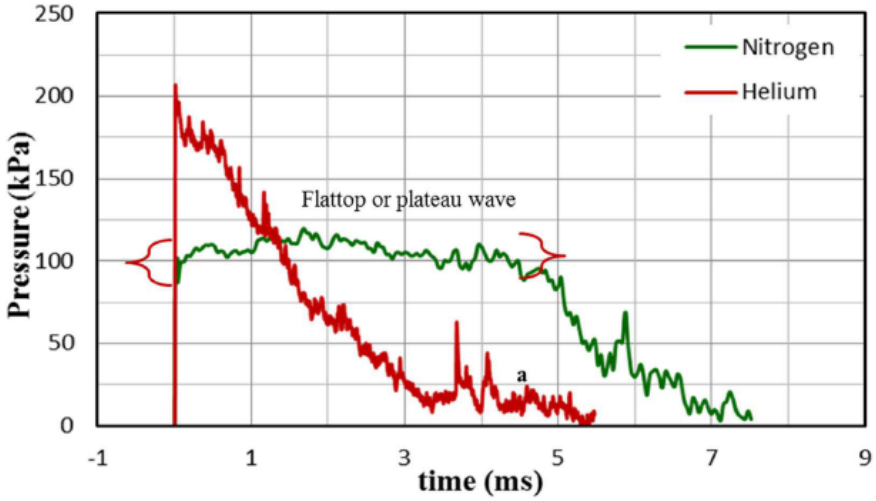

Figure 3.1 Pressure profile for nitrogen and helium, in a shock tube with a driving section of 1209mm. Figure taken from Sundaramurthy *et al* (2014) [51]

3.2.2 Free piston

The initial concept behind the free piston device was to use the movement of a high velocity free piston to pressurise a volume of air, with the pressurisation profile controlled by the mass, geometry, and initial velocity of the piston. This would give a slower pressure rise than a shock tube device, but would not require high speed feed-back electronics and control. The pressure in the driven volume of air can be measured, allowing one to calculate the forces acting on the membrane. Advantages include:

1. This device is likely to be significantly smaller and lighter than a shock tube providing similar pressure over the same duration.
2. A free piston device has more easily changeable variables than a shock tube, allowing for one to more finely tailor the performance of the apparatus with regards to strain experienced by the specimen. Only the driving pressure can be easily changed in shock tube apparatus, whilst a free piston device can easily change the piston mass and the driving pressure in order to tailor strain rates.
3. The pressure profile due to a free piston is likely to more closely match those shown in fig. 3.2.
4. With minor modifications, this device could likely be used for high strain rate bulge tests of other materials at the BISRU laboratory in future.

Disadvantages include:

1. This device appears to be relatively novel, and as such is much more likely than a shock tube to experience teething problems. Shock tubes are well described in the literature.
2. This device is mechanically more complex than a shock tube:

   There are more parts

   There are more moving parts

   The required tolerances are finer

3.3 Concept selection and simulation

The bulging of a membrane was modelled using the quasi-static sphere section assumption, as well as simple FEA code written in Matlab (which took rate dependent effects as well as inertia into account). The simple FEA simulation modelled both a shock tube and a simplified free piston apparatus, in order to assess the author's opinion that the free piston would result in a superior strain rate response to the shock tube.

3.3.1 Quasi-static analysis

Using the sphere section assumption described in section 2.5.3.1 and material parameters taken from Shergold *et al* (2006) [22], driving pressure vs apex strain curves were generated for circular membranes with a thickness of 2mm and a diameter of 50mm. If a constant strain rate is required (and dynamic effects are ignored), then the pressure profile should look like those shown in fig. 3.2. The derivations and code used to generate fig. 3.2 are shown in appendix A.

Material	**Material model**			
	Mooney-Rivlin		**Ogden**	
	$C1$ (MPa)	$C2$ (MPa)	α	μ(MPa)
B452 Silicone	0.5	0	3	0.4
Human skin	0.3	0	9	0.11

Table 3.1 *Material parameters for B452 silicone and human skin taken from Shergold* et al *(2006) [22]*

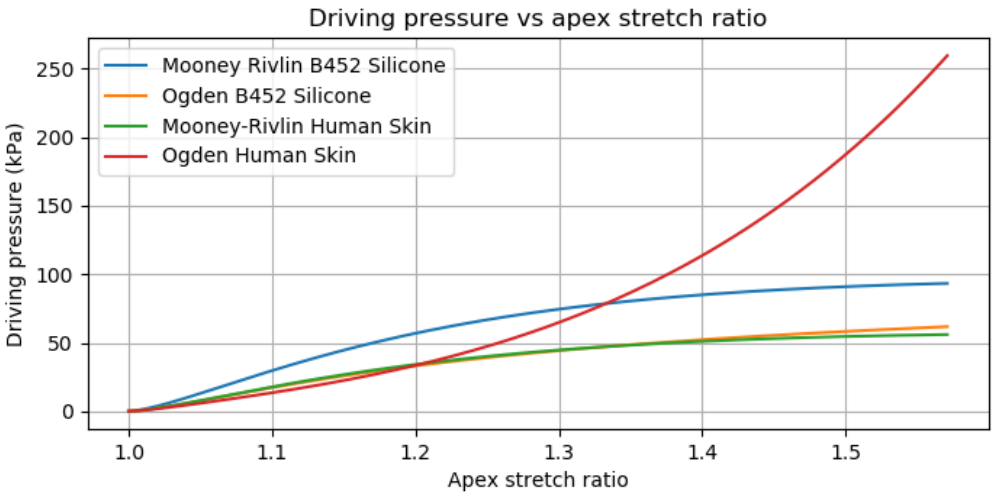

Figure 3.2 Membrane pressure vs apex stretch ratio for membranes of various materials. Note that this plot is identical to a pressure:time plot of a constant strain rate bulge test, if dynamic effects are ignored (as the x axis will simply be linearly scaled by a factor of the strain rate)

Whilst fig. 3.2 implies that a free piston will give superior results to a shock tube, it does not take dynamic effects such as inertia or viscosity into account.

3.3.2 Simple FEA

As this FEA was part of the design and concept selection process (rather than a high fidelity prediction), the membrane material model was simplified to a visco-elastic solid, rather than the full non-linear, anisotropic, heterogeneous model required for real skin.

P1 (3 noded linear) shell elements were used due to their simplicity, robustness, and computational efficiency. Bending stiffness was ignored, as the membrane had a low thickness:diameter ratio. Quarter symmetry, pre-inversion of matrices, and mass lumping were used for computational efficiency. This FEA code confirmed that the free piston device resulted in a superior[3] strain rate profile compared to a shock tube.

3.3.3 Concept chosen

Both quasi-static nonlinear hyper-elastic analysis and dynamic linear visco-elastic analysis indicate that the free piston driven device will result in a more constant strain rate than a shock tube would. As a result, the free piston was chosen as a pressure supply method.

3.4 Design and Operation of bulge tester

The operation of the bulge tester consisted of 2 primary stages: acceleration of the piston, and pressurisation of the membrane. When the vents at the midpoint of the pump tube were closed, these stages were merged - allowing for greater membrane pressures, and changing the pressurisation profile. The piston acted as the valve between the reservoir and the driving section of the pump tube, allowing for consistent firing of the piston.

3.4.1 Operation of bulge tester

[3] I.e. a strain rate with less variation throughout the test

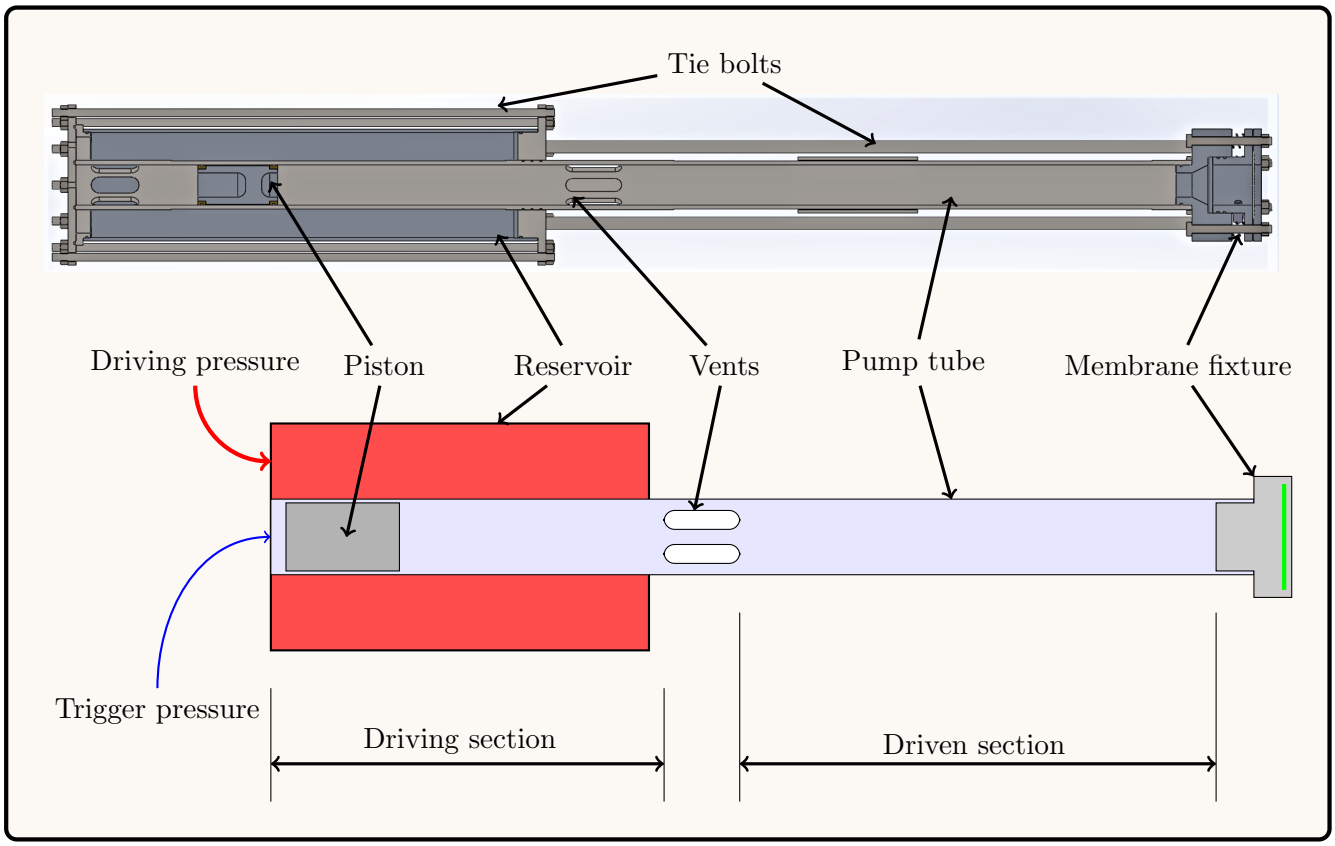

Figure 3.3 Bulge tester schematic (not to scale) and cross section

3.4.2 Firing steps

1. The reservoir and trigger are vented to atmosphere, and the piston is pushed to the back of the driving section with the push rod. A membrane specimen is clamped in the membrane fixture. All sections are at atmospheric pressure.

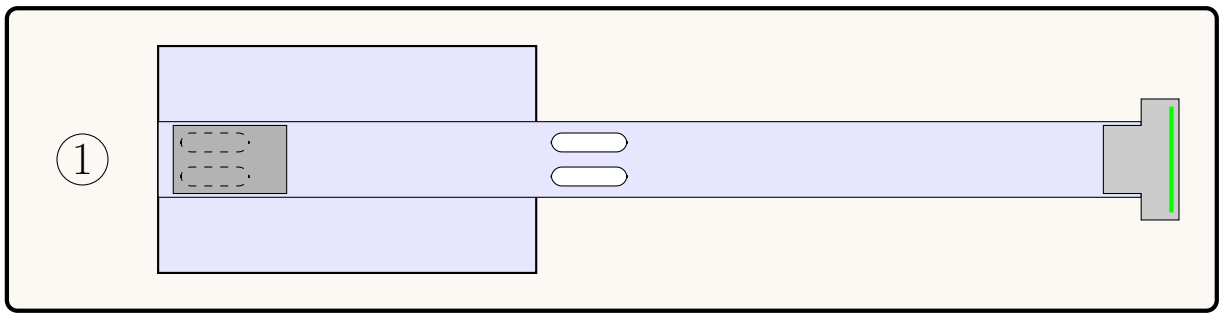

Figure 3.4 Loaded, unpressurised bulge tester. Ports between reservoir and pump tube (obscured by piston) shown with dashed lines

2. The reservoir is pressurised to a chosen driving pressure. During this time the pump tube in front of the piston is vented to atmosphere due to the central vents, and the section of pump tube behind the piston is vented to atmosphere by the pneumatic control circuitry. Small leaks from the reservoir past the piston seal have no effect. The lights are turned on, and the high speed cameras and oscilloscope set to wait for the trigger signal.

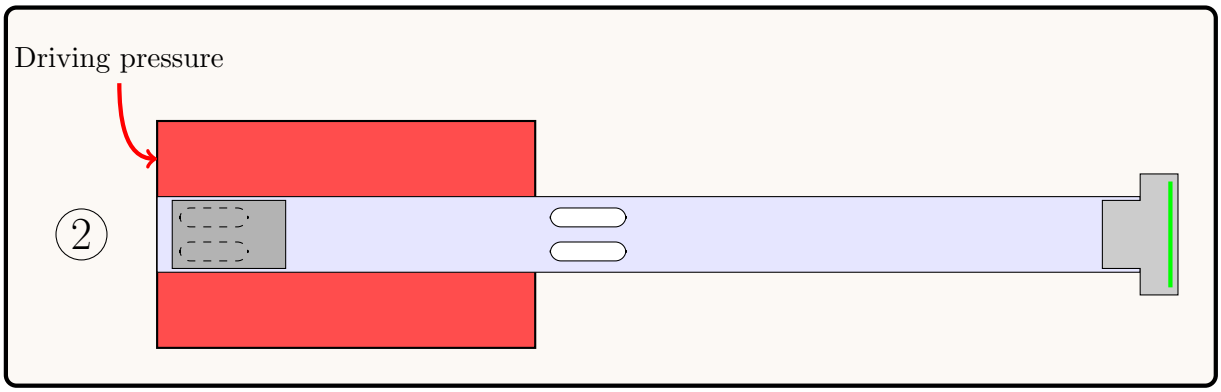

Figure 3.5 Loaded, pressurised bulge tester

3. The valve venting the trigger section to atmosphere is closed, and the trigger pressed. This sends a 4.5V step pulse to the cameras and oscilloscope, and introduces a small amount of high pressure air behind the piston, moving it forwards slightly. The compressed air flow from the trigger is sufficient to move the piston slightly, but flows too slowly to provide significant velocity to the piston.

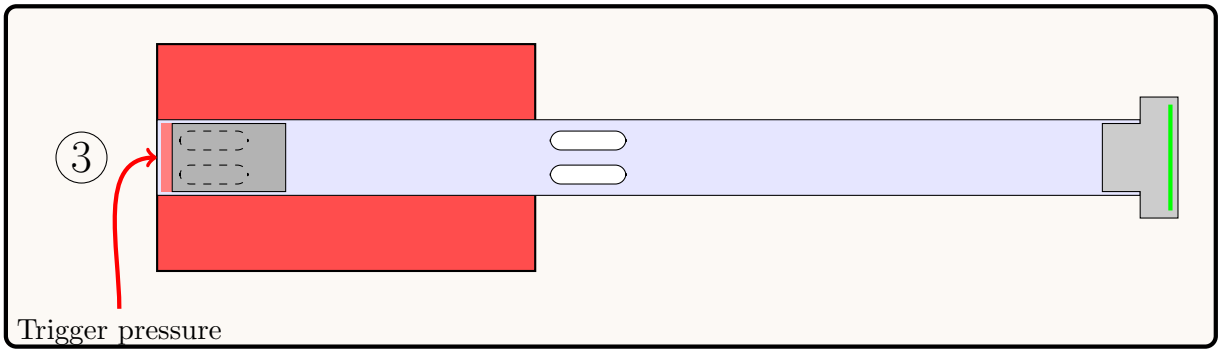

Figure 3.6 Trigger pressure supplied, piston starts moving forwards slightly

4. Once the piston has moved forward 1cm, the ports between the reservoir and the driven section of the pump tube are exposed. This allows the high pressure air of the reservoir to enter the pump tube, moving the piston forward. The piston accelerates forwards, and the central vents ensure that the driven section of the pump tube stays at atmospheric pressure. The driving pressure is supplied almost entirely by the reservoir, and the trigger pressure has a negligible effect on piston velocity.

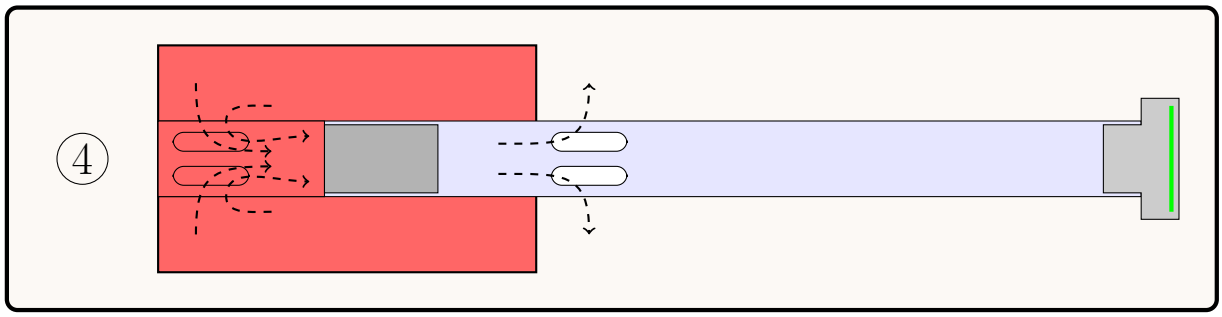

Figure 3.7 Piston accelerating forwards. Dashed lines represent airflow from the reservoir to the driving section of the pump tube, and from the driven section of the pump tube to atmosphere. Driven section still open to atmosphere, and nominally at atmospheric pressure

5. The piston passes the vents, crossing from the driving section of the pump tube to the driven section. The pressure behind the piston is now vented to atmosphere, and the pressure in front of the piston (in the driven section of the pump tube) starts rising due to (nominally) isentropic compression. The membrane (shown in green) begins to bulge.

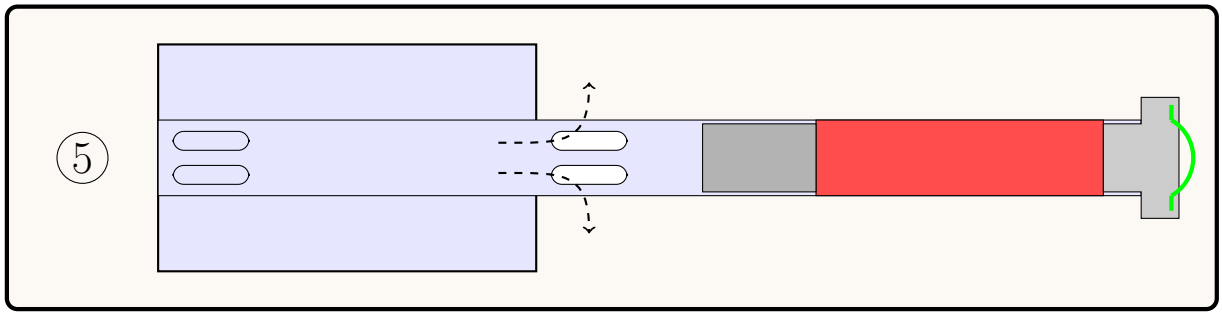

Figure 3.8 Piston compressing air in driven section of pump tube. Driving pressure vented to atmosphere via vents, resulting in nominally atmospheric pressure behind the piston. Membrane starts to bulge

3.5 Specific design features

3.5.1 Piston

3.5.1.1 Effect of piston mass

If the effect of the membrane on the volume of the driven section is assumed to be negligible, the pressurisation profile will be dependant on the energy and velocity with which the piston enters the driven section. For a fixed piston energy, the pressurisation rate will nominally be proportional to $v_{piston} \propto \frac{1}{\sqrt{m_{piston}}}$. As a result, a range of pistons were created, with masses ranging from 400g to 1600g.

Lower limit on piston mass: In order to prevent rocking of the piston, there is a lower limit on the length:diameter ratio of the piston: locking will occur at $L \leq \mu D$. In addition to the limit imposed by frictional effects, the quick release valve system sets a lower limit on piston length. The piston is

used as the valve, with the valve cross sectional area being directly proportional to piston length. If the valve's cross sectional length is too low, there will be choking of the flow of pressurised gas driving the piston. In practise, the limiting case was due to port length (as the piston:tube friction was low).

3.5.1.2 Friction between piston and pump tube walls

The pistons contacted the pump tube walls via phosphor bronze or PTFE bushings and rubber O rings.

Bushings The bushings appeared to have negligible friction compared to the rubber O rings, particularly as it was a clearance fit.

O rings The static friction due to the O rings was substantial (equivalent to approximately 100-200 N, or 50-100 kPa driving pressure). Once the piston started moving however, the O rings lost direct contact with the pump tube due to the hydrodynamic effects of the oil film [4] on the pump tube walls. This greatly reduced the effect of friction, to approximately 20N (equivalent to 5kPa driving pressure). At higher piston velocities this force would greatly increase, but this was not measured.

The static friction was measured by placing the piston midway down the pump tube and then gradually increasing the pressure behind it until it stated to move. This pressure difference was 50-100 kPa, or 100-200N.

3.5.2 Effect of central vents

For isentropic compression in a closed ended cylinder of length L with piston position x, the pressure and pressurisation rate are:

$$P = P_0 \left(\frac{L}{L-x} \right)^k \tag{3.1}$$

$$\dot{P} = P_0 \frac{k}{L} \left(\frac{L}{L-x} \right)^{k+1} \dot{x} \quad = \quad P \frac{k}{L-x} \dot{x} \tag{3.2}$$

This shows that the pressurisation rate is proportional to the current pressure and piston velocity, and inversely proportional to the remaining cylinder volume. For materials with a relatively low strain hardening co-efficient (α in the Ogden model, see table 3.1), a decreasing pressurisation rate is needed (see fig. 3.2).This is achieved by opening the vents, as the piston enters the driven section at high velocity (when the pressure is low), and slows down as the pressure increases.

For materials with a high strain hardening co-efficient (such as skin), the pressurisation rate needs to continually increase with time. This is achieved by closing the vents, causing the pressure rate to increase with time.

Note that both of the above scenarios only apply under the assumption that the piston has sufficient energy to move forwards throughout the test. If the membrane is stiff enough, the piston will slow down and then start moving backwards - leading to unloading of the membrane and a negative pressurisation rate.

[4] The pump tube walls and O ring grooves were lubricated with compressor oil, improving both friction and sealing characteristics of the O rings

The above calculations neglect the effect of the membrane on the volume of the chamber. As a result, these calculations are an approximation that holds true only when the volume of the membrane bulge is significantly lower than the volume of the cylinder.

3.5.2.1 Noise

A significant downside to the vents is the large amount of noise generated when the driving pressure is vented to atmosphere. A suppressor was built, which consisted of an expansion chamber with walls consisting of alternating rubber and microfibre textile layers, and baffles constructed from dense copper wire mesh. This suppressor was closely based on the design of typical fire-arm suppressors.

This suppressor was found to be unnecessary. Sound level measurements at 5m from the device were below 95dB for driving pressures up to 750kPa. The peak noise level in the offices adjacent to the laboratory was below 80dB. As such, the use of ear protection by the operator was sufficient to mitigate the noise, particularly given the short noise duration[5].

If tests are conducted at higher driving pressures in the future, it may be necessary to use the suppressor.

3.5.3 Pneumatic control

3.5.3.1 Pneumatic circuit

Table 3.2 *Pneumatic circuit components*

Component	Function
1	Trigger circuit isolation valve. Isolates the trigger circuit from source pressure.
2	Trigger. Triggers the bulge tester when pressed, and simultaneously sends a 4.5V step pulse to trigger the cameras and pressure sensor.
3	Trigger circuit vent. Vents the trigger circuit to atmosphere, and prevents any leaks past the piston from causing premature firing.
4	Pressure regulator. Used to step the supply pressure down to the selected reservoir pressure.
5	Reservoir isolation valve. Used to isolate the reservoir from the supply pressure.
6	Reservoir circuit vent. Used to vent the reservoir pressure to atmosphere.

[5]According to safety regulations, ear protection is not required by the operator given the noise levels and durations. The noise was unpleasant however, and operator ear protection was judged to be prudent (particularly given the uncertainty associated with noise level measurements)

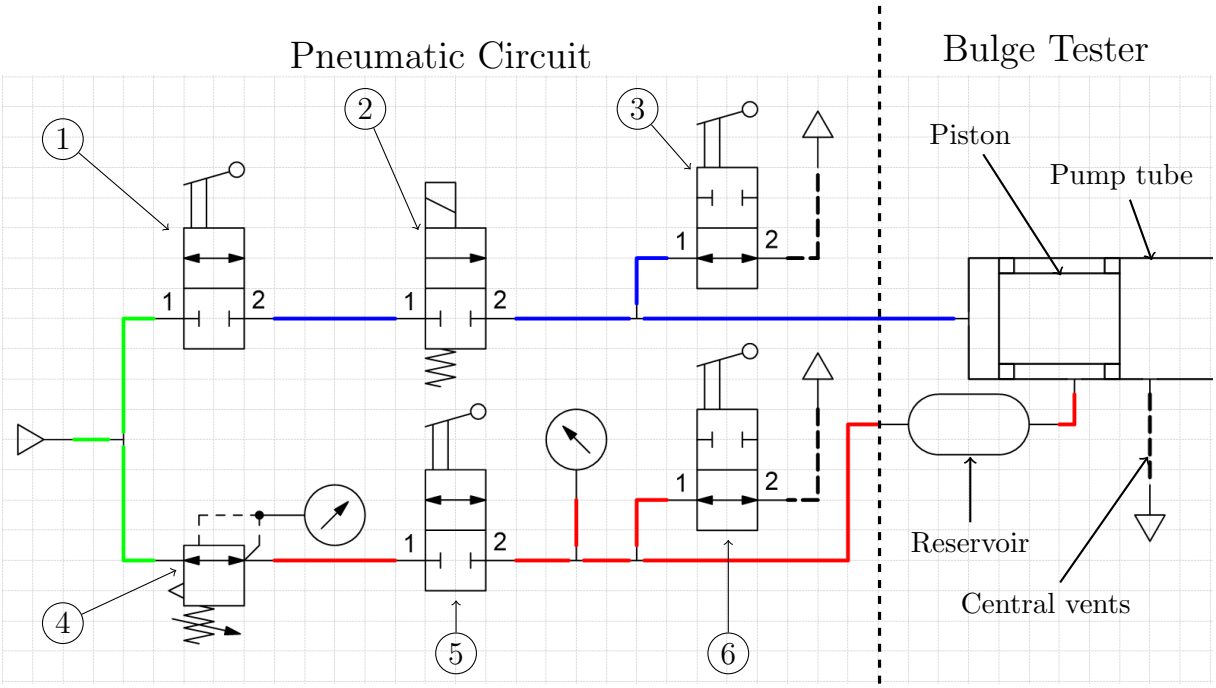

Figure 3.9 Diagram of pneumatic control system. Valves are shown in the unpressurised configuration. Red lines represent the reservoir pressure side of the control circuit, blue lines represent the triggering side of the control circuit, green lines represent the supply air, and dashed lines represent vents to atmosphere. Bulge tester is shown as a functional diagram, which is not representative of the physical device

Figure 3.9 shows the pneumatic control system when the bulge tester is unpressurised. Valves 1, 5 and 6 were not strictly necessary, but were included in order to reduce the chance of an accidental firing, and to allow for easy venting of the reservoir. The pressure gauge between valves 5 and 6 was included as it had a higher resolution than the pressure gauge on the regulator (valve 4).

3.5.3.2 Piston valve

Figure 3.10 shows the piston valve/trigger mechanism in detail. The large slots in the pump tube allow pressurised air from the reservoir to enter the driven section of the pump tube when the piston is not blocking the vents. When the piston is in the unfired position, the front O ring seals the reservoir off from the front section of the pump tube. The rear O ring prevents reservoir pressure from travelling backwards, and prematurely firing the piston.

The reservoir was pressurised to 850 kPa with no observable leaks after 8 hours, but as the O rings wear there are likely to be minor leaks. Figure 3.10 shows the path of these leaks with a dashed red line, and how they are vented via the triggering port in order to prevent premature firing.

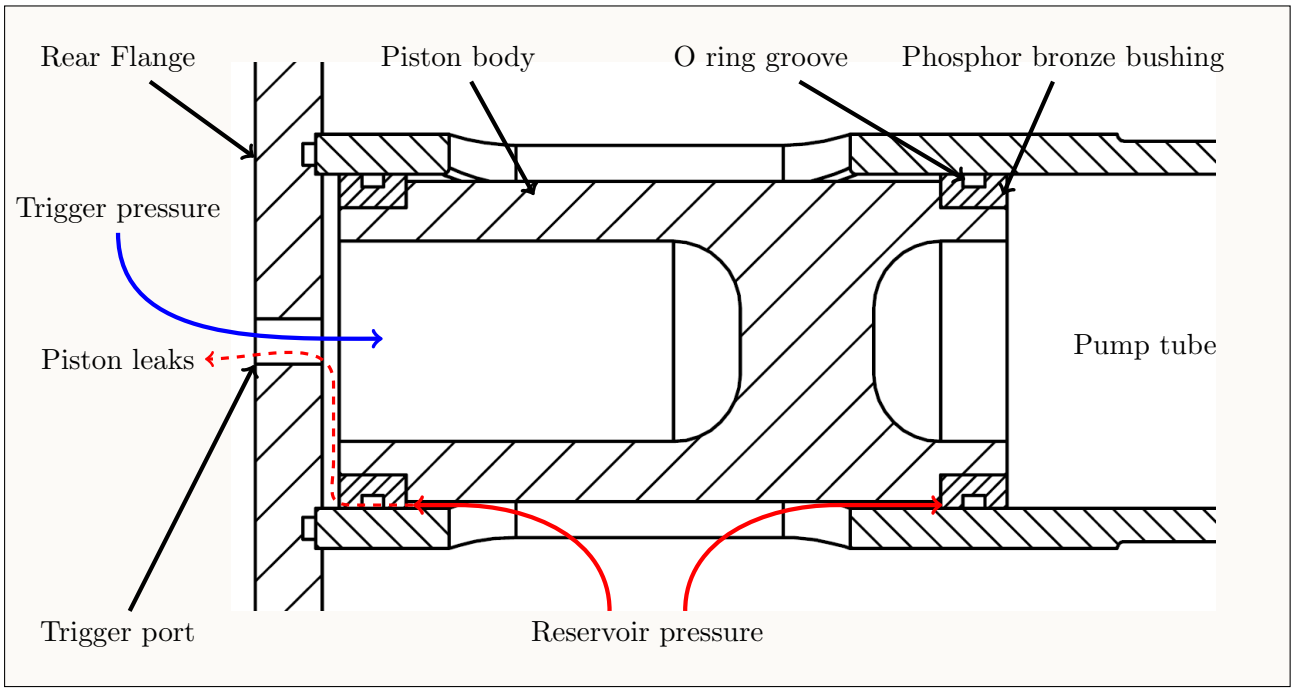

Figure 3.10 Piston trigger mechanism

3.5.4 Safety

Due to the hazards associated with pressure vessels and high velocity pistons, the following safety considerations were made during apparatus design.

3.5.4.1 Leak before break

All pressure vessel parts were designed with ductile materials and a safety factor on yield of at least 4.5, assuming 3 MPa driving pressure. Note that for the materials of interest in this project, pressures below 800 kPa were sufficient. Where possible, materials with a large ductile regime (such as mild steel) were used. The O-ring seals used were all nominally rated for 6 MPa pressure - the O rings should fail prior to any plastic deformation of metal structural components. One of the reservoir seals was an axial seal, and one was a radial seal. The axial seal was designed to leak due to joint separation before the tie rods etc entered the plastic regime. The radial seal ensured that the reservoir would leak as soon as it entered the plastic regime, and long before fracture.

If the reservoir pressure is increased indefinitely, the following failure modes are anticipated:

1. 6 MPa: O rings fail, leaks occur, pressurisation slows/stops
2. 9.7 MPa: Elastic (axial) joint separation ($0 - 0.2mm$), leaks occur, pressurisation stops
3. 14 MPa: Reservoir begins to yield[6]. Radial joint separation, pressurisation slows/stops
4. 14.1 MPar: Tie rods start to yield, significant axial joint separation ($> 0.2mm$), leaks occur, pressurisation stops

[6]Due to difficulty obtaining parts, a reservoir with lower strength was used. Given that reservoir pressure did not go above 1 MPa, this was acceptable. If the bulge tester is used over the full design range (up to 3 MPa reservoir pressure) in future, the originally specified reservoir should be used.

5. 27 MPa: Originally specified reservoir begins to yield.[7]

A summary of the equations used to calculate the above figures can be found in appendix C.

If the O-ring seal does not fail, joint separation due to elastic deformation of the tie rods will occur at a reservoir pressure of approximately 9.7 MPa. Pressurisation past this point is unlikely to occur, as elastic joint separation of up to $0.2mm$ will occur before the bolts enter the plastic regime.

If the pressurisation rate is sufficient to overcome the leaks due to $0.2mm$ joint separation, the bolts will undergo plastic deformation at 14.1 MPa of reservoir pressure. The bolts are capable of undergoing significant ductile elongation before fracture, making catastrophic bolt failure unlikely.

Inducing a catastrophic failure due to pressure would require overtorquing the tie rods well into the plastic regime (inducing necking), and then pressurising the reservoir. Inducing fracture in either the originally specified reservoir or the replacement reservoir is not feasible, as sealing will be lost long before fracture will occur.

3.5.4.2 Piston containment

In the event of a "dry firing", the piston will hit the membrane fixture at high speed. It is important that the piston remain within the device should this occur. Should the piston hit the membrane fixture at high speed, the energy will be transferred into the tie rods bolting the membrane fixture to the central flange.

If a metallic piston is allowed to directly impact the clamp fixture, approximately $78J$ of energy are required to induce plasticity in the tie rods (detailed calculations in appendix C)[8].

As a result, 3 plastic spacers were placed in series between the piston and the clamp fixture:

1. One 10mm thick 3D printed sacrificial ABS disc. This disc was designed to be crushed as soon as any significant force went through it, indicating that piston impact was occurring. Given the poor mechanical properties of 3D printed parts, this disc was not expected to absorb significant energy
2. One 20mm thick Sorbuthane®vibration damping elastomeric disc. This material is highly elastic with significant viscous effects, and has previously been used to stop a similar piston in a 2 stage gas gun at BISRU labs.
3. One 20mm thick sacrificial HDPE disc. This disc is designed to plastically deform in the event of an unplanned high velocity piston impact. HDPE is highly ductile, allowing it to absorb large amounts of energy when plastically deforming.

Additionally, the clamp fixture is significantly heavier than the piston (approximately 6.6kg). In the event that the tie rods fracture and the clamp mechanism flies forwards, it will be moving slowly for a given amount of energy. This will reduce the distance that it travels in the event of a containment failure. It should be noted that a containment failure is not anticipated, and this is simply a precaution.

[7] This calculation is fairly meaningless. Reaching this pressure without leaks would involve a substantial redesign of the bulge tester, which would in turn change the boundary conditions used to calculate this burst pressure.

[8] It would take significantly more energy to completely fracture the tie rods and allow the piston to leave the pump tube, but plasticity is taken to be a failure criterion. If the bolts are allowed to plastically deform slightly with each firing, a fracture event is likely to eventually occur

3.5.4.3 Fatigue failure

Given that this bulge tester is a prototype, it is expected to undergo a limited number of use cycles. This (combined with the high safety factor on yield) makes fatigue failure unlikely. As a result, fatigue strength calculations were not done. If future users plan to undertake a significant number of tests (≈ 1000), fatigue failure calculations should be done.

Chapter 4

Specimen materials and preparation

Contents

4.1 Materials chosen

Finding a readily available skin simulant with identical properties to skin is highly unlikely. Instead of trying to exactly emulate skin, 3 different materials were tested, with a greater inter-material range of properties than skin exhibits. This allowed the bulge test methodology to be validated over a wider range of strains, moduli, and transverse stiffness ratios than anticipated for skin or other biological membranes.

Three materials were tested, two types of Polydimethylsiloxane (silicone) elastomer and one textile reinforced silicone elastomer:

1. *Dragon Skin 10* from *Smooth-On Inc.*
2. *Mold Max 60* from *Smooth-On Inc.*
3. Textile reinforced *Dragon Skin 10.*

Silicone was chosen over other elastomers (such as rubber or polyurethane) as it was food safe, readily available and easy to cast. Additionally, it was hoped that the silicones chosen would exhibit the significant strain hardening behaviour demonstrated by many of the silicones tested in the literature[52, 53, 54], emulating the strain hardening behaviour of skin. The selected PDMS elastomers have not been extensively tested in the literature. Some testing has been conducted on Dragon Skin 10, however

the maximum strain was only 25% and the test method was via indentation testing [55]. As a result, the manufacturer's data-sheet was the primary source of information when considering this material.

Two other skin simulants were experimented with in the initial material selection phase, but were not used. Appendix B describes these materials in more detail.

4 different membrane shapes were tested (ellipses with major diameters of 50mm and minor diameters of 50,40,30 and 20mm) in order to test different biaxial strain states (the strain in the direction of the minor axis of the ellipse will generally be greater, if the material is isotropic).

4.1.1 Dragon Skin 10

Dragon Skin 10 is a highly pliant Shore 10A platinum cure silicone with an elastic modulus of approximately 150 kPa and an elongation at break of 1000%[1][56]. It was chosen as it has similar elastic properties to skin in the toe region (E_y of approx 150kPa vs approx 126 kPa [1]). An additional reason for choosing this material was the high elongation at break - this would allow for the DIC method to be validated over a larger range of strains than expected when testing skin. Pure Dragon Skin 10 silicone is clear and highly viscous when uncured, so a small amount of silicone thinner (Dimethylsiloxane) and white silicone pigment (primarily titanium dioxide) were added. The final mix ratio was 50:50:1:1 part A to part B to pigment to thinner by mass.

The addition of the thinner allowed for the casting of bubble free parts without the use of a vacuum chamber, and the addition of the pigment turned the silicone opaque - allowing the high speed cameras to more accurately record images of the surface. Both the thinner and the pigment cause a slight decrease in the stiffness and strength of the silicone[57, 58] relative to pure Dragon Skin 10.

4.1.2 Mold Max 60

Mold Max 60 is a Shore 60A tin cure silicone with an elastic modulus of approximately 2.3 MPa and an elongation at break of 130% [59]. This silicone was chosen to be stiffer than skin simulants typically used in the literature (such as 40 Duro[2] polyurethane [60]), in order to test the device over a wider range of moduli than anticipated for skin or other biological membranes. Mold Max 60 was the stiffest castable silicone elastomer readily available.

4.1.3 Textile reinforced silicone

Dragon Skin 10 silicone was reinforced with cotton based bandage material. This material was highly anisotropic: the weft direction consisted of straight cotton fibres, but the warp direction consisted of a combination of straight elastomer fibres and highly crimped cotton fibres. As a result of this, the weft direction of the material was stiff but the warp direction exhibited low initial stiffness with a high degree of strain stiffening as the warp fibres straightened out. The textile was chosen both for its high degree of anisotropy as well as the strain stiffening behaviour exhibited in the warp direction.

This material was embedded in a matrix of 10Duro silicone - the silicone matrix being analogous to elastin and the cotton fibres being analogous to collagen. Figure 4.1 shows an example of textile reinforced clear Dragon Skin 10 silicone. Note the high degree of crimping exhibited by the cotton warp fibres. Additionally, note the presence of air bubbles in the silicone - unlike the pure silicone samples,

[1] These values are taken from the data-sheet, and are used as ballpark figures

[2] Duro refers to Durometer, and is a measure of rubber stiffness. 60 Duro refers to a polymer with a stiffness of 60 on the Durometer scale

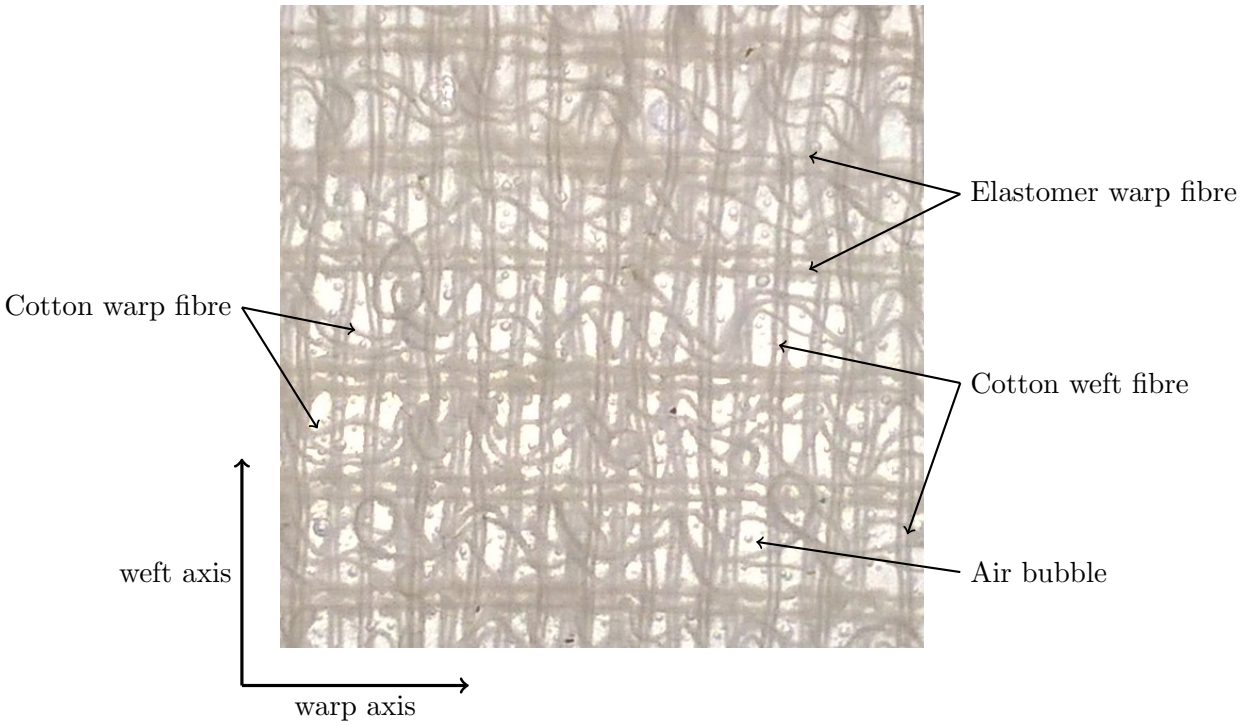

Figure 4.1 Textile reinforced silicone sample (clear), showing weft and warp fibres

the textile reinforced samples had some entrained air bubbles. The use of a vacuum or pressure chamber when casting would remove these bubbles, and it is suggested that a vacuum casting process is used if this material is made in future. This material was heterogeneous due to the randomness of the warp fibres as well as the presence of small bubbles in the silicone matrix.

Whilst this sample shown contains one layer of textile cast in clear silicone, the samples tested consisted of 2 layers of textile (with matching weft and warp axis) cast in white pigmented silicone.

This material had a significantly higher transverse stiffness ratio than skin, allowing the bulge test methodology to be validated for a material that exhibits a greater degree of anisotropy than expected from skin or other biological membranes.

4.2 Specimen preparation

4.2.1 Membrane shape

Four different elliptical membrane shapes were used, all with a major diameter of 50mm. The minor diameters were 20, 30, 40 and 50 mm [3] respectively. The reason for this was to allow for differential strain in the major and minor axis directions - the apex strain in the minor axis direction would be greater than the apex strain in the major axis direction for a given bulge height (see section 2.5.3.2). For isotropic membranes, the apex strain ratio would nominally be inversely proportional to the square of the major:minor diameter ratio - as a result, the strain ratio for isotropic membranes is expected to be approximately 1, 1.6, 2.8, and 6.25. Note that this is an approximation, and not expected to hold true (particularly at high strains and strain rates).

[3] i.e. a circle

When the membrane material was anisotropic (textile reinforced silicone), the stiff axis of the material was always aligned with the major axis of the ellipse.

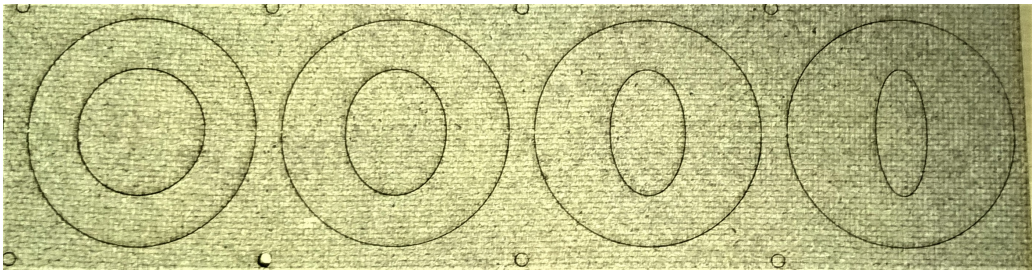

Figure 4.2 Laser cut Masonite membrane clamps. The outer ring bonded to the specimen, and the inner ellipse was removed, giving the effective membrane shape. Each inner ellipse has a major diameter of 50mm. From left, the minor diameter is 50,40,30, and 20mm. The outer diameter of each Masonite ring is 90mm, as shown in fig. 4.3

4.2.2 Membrane fixation method

Clamping soft elastomeric or biological materials is particularly challenging, as they are often effectively incompressible with a low shear modulus.

4.2.2.1 Friction based methods

Any significant clamp force leads to material flow inwards, causing significant deformation of the membrane prior to the application of pressure. As a result, relying on friction to clamp soft elastomeric or biological material is not feasible if the membrane is to be undeformed and stress free prior to testing. Additionally, the thickness of the membrane will decrease as it is stretched (due to incompressibility), causing the grips to lose contact near the edges of the membrane, allowing inward slippage. This method was used by Bentil *et al* (2016) [34] on relatively stiff silicone, and appeared to result in some slippage.

4.2.2.2 Adhesive based methods

Tonge *et al* [2014] [1] clamped skin for quasi-static bulge testing through the use of large amounts of cyanoacrylate adhesive (commonly known as "super glue"). This worked well, as cyanoacrylate bonds well to moisture containing biological tissue, and has an elastic modulus significantly higher than that of skin. This provided grip force for the skin without the bulging associated with friction based methods, and prevented undue compression of the skin in the clamp (due to the high relative stiffness of cured cyanoacrylate).

The skin simulants used in this series of experiments are all silicone based, making an adhesive based fixation method challenging. Silicone is impervious to most commercial adhesives, and does not bond to most carbon based molecules. As a result, a mechanical bond was used instead.

4.2.2.3 Mechanical bonding of specimens

When casting the liquid silicone, a porous clamp fixture laser cut from Masonite [4] was placed above the liquid silicone. The liquid silicone partially penetrated the Masonite due to capillary action, and remained well bonded to the Masonite once cured. This joint was highly resistant to shear and compressive stresses, but the top layer of Masonite often delaminated when exposed to significant tensile forces.

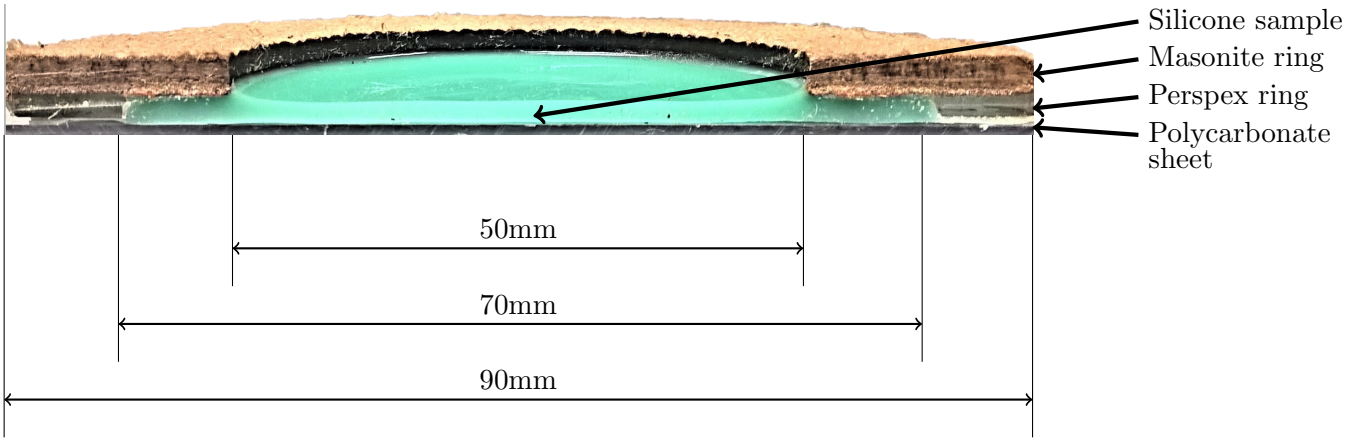

Figure 4.3 Cross section of silicone cast in clamp mechanism

[4]Unlike most forms of wood fibre board, Masonite does not make use of adhesives when being manufactured, relying instead on the lignin contained in the wood fibres. This makes it less likely to interfere with the delicate cure process of platinum cure silicone

Figure 4.3 shows a cross section cut out of a typical silicone membrane bonded to a Masonite ring. Note the meniscus at the edges, slightly increasing the edge thickness of the membrane. This localised increase in thickness was considered to be insignificant for the purposes of this investigation, and the thickness of the flat central portion (approx 5mm from walls and inwards) was taken to be the membrane thickness.
Figure 4.4 shows a clear (unpigmented 10Duro silicone) membrane bonded to Masonite. Note the significant number of air pockets trapped under the Masonite section, and the lack of air pockets in the central section. As the central section was open to the atmosphere during casting, air bubbles could readily escape. However, bubbles in the resin below the Masonite couldn't surface and escape before the liquid silicone gelled.

Neither the teal silicone of fig. 4.3 nor the clear silicone of fig. 4.4 were tested - these images are of specimens made when still experimenting with the clamp/bonding mechanism, and are shown for illustrative purposes

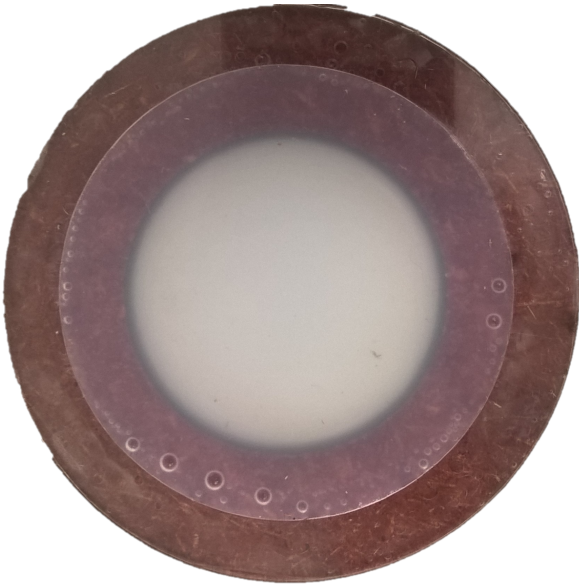

Figure 4.4 Clear silicone membrane bonded to masonite ring

The perspex spacer ring shown in fig. 4.3 was kept with the silicone membrane after it was extracted from the mould. The clamp fixture then compressed the Masonite ring from above, and the silicone and perspex ring from below. Due to the high elastic modulus of perspex relative to silicone, the majority of the clamp force was borne by the perspex ring, allowing for high clamp forces without unduly compressing the edges of the silicone membrane.

The silicone membranes were cast in batches of 25, with the perspex mould and the Masonite clamp rings laser cut. All specimens were cast at a temperature of 30 degrees Celcius for at least 25 hours in order to achieve consistent curing (the silicones used are highly sensitive to the cure temperature).

4.2.3 Speckle pattern generation

Whilst spray paint is typically used for DIC on metal plates, and Bentil *et al* (2016) [34] successfully used spray paint to generate a speckle pattern on silicone, spray paint was not found to be suitable for the materials used here. Spray paint did not bond to the silicone, and cracked at relatively low strains. A variety of membrane speckle patterns were tried, and two were found to be successful:

4.2.3.1 Graphite based speckle pattern:

This speckle pattern was generated by scraping finely divided graphite powder with a slight electrical charge onto the surface of the (white) silicone approximately 20% into the cure time (i.e. at 1 hour for

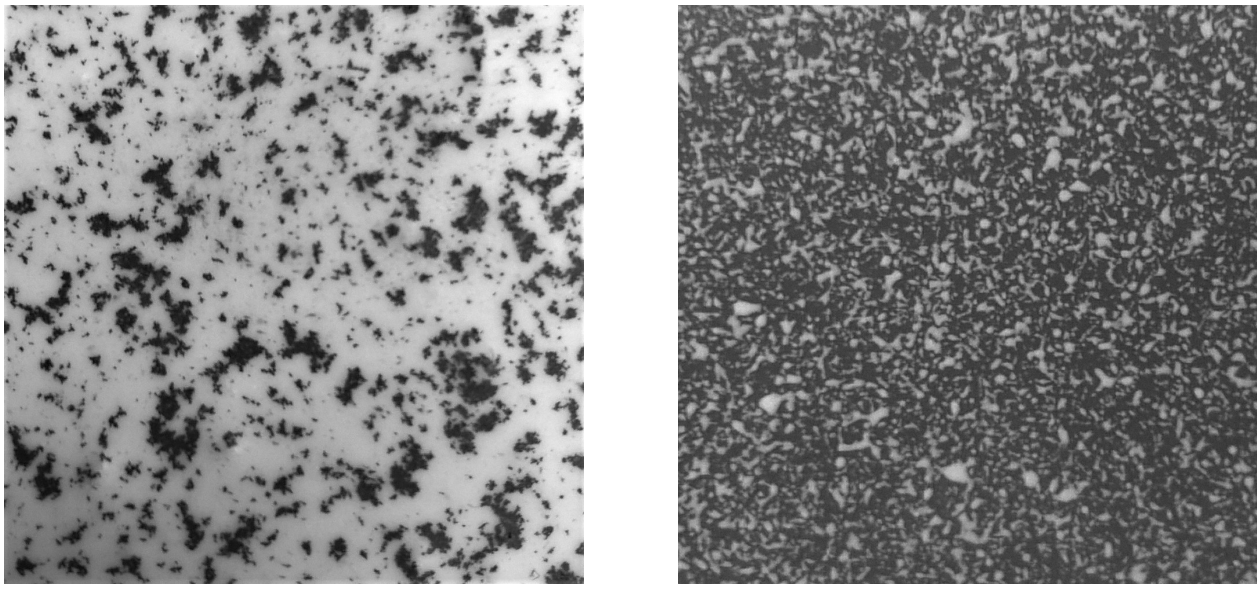

(a) White (10Duro) silicone speckled with graphite flakes

(b) Red (60Duro) silicone speckled with white silicone "paint"

Figure 4.5 Greyscale images of 20x20mm sections of speckled silicone membrane

the Dragon Skin 10 with a 5 hour cure time). Due to the high capillary action of the uncured silicone, the graphite flakes sank slightly below the surface and could not be washed off once the silicone had cured. This method was robust, allowing for DIC detection of strains up to 300%, but resulted in lower accuracy than the silicone based speckle pattern at low strains.
Control of speck size was achieved by changing the geometry and type of graphite used to generate the flakes as well as the angle of the blade used to scape graphite flakes. Smaller, harder raw graphite (such as 0.5mm 2H clutch pencil "lead") resulted in smaller flakes, whilst larger, softer raw graphite (such as 1mm 2B clutch pencil "lead") resulted in large, coarse flakes such as those shown in fig. 4.5a.

4.2.3.2 Silicone based speckle pattern:

This speckle pattern was generated by coating the surface of a silicone membrane with a fine mist of different coloured silicone[5]. The fine mist of silicone was generated by dipping a milk frother into liquid silicone and then turning it on, flinging small silicone droplets away from the frother.

It was important that the silicone speckle pattern was applied to partially cured membrane specimens. Applying the silicone speckle pattern when the membrane was uncured led to mixing of the "paint" and the membrane material, resulting an a fairly uniform grey surface that is unsuitable for DIC. Applying the speckle pattern when the membrane was fully cured led to larger, coarser speckles as the liquid silicone tended to bead together on the surface of the membrane. Not only did this reduce the information density of the pattern, it greatly increased the thickness of the speckles (potentially affecting the mechanical behaviour of the underlying membrane).

[5]The silicone "paint" consisted of Dragon Skin 10 silicone mixed with a large amount of silicone thinner and silicone pigment (approximately 3 times more than the maximum specified by the product data-sheet). The thinner greatly reduced the viscosity (allowing for finer droplets) as well as the stiffness and strength of the silicone "paint". This reduction in strength and stiffness was desirable, as it reduced the impact of the speckles on the membrane's mechanical properties

Speckle size was controlled by changing the viscosity of the "paint" by adding additional silicone

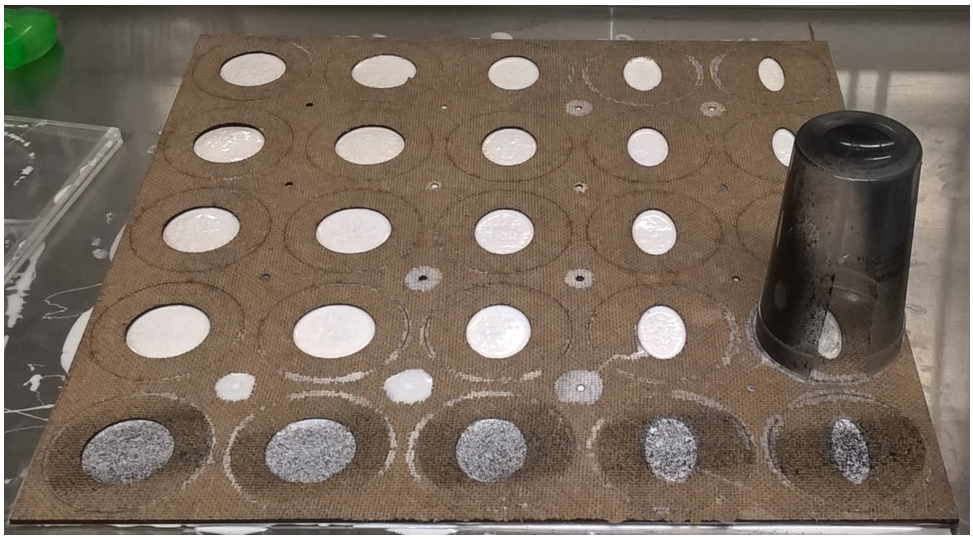

(a) Black silicone speckles being applied to white silicone membrane samples

(b) Milk frother used to apply silicone speckle pattern

Figure 4.6 Silicone speckle pattern being applied

thinner, as well as by changing the application technique. When the frother first started spinning after being dipped in liquid silicone, the resulting specs were large and coarse. As the amount of silicone on the frother decreased, so did the resulting speck size. This allowed for one to control the speck size by controlling how long the frother was on for prior to being placed above the surface of interest. Note that the height of the frother above the sample is not expected to affect the speck size, but will affect the distribution pattern (the specks will likely follow a Cauchy distribution). As a result, the frother was always kept at least 10 cm above the surface when applying speckles. Figure 4.6 shows the speckles being applied to a sheet of samples, and an image of the frother used to apply the speckles. The upside down cup to the right of fig. 4.6a was used to shield the rest of the samples from stray spatter when applying silicone speckles.

Chapter 5

Experimental method

Contents

5.1 High strain rate bulge testing

Using the pneumatic high strain rate bulge tester detailed in chapter 3, the materials detailed in chapter 4 were tested at a variety of piston masses and reservoir pressures. Due to the large range of possible test conditions available, it was not feasible to conduct multiple tests for every combination of variables (membrane material, membrane shape, driving pressure, piston mass, vents). Instead, 5 nominally identical tests were conducted in order to obtain an indication of repeatability, and a series of unrepeated tests were conducted over a wide range of driving pressures, membrane shapes and piston masses.

The pressure and displacement data was synchronised through the use of a 4.5V step pulse which triggered the high speed cameras and the oscilloscope when the firing lever was pressed. The purpose of this voltage pulse was not to set a zero point for the test, but merely to synchronise the pressure and displacement data. The zero point was defined as the time when the pressure adjacent the membrane reached $2kPa$.

5.1.1 Testing matrix

Table 5.1 *List of tests conducted on Mold Max 60, textile reinforced silicone, and Dragon Skin 10 at intermediate driving pressures with a 600g piston and open vents*

Ellipse geometry (mm)	**Mold Max 60** Driving pressure (kPa)						**Textile reinforced silicone** Driving pressure (kPa)					**Dragon Skin 10** Driving Pressure		
	150	170	200	230	250	300	200	250	300	350	400	150	200	250
50 × 50	1	1	1	0	5	1	1*	1,1*	1,1*	1*	1*	3	0	3
50 × 40	1	0	1	1	1	1	0	1	1	0	0	0	0	0
50 × 30	1	1	1	1	0	1	0	1	1	0	0	0	0	0
50 × 20	1	0	1	1	1	1	0	1	1	0	0	0	3	0

* indicates a 3mm thick membrane

Table 5.2 *List of tests conducted on circular Mold Max 60 and Dragon Skin 10 membranes at high and low driving pressures*

Piston mass (g)	**Vents**	**Mold Max 60** Driving pressure (kPa)					**Dragon Skin 10** Driving pressure		
		40	60	100	200	630	20	40	700
1600	Closed	1	1	1	1	0	1	1	0
400	Open	0	0	0	0	1	0	0	1

5.1.1.1 Closed ended cylinder

The membrane was replaced with a nominally rigid sheet (4mm of perspex), and the device was fired at a variety of driving pressures. This allowed one to compare the consistency and predictability of the pressure profile independently of the effects of the membrane. The device was fired 5 times each at 150,200,250 and 300 kpa with a 600g piston.

5.1.1.2 Mold Max 60 silicone

29 membranes of 2mm thick Mold Max 60 silicone were tested in total.

1. Five circular membranes under identical conditions (600g piston, 250kpa firing pressure) in order to quantify the consistency of the device's behaviour

2. Five membranes of each membrane geometry (minor diameter 20, 30, 40, 50) were tested at driving pressures of (150, 200, 250 and 300 kpa), and then one membrane was tested at a driving pressure 20kpa lower than burst pressure. These tests focussed on covering a wide range of membrane geometry and driving pressures.

3. Four circular membranes were tested at 40, 60, 100 and 200 kpa driving pressure with a 1.6kg piston and closed vents. The purpose of these tests was to obtain an indication of the minimum possible strain rate achievable by the device.

4. One circular membrane was tested with a 400g piston and a driving pressure of 630 kpa, in order to obtain an indication of the approximate maximum strain rate obtainable. Firing at significantly higher pressures would likely have resulted in damage to the piston, unless a membrane with a higher burst pressure was tested.

5.1.1.3 Dragon Skin 10 silicone

10 Duro silicone samples were used extensively when testing various bulge tester subsystems, but due to the low stiffness of the 10 Duro silicone membranes, the membrane pressure was barely readable on the pressure sensor used. As a result, only 12 10Duro silicone membranes were tested fully:

1. With a 600g piston and open vents:

   Three circular membranes at 150kPa

   Three circular membranes at 250kPa

   Three 50x20mm elliptical membranes at 200kPa

2. With a 1600g piston and closed vents:

   One circular membrane at 20kPa

   One circular membrane at 40kPa

3. With a 400g piston and open vents:

   One circular membrane at 700kPa

5.1.1.4 Textile reinforced silicone

Thirteen textile reinforced samples with were tested in total, all with a 600g piston and open vents:

1. Two of each membrane geometry were tested at 250 and 300kpa driving pressure (eight in total), in order to examine the effects of changing membrane geometry on an anisotropic material. These membranes were all 2mm thick with 2 layers of textile reinforcement

2. Five circular membranes were tested at driving pressures of 200, 250, 300, 350 and 400 kPa in order to examine the effects of increasing driving pressure. These membranes were all 3mm thick, with 2 layers of textile reinforcement.

When testing the 2mm thick textile reinforced membranes, it was observed that bubbles in the silicone matrix (as shown in fig. 4.1) occasionally burst significantly earlier than the bulk membrane. As a result, the next set of membranes were 3mm thick, in order to mitigate this localised bursting. No localised bursting was observed in the 3mm thick textile reinforced membranes.

5.1.2 Pressure measurement

The membrane pressure was measured with a high speed piezoelectric pressure transducer (Dytran Instruments 2300V3). This sensor had an accuracy of $\pm 1\%$, an equivalent electrical noise (resolution) of 48.3 Pa, and an operating range of 0-3.447Mpa (0-5V electrical output). In practise the measured noise was significantly greater than 50 Pa, with an equivalent magnitude of $1.6kPa$. When passed through a Fourier transform, this noise occurred predominantly at $18kHz$. The additional noise is likely caused by electromagnetic interference, as well as noise from the amplifier. Shielded coaxial cables supplied with the pressure transducer were used in order to minimise electrical interference.

The data from this sensor was read into a 12 bit Picoscope3424 from Picotech with an accuracy of $\pm 1\%$. Pressure data was recorded for 500 ms from when the firing lever was pressed in order to ensure that all relevant data was captured regardless of driving pressure or membrane stiffness. This resulted in a sample interval of $6.4\mu s$ - well above the $1\mu s$ rise time of the pressure sensor, but well below the $125\mu s$ sample interval of the high speed cameras (8000 fps).

A sample interval $6.40\mu s$ is equivalent to a sampling frequency of $156kHz$, and can accurately capture signals with a frequency of $78.1kHz$. Frequencies this high are not expected from the data, and a Fourier transform of a test sampled at $625kHz$ confirmed this. No significant frequencies above $1kHz$ were detected, indicating that a sample frequency of $156.25kHz$ is sufficient to capture the pressure rise and decay.

Due to geometry constraints, this pressure sensor was located approximately $20mm$ behind the membrane. As a result, pressure due to the piston was measured approximately $50\mu s$ before it reached the membrane, and pressure due to the membrane was measured approximately $50\mu s$ after it occurred. Placing the pressure sensor closer to the membrane was not found to be feasible, and similar tests in the literature have placed the pressure sensor $12.7mm$ from the membrane [34].

5.1.3 Membrane displacement measurement

High speed 3D DIC was used to measure the deformation of the membrane. All tests were filmed using the camera system from the blast pendulum built by Curry (2017) [37]. The cameras used were two IDT vision NR4 S3 high speed cameras synchronised via a synchronising cable between the camera control boxes and triggered by the rising edge of the bulge tester's trigger circuit (which simultaneously triggered the pressure reading). Before testing, each membrane was lightly dusted with talc powder, which reduced reflections and glare from the lighting.

5.1.3.1 Camera setup

Each camera was set to an aperture of f 22 in order to maximise the depth of field, and the region of interest was set to 352x360 pixels. This resulted in a spatial resolution of $0.185mm$ per pixel, and allowed for a maximum frame rate of just over 8000 fps (due to camera limitations). The cameras were set to a focal distance of $440mm$ and an included angle of $31.0°$. This resulted in a nominal depth of field (DOF) of $135mm$ ($57mm$ in front of focal plane and $78mm$ behind focal plane).The specimen was placed $450mm$ from the cameras, increasing the useable focal depth by $10mm$.

Achieving sufficient lighting was challenging: early tests were filmed at 5000 fps, and later tests were filmed at 8000 fps (once additional lighting had been acquired). Using an aperture of f 16 would theoretically allow for a DOF of $95mm$ and shorter shutter times or less lighting, but this was found to result in reduced correlation accuracy and an unacceptably low DOF.

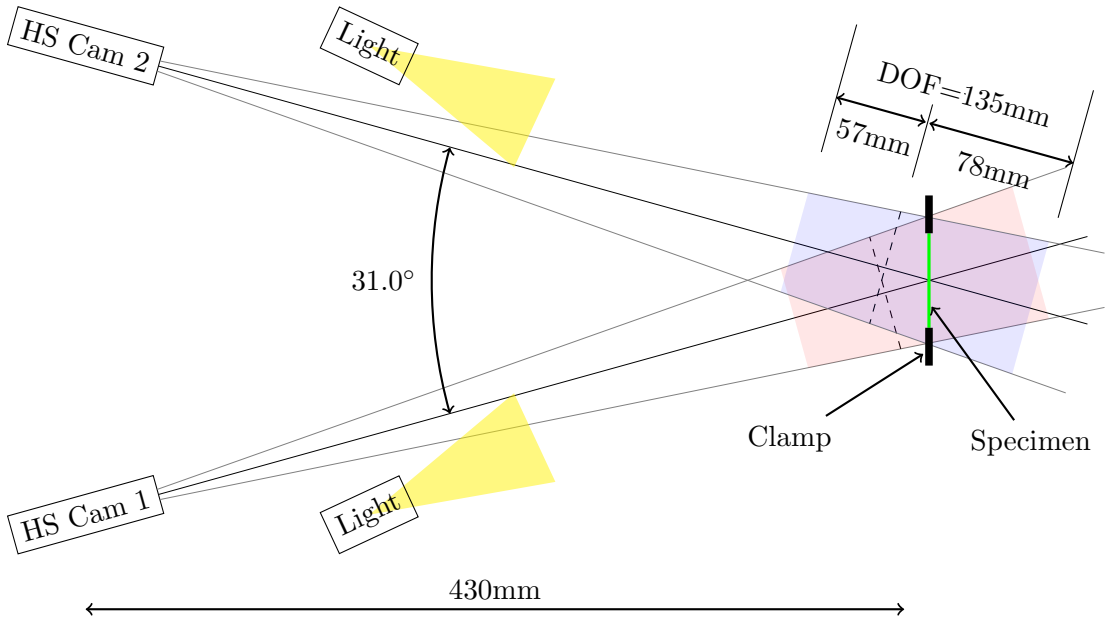

Figure 5.1 1:4 scale diagram of DIC camera setup viewed from above. Camera focal plane shown with dotted lines, and camera focal area shown in pale blue and red. Unstretched specimen shown in green.

Figure 5.1 shows the camera setup used for DIC measurements. Note that only the region encapsulated within the focal area of camera 1 (shaded red) and camera 2 (shaded blue) can be measured before the images lose focus (or the specimen leaves the imaging region). The DIC software is unable to correlate between cameras reliably once focus is lost. This implies that the entire focal region behind the specimen is wasted, however:

1. Objects at the extremes of the focal depth have up to one pixel of blur, whilst objects at the focal plane have (nominally) zero blur.

2. All displacement and strain calculations are done relative to the unstretched membrane. This makes it important that images of the unstretched membrane have high fidelity, reducing error propagation.

3. As a compromise, the unstretched membrane started approximately $10mm$ behind the focal plane of each camera, bulged into perfect focus and then continued to bulge.

Each camera's focal region of interest was vertically truncated in order to allow for greater frame-rates, and was horizontally truncated in order to decrease image size[1]. This was not a problem for this set of experiments, as the membranes burst prior to leaving the focal area of the cameras [2].

[1]Unlike most high speed cameras, the frame-rate of the high-speed cameras used for this project was affected purely by the resolution of the y axis, and not the x axis. The images were truncated in the x axis in order to reduce the size of the images; even with truncated images, it took over 20 minutes to store the images from each experiment.

[2]Note that motion blur can still occur, even if the images are in perfect focus

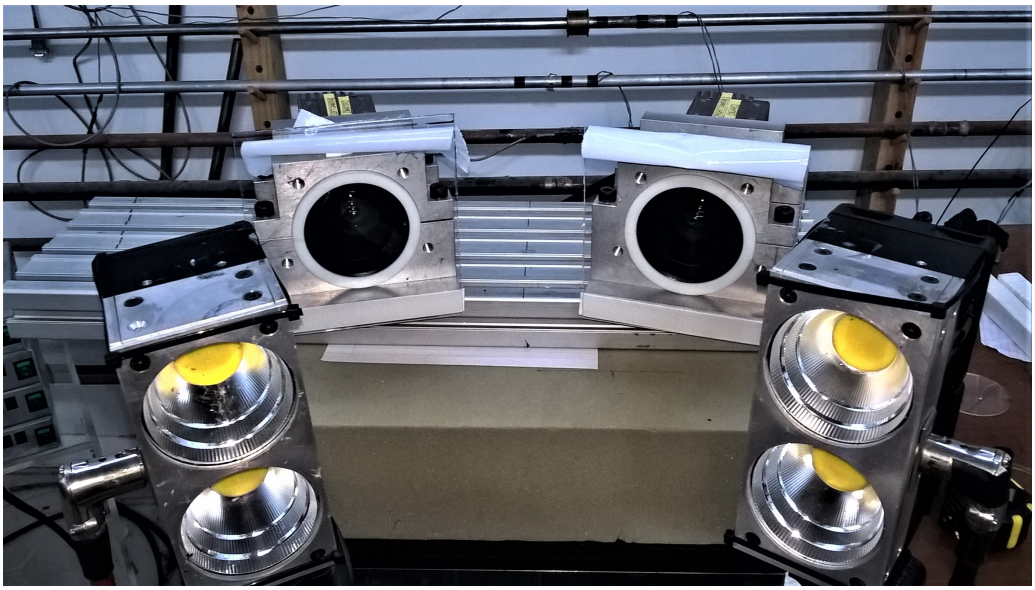

Figure 5.2 Cameras and high power LED lights shown in fig. 5.1. Image taken from perspective of specimen. White plastic flaps above the cameras are covers for the polycarbonate camera shields, preventing scratches when not in use. Camera rail, cameras and lights taken from blast pendulum used by Curry (2017) [37]

In order to protect the camera lenses from high speed membrane fragments, 2mm thick polycarbonate[3] shields were used. These shields caused the DIC to measure a slight rigid body displacement if the cameras were calibrated before the shields were placed[4]. In order to eliminate this effect[5], the cameras were calibrated once the shields were already in place. When not in use the shields were covered in order to prevent scratches, and if any scratches were observed the shields were replaced.

5.1.3.2 Calibrating high speed cameras

Prior to each set of tests, 200 pairs of calibration images were taken (20 seconds at 10 fps). These were stereoscopic images of a calibration target with well known dimensions[6] supplied by Dantec Dynamics. Of these 200 images, 7 pairs were chosen for the calibration process. These seven pairs were chosen to cover the entire sensor range, and were generally chosen to have the calibration target at each of the 4 corners, in the centre and in the centre but tilted in x and y. Whilst only a small portion of the sensor was used for the test, the calibration images covered the entire sensor. This was important in order to allow the software to accurately calculate the various intrinsic properties of the lenses.

[3]Perspex shields would be more scratch resistant than PC, but significantly less impact resistant

[4]The same effect was found by Tonge (2014) [1]

[5]As this project is interested in relative displacements and strains, this effect would theoretically not be a problem. However, it was felt that correcting for this effect would be more experimentally sound. All calibration images were taken with the shields in place.

[6]Calibration target *GL 06 WMB 9x9* was used, consisting of a 9x9 grid of 6mm squares with dimensions accurate to the micron level

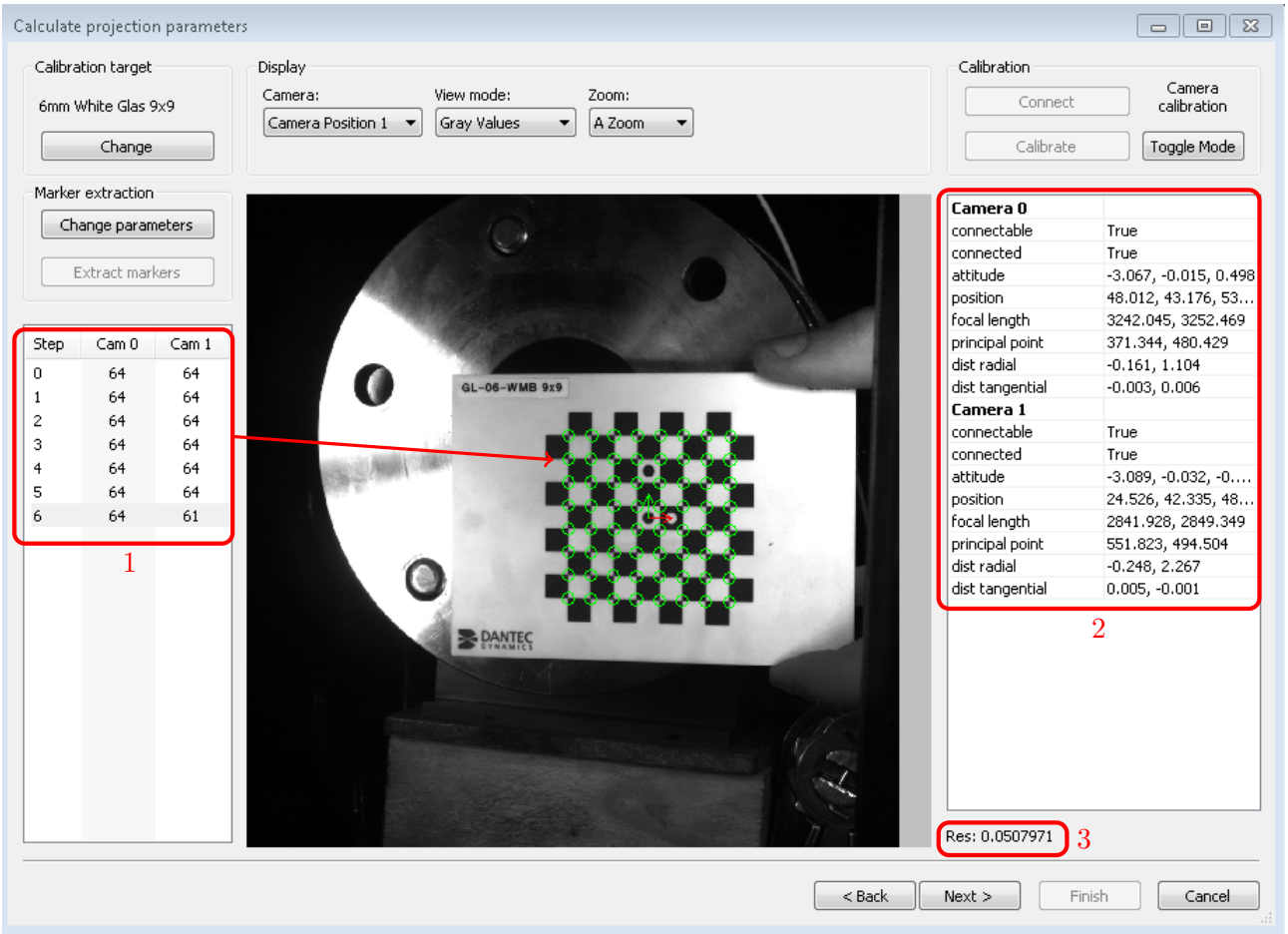

Figure 5.3 Example of a calibration image in the Istra software.

Figure 5.3 shows an example of a calibration image in the DIC software. The left pane (box 1) shows the number of points/corners detected on each image (64 is the maximum, and 50 is a recommended minimum), and the right pane (box 2) shows the calculated intrinsic and extrinsic parameters for each camera. The bottom right of the image (box 3) shows the calibration residuum - this is directly related to correlation accuracy, and should be kept as low as possible. In practise, this number ranged from 0.02-0.06 pixels.

5.1.4 Processing of data

Both the high speed cameras and the pressure transducer started recording as soon as the trigger was pressed, but in practise the pressure rise only occurred 150-200 ms after the trigger was pressed. The start of the pressure rise was identified on the Osciloscope, and then DIC images were taken from at least 20ms before, starting on a 25ms increment. Figure 5.4 shows an example of a pressure trace where the pressure rise occured at approximately 177ms - as a result, DIC images from 150ms until bursting were analysed. This ensured that a reasonable number of nominally stationary images were included in the DIC analysis, allowing one to identify if there was any movement of the membrane prior to the arrival of the pressure wave. DIC images until bursting were analysed, but in practise correlation was often lost a few frames prior to bursting due to a combination of heavy distortion and motion blur[a]. The entire range of pressure readings were processed, as the additional processing time was trivial. These pressure results were later truncated, and the temporal region of interest extracted.

[a]Whilst the images were in focus, motion blur still occurred at high speeds due to shutter time limitations

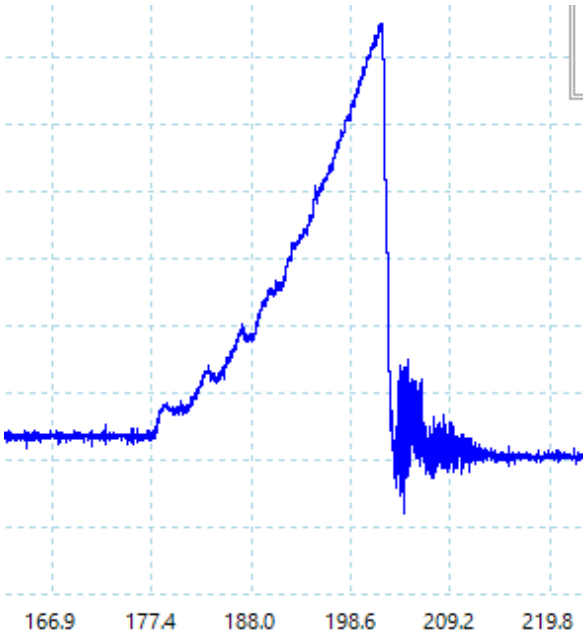

Figure 5.4 Example of a pressure trace for a bulge test (prior to noise filtering). This figure is shown without units or a scale, as the purpose is to convey qualitative rather than quantitative information

5.1.4.1 DIC Data

The Dantec Dynamics Istra 4D DIC software package was used to process the high speed stereoscopic images. Each test had an associated (not neccessarily unique) series of calibration images which was used to generate a calibration file specifying the parameters of each camera. This calibration file (along with the correlation images) was used to generate a displacement field for each frame of the test. A gauge point was then placed in the centre of the membrane (at the apex), and the Lagrangian strain in x and y as well as the z displacement for each frame were extracted in csv format.

Defining of the co-ordinate system: For circular membranes of isotropic materials, the default co-ordinate system defined by the calibration images was used. For elliptical membranes, the x axis was defined as parallel to the minor axis of the elipse, with y axis parallel to the major axis. For circular, anisotropic membranes, the x and y axis were defined such that the principal strains coincided with the x and y axis (i.e. there was no shear at the apex). This allowed one to detect the direction of the stiff fibres, as the strain was significantly lower in this direction. In all cases, the z axis was normal to the unloaded (flat) membrane.

5.1.4.2 Pressure data

The pressure data contained electrical noise equivalent to $1.6kPa$, occurring predominantly at $18kHz$. A Savitsky-Golay filter [61] algorithm developed by Savitzky and Golay (1964) [62] was used to smooth the electrical noise of the signal. This filter was chosen as it was easy to modify, numerically efficient and entirely in the time domain (no Fourier transforms were required). A smoothing window of width 41 (equivalent to 0.26 ms) and order 3 was used [a]. This largely removed the Gaussian noise without significantly affecting the pressure reading, as the period of the lowest observable oscillation was 5ms - significantly greater than the width of the smoothing window. Additionally, the use of a 3rd order smoothing polynomial allowed for the capture of higher order (and frequency) effects[61].
The pressure data had a sample time of 6.4 μs, leading to approximately 20 or 31 pressure readings per frame (depending on whether filming was at 5000 fps or 8000 fps).

[a] i.e. each data-point was replaced by the point suggested by the 3rd order polynomial best fit curve through 20 data-points to either side of the point of interest

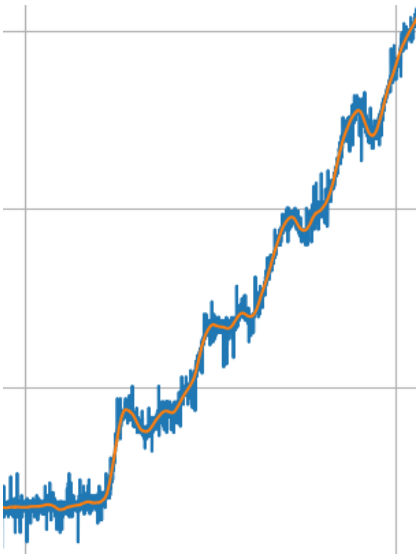

Figure 5.5 Pressure data before (blue) and after (orange) smoothing. Note that oscillations are still captured. This figure is shown without units or a scale, as the purpose is to convey qualitative rather than quantitative information

5.1.4.3 Post-processing of pressure and displacement/strain data

Once the displacement and strain data of the DIC and the pressure data for each test was acquired in csv format, a custom python script was used to combine, process and plot the data in .pgf format (allowing for direct insertion into LaTeX).The DIC generated displacement and strain data had any missing points generated through polynomial interpolation, and the pressure data was truncated to only the temporal region of interest (i.e. the temporal region covered by the DIC results). The pressure data was downsampled to match the sample rate of the DIC data using polynomial interpolation, and the results written to a csv file. In addition to the pressure, strain and displacement at the apex, pressure rate, strain rate and velocity were calculated and written to the csv file as well.

The strain data was defined as having a "dynamic" section (where the behaviour was dominated by inertial effects), and an "equilibrium" section (where the behaviour was dominated by pressure:stress interactions). A least squares straight line was fitted through the "equilibrium" section, and the goodness of fit and implied strain rate were calculated and displayed.

In practise, storing the processed results in a csv file was not necessary, as post-processing/collation time per test was on the order of seconds.

Numerical derivation is an inherently noisy process, and tends to amplify any noise in the data. The strain data is already the numerical spatial derivative of the displacement measured by the DIC, making the time derivative of the strain particularly noisy.

5.2 Uniaxial tensile tests

In order to develop a more comprehensive approach to material modelling, uniaxial tensile tests were done in conjunction with the bulge tests. Simple uniaxial tensile tests were conducted on each material tested (10 Duro Dragon Skin silicone, 60 Duro Mold Max silicone, textile reinforced 10 Duro Dragon Skin silicone and on the silicone "paint" used to make speckle patterns).

Tensile specimen dies were laser cut in the shape specified by *ASTM D412-16: Standard Test Methods for Vulcanized Rubber and Thermoplastic Elastomers - Tension* [63], and each silicone material was cast in the dies.

5.2.1 Testing matrix

Table 5.3 *Uniaxial tensile tests conducted*

Strain rate (s^{-1})	**Dragon Skin 10**	**Silicone "paint"**	**Mold Max 60**	**Textile Reinforced Silicone**		
				Warp axis	45°	Weft axis
2.2×10^{-1}	✓	✓	✓	✓	✓	✓
2.2×10^{-2}	✓		✓			
2.2×10^{-3}			✓			

The 10 Duro and 60 Duro silicone samples were tested at a variety of strain rates (2.2×10^{-1}, 2.2×10^{-2}, and 2.2×10^{-3} s^{-1}) in order to determine both the effect of both strain and strain rate. Additionally, the presence of the Mullins effect[7] was tested for by straining a single tensile sample multiple times under identical conditions and recording the change in mechanical behaviour with repeated tests.

The textile reinforced silicone samples were tested at 0, 45 and 90° to the weft fibre axis, allowing for an approximation of the degree of anisotropy as well as the non-linear behaviour of the embedded fibres.

The silicone "paint" used to generate speckle patterns was tested in order to determine the ultimate tensile strain as well as the approximate stiffness, giving an indication of the mechanical impact of the "paint" on each membrane.

Each uniaxial tensile test specimen was measured with a Vernier caliper prior to testing, as the laser cut tensile specimen moulds had tolerances of approximately 0.2mm. Each pure silicone tensile

[7]This project does not plan on quantifying the Mullins effect on these polymers, but it is important to test the extent to which it occurs. If it occurs to a significant degree but is ignored, spurious conclusions may be drawn. The Mullins effect occurs in some polymers when stretched past a certain strain. The initial (elastic) stretch can be significantly stiffer than subsequent ones, causing potentially unreliable results in not taken into account

test was then modelled with a 4 term Ogden material, and a least squares downhill optimisation approach was used to determine the 8 material parameters. Due to instabilities in the algorithm, conditional damping was introduced in the optimisation process. This reduced the convergence rate (and instability) when the error was large, but had no effect when the error was small and the solution was close to convergence.

In practice it was found that the use of more than 2 Ogden terms led to repetition of identical parameters - increasing the computational complexity of the material model with no increase in accuracy. The goodness of fit was not described using R^2, as R^2 values are suspect at best when describing goodness of fit for certain types of non-linear best fit curves[64]. Unlike polynomial least squares fitting, the co-efficients in an Ogden fit are not orthogonal to the residual, making R^2 values an invalid descriptor for correlation. The standard error was used instead, as it is a more reliable indicator of goodness of fit. [8]

[8] https://stats.stackexchange.com/questions/92065/why-is-polynomial-regression-considered-a-special-case-of-multiple-linear-regres/92087#92087 has an excellent explanation of why polynomial best fit curves are a special case of a linear best fit curve

Chapter 6

Numerical Modelling

Contents

Bulge tests A selection of the bulge experiments were simulated using the commercial explicit finite element code LS-DYNA. The aim of these simulations was to augment the understanding gained by the experimental data, and to validate the feasibility of the inverse iteration parameter extraction method for the experimental method conducted in this project.

Uniaxial tensile tests Due to their relative simplicity, the uniaxial tensile tests were modelled analytically. A custom python script was then written to use an inverse iteration method to extract material parameters from the uniaxial tensile test experimental data. An advantage of this method was that it allowed for custom material models to be used - adding custom material models to LS-DYNA is significantly outside the scope of this dissertation.

6.1 Material model used

All three materials tested (Dragon Skin 10 Silicone, Mold Max 60 silicone and textile reinforced silicone) were modelled using a modified version of the anisotropic, visco-elastic soft tissue model developed by Weiss *et al* (1996,1998) [4, 21] (shown in sections 2.3.2.1 and 2.3.2.2). This model was modified slightly in order to capture the behaviour of a textile reinforced silicone elastomer. This model consisted of the following:

1. An isotropic, hyper-elastic, incompressible term representing the elastic deformation of the silicone matrix. This term was described with the Ogden model, unlike in the Weiss model, where a compressible Mooney-Rivlin term was used. An Ogden model was necessary in order to capture the high strain hardening co-efficients exhibited by silicone.
2. An isotropic, rate dependant, incompressible viscous term representing the viscous damping effect of the silicone matrix. This term modelled a Maxwell fluid represented by a Prony series, and took the same form as the viscous term of the Weiss model. Note that the Weiss model included the effects of the fibre matrix in the viscous term, but this model includes the effects of the elastomer matrix alone.
3. A transverse isotropic fibre term describing the effect of the textile fibres based on the model of Weiss *et al* (1996) [4]. In the warp direction this term was identical to the Weiss fibre model, but in the weft direction this term was a simple linear hyper-elastic model. This term had zero stiffness in the z direction (perpendicular to the warp and weft axis), and each fibre had no compressive stiffness.

For the unreinforced silicone the fibre stress term was set to zero (as there were no fibres). Note that if the fibre stress term is dropped, this model is identical to the *LS Dyna* Ogden Rubber model (*MAT_077_O*).When analysing the uniaxial tensile test data the viscous term was ignored as the uniaxial tensile tests covered a small number of strain rates - this meant that it was not feasible to extract viscous properties from the uniaxial tensile test data.

Weiss Model

$$\Psi_{Weiss} = C_1(I_1 - 3) + C_2(I_2 - 3) + F(\lambda) + \frac{1}{2}K[ln(J)]^2 \tag{6.1}$$

$$\frac{\partial F}{\partial \lambda} = \begin{bmatrix} 0 & \lambda < 1 \\ \frac{C_3}{\lambda}[e^{C_4(\lambda-1)} - 1] & \lambda < \lambda^* \\ \frac{1}{\lambda}(C_5\lambda + C_6) & \lambda \geq \lambda^* \end{bmatrix}$$

$$\boldsymbol{S}(\boldsymbol{C}, t) = \boldsymbol{S}(\boldsymbol{C}) + \int_0^t 2G(t-s)\frac{\partial \Psi}{\partial \boldsymbol{C}(s)}ds \qquad G(t) = \sum_{i=1}^{N} S_i e^{\frac{t}{T_i}} \tag{6.2}$$

λ^* represents the stretch at which a collagen fibre is considered to have straightened (and transitioned to linear behaviour)

Modified Weiss model

$$\boldsymbol{T}(\boldsymbol{B}(t)) = V \times \overbrace{\left[\underbrace{\boldsymbol{T}_e(\boldsymbol{B}(t))}_{\text{Elastomeric}} + \underbrace{\int_0^t 2G(t-s)\boldsymbol{B}(t) \cdot \frac{\partial \Psi}{\boldsymbol{\partial B}(s)}ds}_{\text{Viscous term}}\right]}^{MAT\_077\_O \text{ in } LS\ Dyna} + \underbrace{(1-V) \times \left[\boldsymbol{B^*} \cdot \frac{\partial F}{\partial \boldsymbol{B^*}}\right]}_{\text{Fibre stress}} \tag{6.3a}$$

V is the volume fraction of silicone matrix:fibres

$$\boldsymbol{T}_e(\boldsymbol{B}(t)) = 2\boldsymbol{B}(t) \cdot \frac{\partial \Psi}{\boldsymbol{\partial B}(s)} = -P\boldsymbol{I} + \sum_{p=1}^{N} \mu_p \sum_{i=1}^{3} \lambda_i^{\alpha_p} \boldsymbol{f}_i \otimes \boldsymbol{f}_i \tag{6.3b}$$

Where λ_i are the principal stretches (eigen values) of $\boldsymbol{F}$, and $\boldsymbol{f}_i$ are the principal directions.

$$G(t) = \sum_{i=1}^{n} S_i e^{\frac{t}{T_i}} \tag{6.3c}$$

Where S_i are the normalised shear moduli, and T_i are the respective decay times in the Prony series

$$\frac{\partial F}{\partial B^*_{11}} = \begin{Bmatrix} 0 & \lambda^*_1 < 1 \\ \frac{C_1}{\lambda^*_1}(\lambda^*_1 - 1) & \lambda^*_1 \geq 1 \end{Bmatrix} \quad \frac{\partial F}{\partial B^*_{22}} = \begin{Bmatrix} 0 & \lambda^*_2 < 1 \\ \frac{C_2}{\lambda^*_2}\left[e^{C_3(\lambda^*_2 - 1)} - 1\right] & \lambda^*_2 < \lambda_{crit} \\ C_4 + \frac{C_5}{\lambda^*_2} & \lambda^*_2 \geq \lambda_{crit} \end{Bmatrix} \quad \frac{\partial F}{\partial B^*_{33}} = 0 \tag{6.3d}$$

C_1, C_2, C_3 and C_4 are chosen, and C_5 is set to ensure continuity of the curve. λ_{crit} is the critical stretch ratio at which the fibre is assumed to have fully straightened. $\boldsymbol{B^*}$ represents $\boldsymbol{B}$ decomposed into the principal fibre directions (weft, warp, normal to textile), and λ^* represents the stretches in the principal fibre directions. The fibres are assumed to have negligible compressive stiffness. Note that the fibre model is identical to the Weiss fibre model in the warp direction, and equivalent to an uncrimped fibre in the weft direction[1].

6.2 Uniaxial tensile tests

A custom python script was written to read in the force:strain data taken from the uniaxial tensile test rig load cell and contact extensometer respectively, and convert the engineering strain into stretch ratio. The uniaxial tensile tests were modelled as 1D tests of a homogenous, incompressible[2] material. Given that the uniaxial tensile tests were run for a small number of strain rates[3], the viscous terms of the modified Weiss model were ignored. A least squares downhill optimisation algorithm was written to select material parameters which minimised the difference between the experimental and the numerical results. The non-linear optimisation method used was closely based on methods used in the non-linear FEA course taken by the author. Further details can be found in chapter 5 of *Nonlinear Finite Element Methods* by P. Wriggers (2008) [65].

6.2.1 Numerical model of test

Taking λ_1 to be the stretch ratio measured by the contact extensometer, and a_0 to be the initial cross sectional area of the uniaxial tensile specimen, the instantaneous cross sectional area was given by:

$$\lambda_2 = \lambda_3 = \lambda_1^{0.5} \quad \because J = 1 = \lambda_1\lambda_2\lambda_3 \tag{6.4}$$

$$a = a_0\lambda_2\lambda_3 = \frac{a_0}{\lambda_1} \tag{6.5}$$

Note that eq. (6.5) only holds true if the principal axis of the uniaxial tensile test coincide with the principal fibre directions. This, coupled with the expression for Cauchy Stress given in eq. (6.3a), allowed for the experimental force:stretch data from the uniaxial tensile tests to be compared to the

[1] I.E. a fibre with zero crimp angle, which straightens at a stretch of 1

[2] Given the presence of bubbles, it is not entirely accurate to model the textile reinforced silicone as incompressible. Modelling it as incompressible gave a close correlation with experimental results however. If the material was to be modelled as incompressible, the lateral strains would have to be measured.

[3] Some materials were only tested at two strain rates, and others at three strain rates

force:stretch curve predicted by the modified Weiss model:

$$F^{num}(\lambda_1) = \frac{a_0}{\lambda_1}\left[(1-V)\lambda_1^2\frac{\partial F}{\partial \boldsymbol{B}} + V\sum_{p=1}^{N}\mu_p(\lambda_1^{\alpha_p} - \lambda_1^{-\frac{\alpha_p}{2}})\right] \tag{6.6}$$

λ_1 will be λ_1^*, λ_2^*, or λ_3^* if the fibre is being tested in the weft, warp or normal direction respectively.

6.2.2 Parameter extraction

For a tensile test with m data points, let the squared residual be represented by $\boldsymbol{G}$, and the various material parameters by the vector $\boldsymbol{P}$. The numerical force ($\boldsymbol{F}^{num}$) is a function of the measured stretch ($\boldsymbol{\lambda}$) and $\boldsymbol{P}$. The residual is calculated as:

$$\boldsymbol{G} = (\boldsymbol{F}^{num} - \boldsymbol{F}^{exp}) \odot (\boldsymbol{F}^{num} - \boldsymbol{F}^{exp}) = \boldsymbol{G}(\boldsymbol{\lambda}, \boldsymbol{P}, \boldsymbol{F}^{exp}) \tag{6.7}$$

Note that $\odot$ represents the Hadamard product of two tensors (element-wise multiplication)[4]. $\boldsymbol{G}(\boldsymbol{P})$ is linearised at point $\boldsymbol{P} = \boldsymbol{P}_n$ in the direction $\Delta\boldsymbol{P}$ as:

$$\boldsymbol{G}(\boldsymbol{P}) \approx \boldsymbol{G}(\boldsymbol{P}_n) + \boldsymbol{D}[G(\boldsymbol{P})] \cdot \Delta\boldsymbol{P} \tag{6.8}$$

Where the tangent matrix can be calculated by:

$$D[\boldsymbol{G}(\boldsymbol{P})] \cdot \Delta\boldsymbol{P} = \frac{\partial}{\partial\epsilon}\left(\boldsymbol{G}(\boldsymbol{P}_n + \epsilon\Delta\boldsymbol{P})\right)_{\Delta\boldsymbol{P}=\boldsymbol{0}} \tag{6.9}$$

Given that $\boldsymbol{G}(\boldsymbol{P})$ should approach zero as the numerical model more closely matches the experimental data, $\boldsymbol{G}(\boldsymbol{P})$ is set to zero in eq. (6.8), resulting in:

$$\Delta\boldsymbol{P} = -[\boldsymbol{G}'(\boldsymbol{P}_n)]^{-1}\boldsymbol{G}(\boldsymbol{P}_n) \tag{6.10}$$

$$\boldsymbol{P}_{n+1} = \boldsymbol{P}_{n+} + \Delta\boldsymbol{P} \tag{6.11}$$

$\boldsymbol{P}_0$ was taken to be the initial material parameters guessed by the user, and eq. (6.11) was iterated over until one of the termination criteria was reached (number of iterations, converged $\boldsymbol{P}$, or increasing $\boldsymbol{G}$).

6.2.2.1 Stability

This solution method was particularly unstable:

1. Equation (6.9) was calculated numerically rather than analytically, leading to some instabilities in the algorithm - particularly where the tangent matrix represented steep gradients. Additionally, the Ogden model is sensitive to changes in α when modelling high stretch ratios.
2. Given that a best fit curve is being fitted to real world data, the error is likely to converge to a non-zero value. This is analogous to using Newton's method to find the root of $x^2 + 1$, in that significant instability will occur around the local minima.

As a result, numerical damping was performed at each step. This slowed convergence, but ensured that the algorithm was stable. Where entries in the tangent matrix would result in a Jacobian of close to zero, they were ignored for that step of the iteration (allowing for the tangent matrix to be inverted).

[4]Readers familiar with the Matlab programming language may be accustomed to $\boldsymbol{A} \odot \boldsymbol{B}$ being represented as $\boldsymbol{A}.*\boldsymbol{B}$

6.2.2.2 Speed

In order to decrease computation time when extracting material parameters for multiple tests, $\boldsymbol{P}_0$ for each subsequent test was set to the final value of $\boldsymbol{P}$ calculated in the previous test (rather than relying on the user's initial guess).

In spite of the numerical damping slowing convergence, it took approximately 30 seconds to extract material parameters for each uniaxial tensile test. As a result, it was not necessary to increase the efficiency of the algorithm used.

Interestingly, minimising the norm of the residual (rather than the residual) resulted in faster solve times. This method required a greater number of convergence steps, but each step was significantly faster. As a result, this method was predominantly used for more stable problems.

6.3 FEA modelling of bulge tests

Simple FEA code was written from scratch in Matlab during the design process in order to confirm design decisions, but this code had limited utility in modelling more complex phenomena. This code ran slowly, and could handle only a small number of material models. As a result, commercial FEA software was used to model the experimental setup, and compared with experimental results.

As the focus of this dissertation is not numerical simulation, the FEA results were used to augment the experimental results. Mesh independence studies, convergence plots and FEA benchmarking were not done. The values for element size and timestep suggested by the FEA software were used and not modified, and custom material models were not written into the FEA software.

The LS Dyna explicit solver (V4.3.12 - 10 July 2017) developed by Livermore Software Technology Corp (LSTC) was used to model a representative experiment using measured pressure data as an input. The displacement data extracted from this FEA simulation was compared to the experimental displacement data. Due to the time and effort involved in designing the dynamic bulge test device, and conducting high rate bulge tests with DIC, only one set of experiments was simulated: circular, 50mm diameter, 2mm thick Mold Max 60 membranes tested with open vents, a 600g piston and 250kPa driving pressure. This simplified modelling, particularly as the membrane was isotropic.

6.3.1 Elements used

Belytschko-Lin-Tsay updated Lagrangian shell elements were used, with 2 through thickness integrations points. Each node has 5 local degrees of freedom, resulting in 6 global degrees of freedom. Bending, shear, warping, and membrane stresses are captured by this element type, but not through thickness stresses (i.e only plane stress behaviour is captured).

This element type captures bending stiffness poorly in comparison to multi-element thick solid FE models. This is not expected to be a significant source of inaccuracy, as the membrane has low thickness:diameter ratio and undergoes large out of plane displacements. Particularly at high strains, hoop stress effects are expected to dominate bending effects. As a result, the model is likely to be more accurate at high strains than at low strains. It would have been possible to use solid elements from a computational time perspective, however fully coupled models (with MMALE) require the use of shell elements.

6.3.2 Geometric representation

The membrane was modelled using quarter symmetry, and an element size of 1mm. This discretization size was suggested by the FEA software used, and was not changed. The membrane was modelled as having uniform thickness - the small local increase in thickness at the boundary due to the meniscus effect during casting was ignored. Using higher symmetry (such as 8th, 12th etc) is nominally possible due to the rotational symmetry of the membrane, but would result in highly distorted meshes of poor quality. Additionally, quarter (or half) symmetry is required if anisotropic materials or elliptical membrane boundaries are to be modelled.

6.3.2.1 Boundary conditions

Figure 6.1 shows the FEA model used, where internal "boundaries" (shown in red and blue) had symmetry boundary conditions applied. The membrane boundary (shown in green) was fully constrained in all 6 degrees of freedom. If the membrane boundary experiences motion relative to the clamp fixture during experiments, a fully constrained boundary condition would not be suitable, and a contact boundary condition would have to be used instead. As the membranes tested were bonded to the clamp fixture and experienced no delamination[5], a fully constrained boundary condition was considered sufficient.

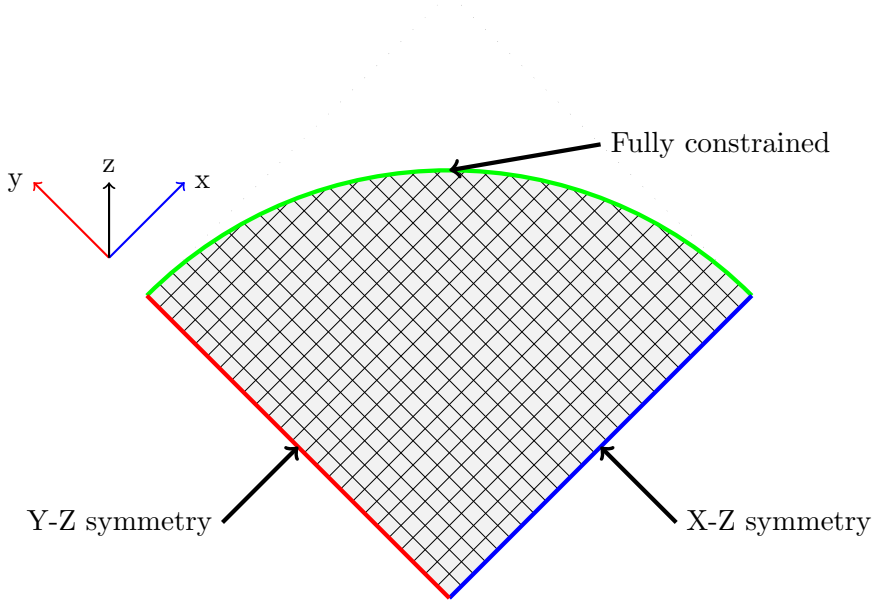

Figure 6.1 Quarter symmetry model of membrane, with boundary conditions shown. Pressure is applied to the $-Z$ side of the membrane (i.e. the "back")

6.3.2.2 Applied loads

The experimentally measured pressure data was applied to the entire surface of the membrane as a pressure load. This was a simple load case to apply, but was not entirely representative of the experiment. Applying the load this way causes the pressure in the FEA simulation to be independent of the behaviour of the membrane. In reality the pressure is affected by the membrane - it would be more accurate to measure initial piston velocity, and model the entire bulge tester system. This

[5]With the exception of two textile reinforced specimens, which were not modelled numerically

was beyond the scope of the project however, and would require significantly more measurement instrumentation on the experimental rig.

6.3.2.3 Material models

*MAT_077_O/*MAT_OGDEN_RUBBER* was used to model the membrane (as the membrane did not contain fibres). The quasi-static strain hardening exponents and shear moduli extracted from uniaxial tensile tests were used to model the elastic behaviour, and a 2 term Prony series was used to model the viscous behaviour. This material model includes frequency independent (Coulomb) damping, but this was turned off.

6.4 Bulge test parameter extraction

6.4.1 LS Opt

LS Opt is an optimisation and probabilistic analysis tool developed by Livermore Software Technology Corp (LSTC), which interfaces with LS Dyna (and other simulation packages). This software is capable of a variety of optimisation tasks, one of which is parameter extraction. LS Opt was used by Curry (2017) [37] to extract material properties of steel plates undergoing air-blast.

When defining material properties in LS Dyna, each property can be defined as either a constant or a variable (*PARAMETER). If the property is defined as a parameter, LS Opt is capable of changing it in order to reduce the difference between the simulated and experimental results.

The elastic properties of the Ogden model were set to the properties extracted from the uniaxial tensile tests, and the viscous damping properties were set as parameters. Unfortunately this approach did not work. The underlying cause of this failure is not definitively known, but appendix D covers this in more detail.

6.4.2 Manual parameter extraction

Given that the workarounds to the problems with LS Opt lay outside of the scope of this project, parameters were instead manually extracted. The entire simulation ran in approximately 3 minutes, and the material was modelled with 2 Ogden terms and 2 Prony series terms for a total of 8 variables. Ogden parameters from the tensile test data were used, and only the shear moduli were modified[6].

This approach was far from ideal, and was not feasible for a large number of tests. However, showing that manual parameter extraction for a single test is feasible implies that automated parameter extraction is feasible for an entire batch. Automated parameter extraction is faster, more efficient and more accurate than manual parameter extraction of this type.

[6] Shergold *et al* (2006)[22] found that apparent shear moduli of silicone change with strain rate, but shear hardening exponents do not

Chapter 7

Results

The uniaxial tensile test results at a variety of strain rates for the 3 skin simulants are first presented, showing their mechanical properties. Next the results of the speckle pattern methods used are shown and evaluated, followed by the results of the bulge test apparatus.

Contents

7.1 Uniaxial tensile tests

Mold Max 60 Duro

A 2 term Ogden model was fitted to the uniaxial tensile tests of 60 Duro silicone, as it was found that including more terms led to repetition of terms rather than increased accuracy. Note that compression tests were not performed, and the below parameters would likely give poor results in compression (much like the Neo-Hookean material model).

The Mold Max 60 Silicone appeared to undergo no plastic deformation prior to fracture - post-fracture specimens had no measurable change in length when compared to pre-fracture length mea-

surements. Additionally, there was minimal change in material properties after repeated tensile strain, indicating that the Mullins effect is not present to a significant degree.

The apparent modulus appeared to be relatively insensitive to strain rate, however the fracture stretch had a positive correlation with strain rate. This is speculated to be as a result of reduced time for cracks to spread across the specimen[1] at lower test times. As only a small number of tests were conducted, this speculation cannot be confirmed without conducting more experiments. The UTS also appeared to be strain rate dependent, likely as a result of both higher viscous forces and higher stretch ratios at high rates.

Table 7.1 Uniaxial tensile test results and Ogden Parameters for Mold Max 60 silicone

$\dot{\boldsymbol{\lambda}}$ (s^{-1})	**Fracture stretch**	**UTS (Cauchy)** (MPa)	$\boldsymbol{\alpha_1}$	$\boldsymbol{\alpha_2}$	$\boldsymbol{\mu_1}$ (kPa)	$\boldsymbol{\mu_2}$ (kPa)	$\boldsymbol{S_{est}}$ (%UTS)
2.2×10^{-1}	2.07 ± 0.06	3.89 ± 0.25	2.9 ± 0.0	3.8 ± 0.0	287.6 ± 8.3	114.4 ± 0.8	1.30
2.2×10^{-2}	1.94 ± 0.08	3.23 ± 0.36	2.9 ± 0.0	3.9 ± 0.0	270.0 ± 12.0	115.6 ± 1.6	1.32
2.2×10^{-3}	1.92 ± 0.10	2.92 ± 0.39	2.8 ± 0.0	3.8 ± 0.0	278.0 ± 0.9	112.7 ± 0.9	1.38

[1]Cracks in the surface of the specimen were observed occurring significantly prior to fracture when low strain rate tests were conducted

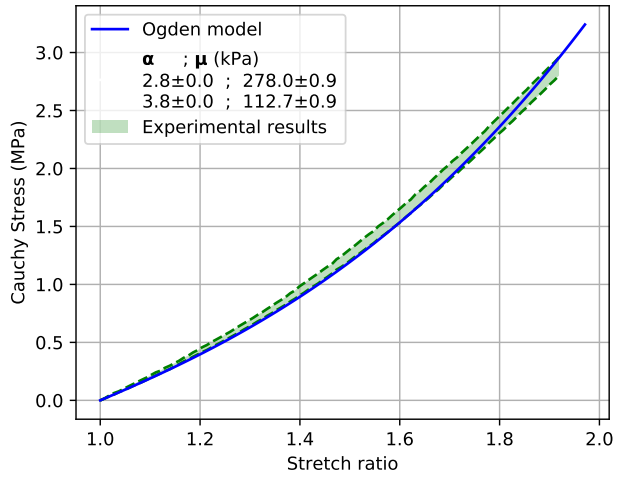

(a) $2.2 \times 10^{-3} s^{-1}$

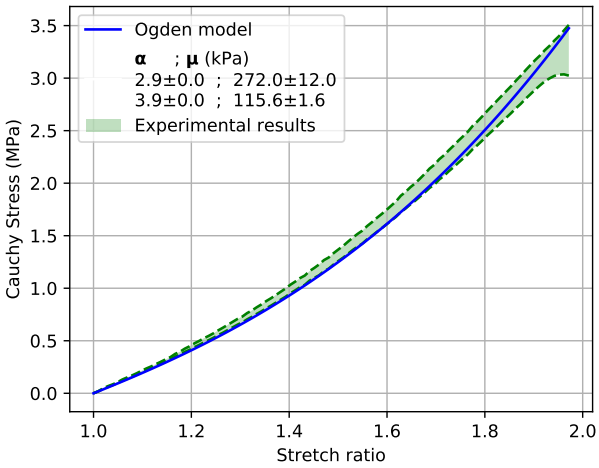

(b) $2.2 \times 10^{-2} s^{-1}$

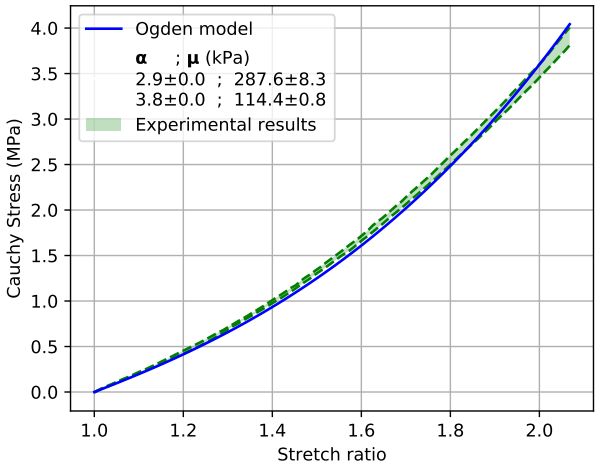

(c) $2.2 \times 10^{-1} s^{-1}$

Figure 7.1 2 term Ogden fits vs experimental data for uniaxial tensile tests of Mold Max 60 Duro silicone at strain rates of 2.2×10^{-3}(fig. 7.1a), 2.2×10^{-2}(fig. 7.1b), and 2.2×10^{-1}(fig. 7.1c). Experimental results shown as a band $\pm$ 1 standard deviation about the mean, and the mean Ogden fit is shown

Dragon Skin 10 Duro

These specimens were not tested to failure due to limitations on the cross-head travel of the tensile tester, but were instead tested to a stretch ratio of 7. The manufacturer's datasheet maintains that this material will fracture at a stretch of approximately 11 (1000% engineering strain).

Table 7.2 Uniaxial tensile test results and Ogden Parameters for Dragon Skin 10 silicone

$\dot{\boldsymbol{\lambda}}$ (s^{-1})	**Peak**[1] **stretch**	**Peak**[1] **Stress (Cauchy)** (MPa)	$\boldsymbol{\alpha_1}$	$\boldsymbol{\alpha_2}$	$\boldsymbol{\mu_1}$ (kPa)	$\boldsymbol{\mu_2}$ (kPa)	$\boldsymbol{S_{est}}$ (MPa)
2.2×10^{-1}	7.02 ± 0.03	7.94 ± 0.44	1.0 ± 0.0	3.0 ± 0.1	131.0 ± 3.1	21.5 ± 0.6	0.05
2.2×10^{-2}	7.00 ± 0.00	6.89 ± 0.44	0.9 ± 0.0	2.9 ± 0.0	129.6 ± 1.7	20.9 ± 0.5	0.05

[1]This is the peak stretch/stress measured during the test, and not fracture stress/UTS

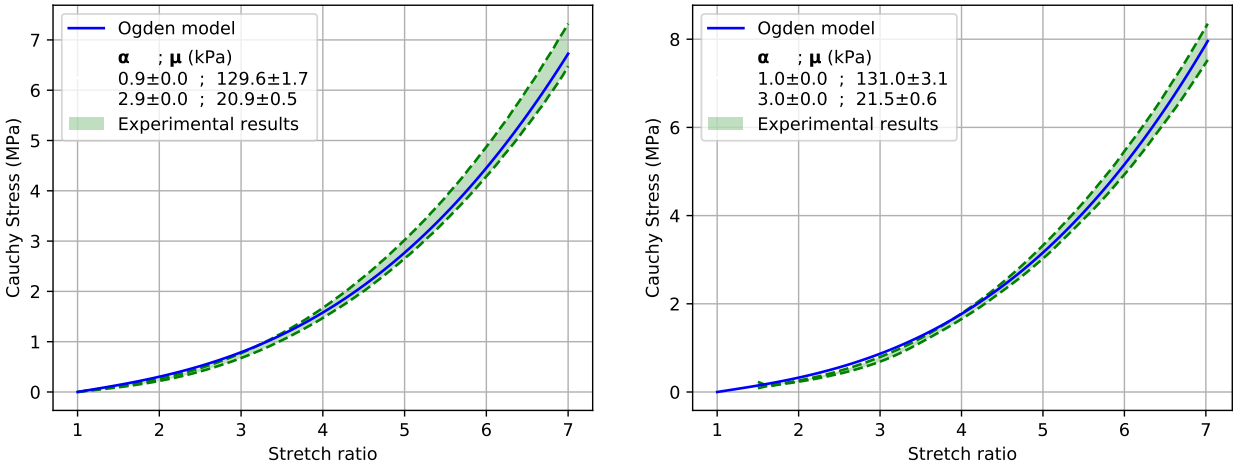

(a) Strain rate of $2.2 \times 10^{-2} s^{-1}$

(b) Strain rate of $2.2 \times 10^{-1} s^{-1}$

Figure 7.2 Cauchy Stress vs stretch ratio for Dragon Skin 10 silicone uniaxial tests. Experimental results shown as a band $\pm$ 1 standard deviation about the mean, and the mean Ogden fit is shown

Figures 7.2a and 7.2b and table 7.2 show the experimental Cauchy stress vs stretch and Ogden parameters for Dragon Skin 10 under uniaxial tension. The experimental results are shown as a band one standard deviation above and below the mean result. The final column of table 7.2 shows the average standard error S_{est} of each Ogden fit and the corresponding experimental results. The peak measured stretch ratio is not a material property (as the specimens were not tested to fracture), but is shown (along with the peak measured stress) in order to give the reader a sense of the material behaviour beyond the Ogden Parameters.

Note the somewhat higher strain rate sensitivity compared to the Mold Max 60 material - a strain rate increase of only one decade increases the stiffness by approximately 15% (comparing Cauchy stress

at a stretch ratio of 7). Whilst the UTS of the Mold Max 60 material increased with strain rate, this occurred in conjunction with an increase in fracture strain.

Unlike the Mold Max 60 specimens, this material exhibited the Mullins effect to a significant degree. As a result, care was taken to avoid straining any membrane or uniaxial tensile samples prior to testing in order to achieve consistent results.

Textile Reinforced Silicone

The tensile samples tested consisted of a 1mm thick textile reinforced silicone layer (1 layer of bandage), and 4mm of silicone. They were modelled up until fracture/snapping of fibres, at which point the fibres began to delaminate and the data became highly erratic. The 1mm thick textile reinforced layer was manufactured from one layer of bandage and a 0.8mm thick layer of liquid silicone, and was therefore modelled as 80% silicone by volume/cross sectional area (making the 5mm thick specimen 96% silicone by volume). The silicone matrix material was identical to the silicone material shown in table 7.2. The fibre stiffness ratio was calculated from the average toe region and linear region stiffness, and the uncertainty was calculated based on an assumption of a normal distribution. The uncertainty shown here is the projected standard deviation, rather than a standard deviation directly calculated from results. Note that the Modified Weiss model overestimates the toe region stiffness in the warp direction - these stiffness ratios were calculated directly from experimental data rather than from the fitted modified Weiss model.

Table 7.3 Fibre parameters for textile reinforced silicone

C_1 (MPa)	C_2 (MPa)	C_3	C_4 (MPa)	λ_{crit}	$\boldsymbol{S_{est}}$ (MPa)
102.5 ± 8.13	0.832 ± 0.154	3.30 ± 0.36	36.8 ± 5.51	1.69	2.82

Table 7.4 Uniaxial tensile test results for textile reinforced silicone

Fracture stretch		**Fibre UTS** (MPa)		**Fibre stiffness ratio**	
Warp direction	Weft direction	Warp direction	Weft direction	Toe region	Linear region
2.17 ± 0.11	1.23 ± 0.03	53.8 ± 3.36	22.6 ± 1.71	17.5 ± 3.2	2.79 ± 0.32

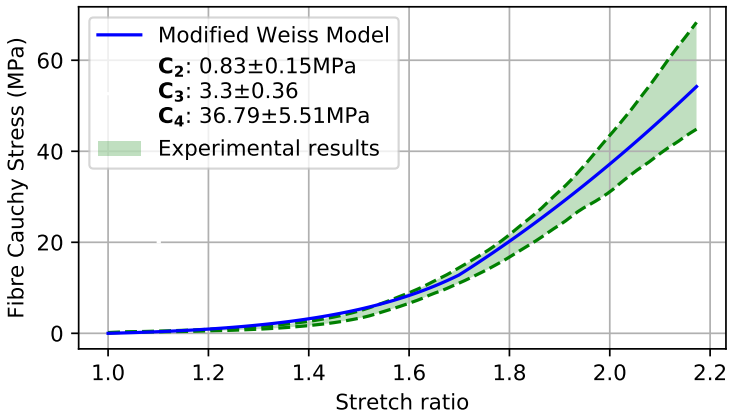

Figure 7.3 Fibre Cauchy stress vs stretch ratio for uniaxial tensile tests of textile reinforced silicone in the warp direction.

7.2 Evaluation of speckle pattern generation methods

Both speckle pattern methods solved the problems associated with traditional spray paint based speckle patterns, but were more difficult to apply.

7.2.1 Information density and robustness of pattern

Information density

For an unstrained membrane, the silicone based speckle pattern generally resulted in correlation residuum of 0.1 to 0.4 pixels, whilst the graphite based pattern generally resulted in a correlation residuum of 0.5 to 1.5 pixels. This indicates that the silicone based speckle pattern had a higher information density than the graphite based speckle pattern, and could be tracked with less uncertainty.

Figure 7.4a shows a graphite based speckle pattern with large, coarse speckles. It was thought that increasing the density and reducing the size of the speckles (to generate a pattern more like fig. 7.4c) would lead to better correlation accuracy, but in practice this reduced both robustness and accuracy of the correlation. It is not clear why this was the case, and further investigation is needed before definitive conclusions are drawn.

The speckle density of fig. 7.4c should be higher if the recommendations of Park *et al* [48] are to be followed (see fig. 2.21), but increasing speckle density was found to result in large, coarse speckles - reducing information density. The liquid silicone has a high surface tension, and speckles in contact with one another tended to merge into a single large speck.

Robustness of speckle pattern

As the membrane strain increased, the correlation residuum of the graphite based speckle pattern was largely unaffected, and the graphite flakes did not change colour. The graphite based speckle pattern allowed for detection of strains in excess of 300%.

The correlation residuum of the silicone based speckle pattern did not change much below strains of $\approx 100\%$, but rapidly increased as the strain approached 100%. This is likely to be as a result of the

silicone changing colour when it stretches, causing the Grey Value Intensity Profile tracking method of the DIC to lose accuracy. Additionally, the silicone speckles (regardless of colour) had a higher reflective index than the graphite, leading to increased glare/reflections. Glare reduces the accuracy of DIC, and can lead to complete loss of correlation in some cases[2] .

It was found that black (grey) silicone speckles on a white background led to reduced DIC correlation accuracy when compared to white silicone speckles on a dark red or black background. The white pigment used appeared to have a greater effect on the silicone than the black pigment (turning it opaque more quickly). The author speculates that thin white silicone specks on a thick black membrane are more effective than thin black silicone specks on a thick white membrane.

The graphite based speckle pattern is significantly more robust than the silicone based speckle pattern at high strains.

Out of interest, the silicone speckle pattern generation method was also tested on steel plates undergoing blast loading. This generated promising results, but is outside of the scope of this project. Results from this test are covered in further detail in appendix E.

7.2.2 Grey value intensity profile

As discussed in section 2.6.2.3, Park *et al* (2017) [48] maintain that the grey level intensity profile of a DIC speckle pattern should match fig. 7.4b. Neither of the speckle patterns shown in fig. 7.4d matches that suggested by Park *et al* , but the graphite based pattern comes closest.

[2]Glare can cause local oversaturation of the sensor, causing all of the pixels in a region to have the same (maximum) intensity value. This prevents the grey scale intensity tracking method from working, and causes a complete loss of correlation for facets in the region of the glare.

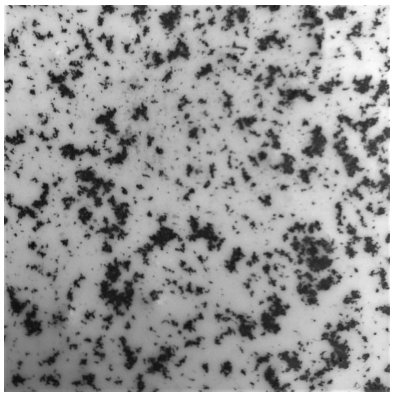

(a) Graphite speckle pattern

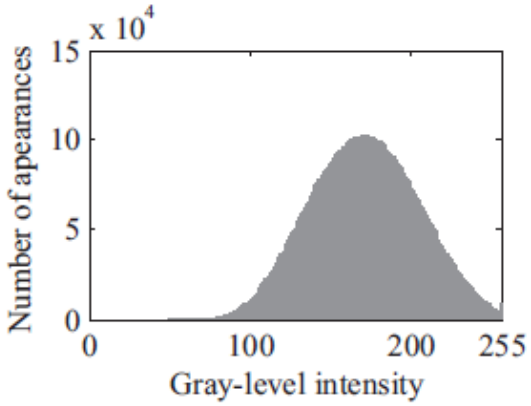

(b) Grey level intensity profile suggested by Park *et al* (2017)

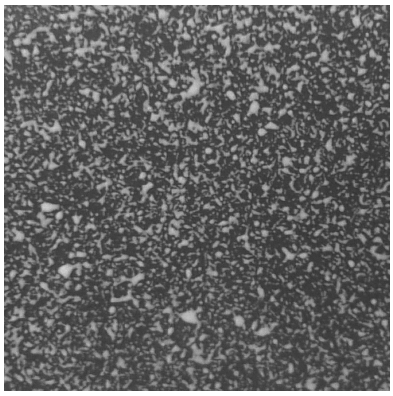

(c) Silicone speckle pattern

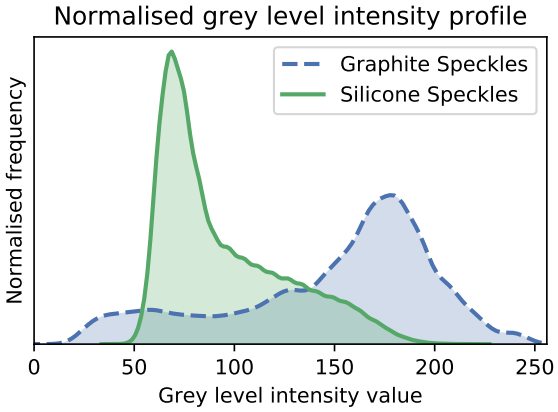

(d) Grey level intensity profile of speckle pattern

Figure 7.4 Grey level intensity profile of speckle patterns used, and grey level intensity profile suggested by Park *et al*

7.2.3 Speckle pattern repeatability

The graphite based speckle pattern was difficult to apply consistently, and had a high degree of variance between specimens. In contrast, the silicone based speckle pattern was easy to apply, and had a high degree of repeatability.

7.2.4 Speckle pattern primarily used

At strains below 100% the silicone based method was superior to the graphite based method in every way from a DIC point of view. Additionally, it likely that the presence of fine graphite flakes embedded in the surface of the silicone membrane would affect the mechanical properties of the membrane. The graphite based method is only viable for translucent silicone, and does not work for opaque silicone (as the graphite flakes sink slightly beneath the surface of the silicone). This prevents the graphite based method from being used with the Mold Max 60Duro silicone for instance. For these reasons the silicone based pattern was used for the majority of specimens tested.

7.3 Bulge testing

The device was first fired with a nominally rigid membrane (4mm thick Perspex) at various driving pressures in order to evaluate the repeatability of the apparatus independently of the effects of membrane variability. Tests of Dragon Skin 10 were then done, followed by 2mm thick textile reinforced silicone, Mold Max 60, and then 3mm thick textile reinforced silicone. Once these tests had been completed, tests were run at very low and very high strain rates.

The initial tests of Dragon Skin 10 experienced significant problems with the high speed cameras, leading to a complete loss of DIC data for several tests. These tests were not repeated, as it was felt that additional testing of Mold Max 60 membranes would be of greater value.

7.3.1 Closed ended cylinder

In order to evaluate the pressure supply independently of membrane effects, the membrane was replaced with a (nominally rigid) 4mm thick Perspex sheet. Each test was conducted 5 times, at driving pressures of 150,200,250, and 300kPa with a 600g piston and open vents. Only the piston with phosphor bronze bushings was tested, as preliminary testing had found that most friction is due to the rubber O rings rather than the bushings.

7.3.1.1 Consistency

Table 7.5 *Actual vs theoretical peak driven pressure with 600g piston, open vents and rigid membrane*

	Driving pressure (kPa)			
	150	200	250	300
Theoretical Peak Driven Pressure (kPa)	810	1120	1495	1940
Peak Driven Pressure (kPa)	84.02	178.3	366.5	690.5
% Sdev	13.8(9.5)	6.1(3.5)	7.7(2.0)	3.9(1.7)
% Pressure loss	90%	84%	75%	64%

Table 7.5 shows the actual vs theoretical peak pressure in the driven section of the pump tube for various driving pressures. The peak pressure is defined as the maximum pressure (i.e. when the piston is at maximum extent) in the driven section of the pump tube. Percentage standard deviation is shown for the whole set of results, and in brackets for results with outliers removed. Note that as the driving pressure increases, both the efficiency and the repeatability increase. The percentage standard deviation once outliers have been removed has no value as an indication of the reliability of the device, but does indicate that the unexpected decrease in reliability at 250 kPa driving pressure is likely due to outliers in the measured data rather than an intrinsic property of the driving pressure.

As the driving pressure increases, the efficiency and consistency of the device increases. This is expected, as friction losses will form a diminishing percentage of of the total energy in each pressurisation event.

Source of outliers: The large discrepancy between the standard deviation with and without outliers indicates that each outlier lies far away from the mean. Close inspection of the piston showed slight dents in the phosphor bronze bushings, indicating that the piston may occasionally impact the edges of the vents in the centre of the pump tube.

7.3.1.2 Pressure profile

When designing and building the device, it was assumed that the effects of shock wave dynamics could be ignored. The air in the driven section was modelled as uniform isentropic compression, given that the piston velocity was significantly below the speed of sound in the pump tube ($\approx 345m/s$).

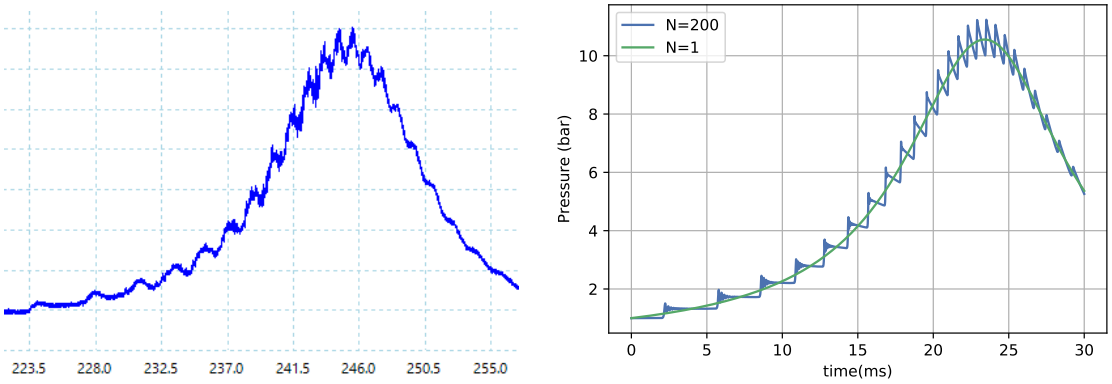

(a) Section of pressure reading taken with rigid membrane, prior to any noise filtering or voltage to pressure conversion. Each x axis division represents $4.5ms$

(b) Simulated pressure reading, with 200 Lagrangian elements and 1 Lagrangian element (uniform isentropic compression). Each x axis division represents $5ms$.

Figure 7.5 Actual vs simulated pressure profile. Note that the overall pressure profiles are slightly different, as the simulation does not take friction into account – the purpose of this image is to demonstrate that the spikes are not an experimental or measurement artefact.

As can be seen in fig. 7.5a, there appear to be pressure waves superimposed on the pressure profile that would be expected from uniform isentropic compression. The period of the first wave is approximately $4.4ms$, with each subsequent wave having a shorter period. This is likely due to the effect of pressure wave propagation within the pump tube. When the piston first enters the pump tube, the tube length is $0.77m$, and the speed of sound in the gas is approximately $343m/s$. It would therefore take approximately $4.49ms$ for the wave to reflect across the length of the pump tube, which is similar to the period of the first wave[3]. Each subsequent wave would have a shorter period, as the tube length decreases and the speed of sound increases (due to isentropic heating of the gas). The measured oscillations were not due to stress waves propagating through the steel of the pump tube, as the frequency was an order of magnitude too low. A compressive/tensile wave would take approximately $0.24ms$ to travel down the length of the tube, resulting in a frequency of $0.48ms$[4]

In order to validate this theory, a simple 1D Lagrangian CFD code was written, the results of which are shown in fig. 7.5b. When only one element is used (i.e. uniform isentropic compression),

[3]Twice the length over the fluid wave speed, i.e. $\frac{2\times 0.77m}{343m/s} = 4.49ms$

[4]The device is approximately $1.4m$ long, and the speed of sound in steel is approximately $5800m/s$. As a result, the first vibrational mode of the device is expected to have a frequency of approximately $0.48ms$

a smooth curve is generated. When multiple elements are used, the effects of pressure propagation within the pump tube are clearly visible. The waves shown in fig. 7.5b when using 200 elements follow the expected frequency, with an initial period of $\approx 4.4ms$ and a decreasing period for each subsequent wave. Increasing the number of elements above 200 did not significantly change the results of the simulation[5]. This numerical model is described in greater detail in appendix F.

While crude, this numerical code served its purpose. It confirmed that the measured pressure oscillations were not spurious, and had a simple physical explanation.

[5] As the shock front is a discontinuity, an infinite number of elements are required in order to fully capture it. As a finite number of elements are used, there are some spurious high frequency oscillations centred after each shock front (much like the oscillations in a low order Fourier approximation of a square wave)

7.3.2 Mold Max 60

The following sections consist primarily of plots of DIC data. Particularly with the Mold Max 60 membranes at high driving pressures, the DIC generally lost correlation a few frames before the membrane burst due to a combination of motion blur and speckle pattern distortion [6]. It should be noted that the maximum measured strain is sometimes lower than the fracture strain as a result of this. Membrane burst pressure vs clamp geometry and driving pressure is shown in section 7.3.2.3.

7.3.2.1 Repeated, nominally identical tests

Five 2mm thick, 50mm diameter circular membranes were tested with a 600g piston at 250 kpa driving pressure and open vents. Figure 7.6 shows the membrane pressure, stretch ratio and z displacement at the apex. The dark plot lines represent the mean, with the dashed lines representing one standard deviation above/below the mean.

The variance in the pressure data per test is small compared to the variance in the strain and displacement data, indicating that a large portion of the variance is from the membranes themselves rather than the bulge tester.

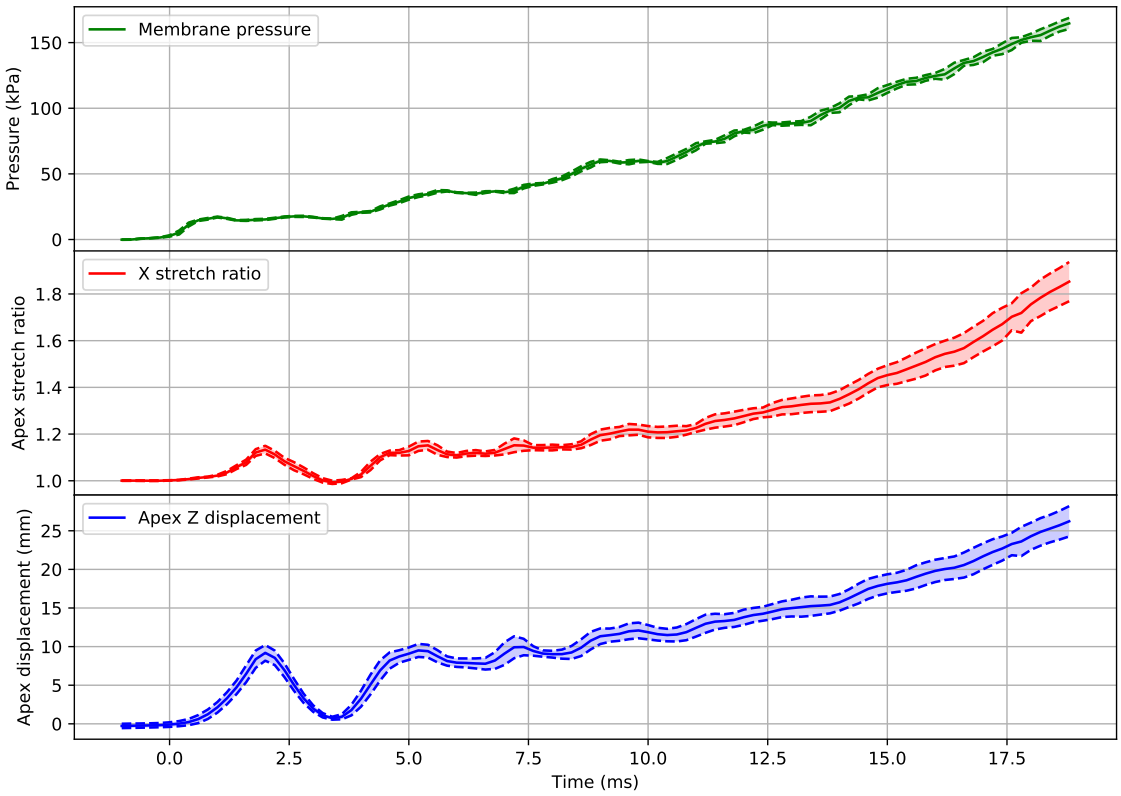

Figure 7.6 Plot of pressure, apex stretch, and apex z displacement vs time for 50mm diameter, 2mm thick Mold Max 60 membranes with 250kPa driving pressure, open vents and a 600g piston.

[6]The motion blur of the images often increased noticeably a few frames before the first cracks were visible to the naked eye. This was unexpected, as the cracks had been expected to initiate at the surface facing the camera (where the strain was the highest due to bending effects)

Likely reasons for membrane variability Whilst care was taken to ensure consistent casting conditions for all membrane samples, there are several likely sources of variability:

1. Mold Max 60 has a short shelf life. This silicone was cast shortly after purchase, but it is not known how long it aged between manufacture and purchase
2. Vacuum degassing was not used when casting specimens. This was not a problem for the Dragon Skin 10 membranes, but the Mold Max 60 membranes exhibited minor porosity.
3. Mold Max 60 undergoes no observable plastic deformation prior to fracture. As a result, the membranes will be particularly sensitive to any imperfections and stress concentrations - causing premature failure.

7.3.2.2 Varying driving pressure and membrane geometry

Figure 7.7 shows the apex stretch ratio vs time for a variety of membrane clamp geometries and driving pressures. For clarity, only tests with comparable driving pressure are plotted - tests at 170 and 230 kPa are omitted from the plots.

Quality of strain rate The initial membrane behaviour is clearly dominated by dynamic (inertial) effects, with large variations in strain rate. This dynamic behaviour has mostly damped down by $10 - 15ms$, resulting in a smoother strain rate. Table 7.6 shows that a straight line closely matches the strain from $10ms$ to $30ms$ for each test, with R^2 being above 0.95 for 81% of tests.

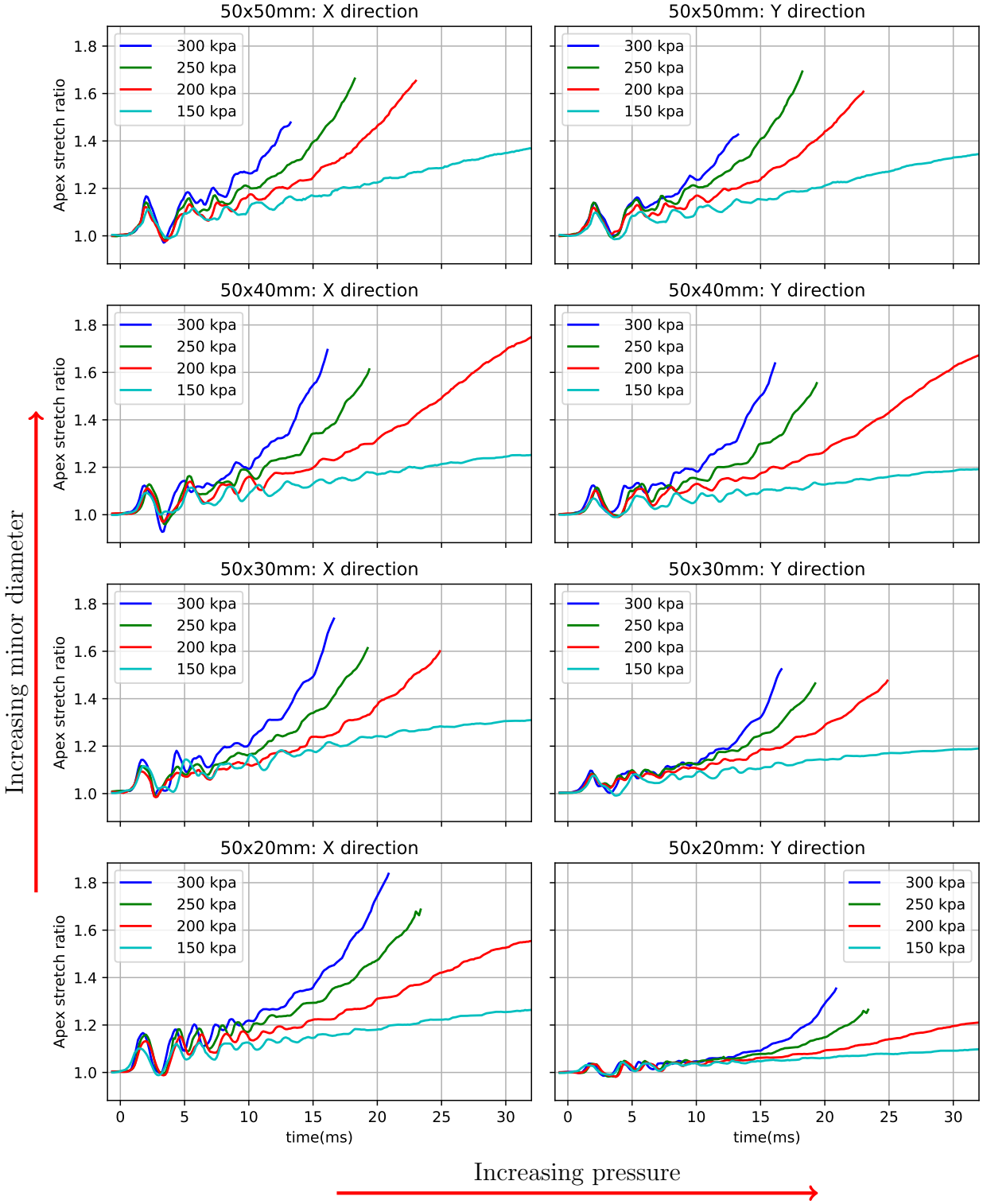

Figure 7.7 Apex strain in x (minor) and y (major) directions vs time for varying membrane geometry and driving pressure. All membrane major diameters were 50mm, and minor diameters were 20,30,40 and 50mm. Piston was 600g, with a piston driving pressure of 150,200,250 and 300 kpa. Curves which reach the far right of the time axis were truncated for plotting purposes, as the membrane did not burst.

Effect of driving pressure on strain rate Prior to $5ms$, changing the driving pressure appears to change only the magnitude of the strain, with minimal effect on the frequency of the oscillation (see fig. 7.7). This is expected, as the initial dynamic behaviour is largely an intrinsic property of the membrane's natural frequency of vibration.

After $10ms$, the strain rate is strongly affected by the piston's driving pressure. A best fit straight line from $10ms$ until $30ms$ was generated for each test. These strain rates are plotted in fig. 7.7, and shown in table 7.6.

For a membrane of given geometry, there is a strong linear correlation between driving pressure and apex strain rate. This relationship holds for both major and minor axis strains, and can be seen in the top two plots of fig. 7.8.

Effect of membrane geometry on strain rate The bottom two plots of fig. 7.8 show the effect of changing membrane geometry for constant driving pressure. Increasing the diameter ratio has a strong positive effect on the strain rate in the major axis direction, but a weaker effect on the strain rate in the minor axis direction.

A diameter ratio of 0.8 appears to result in lower minor axis strains than a diameter ratio of 0.6 at driving pressures of 150-250kPa. This is unexpected, and is unlikely to be a spurious result given how consistently it occurs. All membranes in this series of tests were cast in the same batch, so it is unlikely to be due to a casting defect in all of the membranes with a diameter ratio of 0.6.

When observing high speed video of the tests, some form of resonance appeared to occur for membranes with a diameter ratio of 0.6. Figure 7.8 shows that membranes with a diameter ratio of 0.6 burst at lower pressure than membranes with a diameter ratio of 0.8 - this implies that the resonance theory may have some merit. There is insufficient data to give a conclusive explanation, but FEA simulations of various diameter ratios would augment the understanding gained from these tests.

Outlier datapoint A major exception to the trend for both pressure and geometry is the strain profile exhibited by the circular membrane tested at 300kPa driving pressure. This outlier is thought to be as a result of a flaw in the cast membrane as:

1. This membrane burst at a significantly lower strain than other membranes (see the blue line on the top two plots of fig. 7.8)
2. This membrane appeared to exhibit anisotropy. The apex strain was not equi-biaxial, in spite of a circular membrane boundary and nominally symmetric loading conditions.

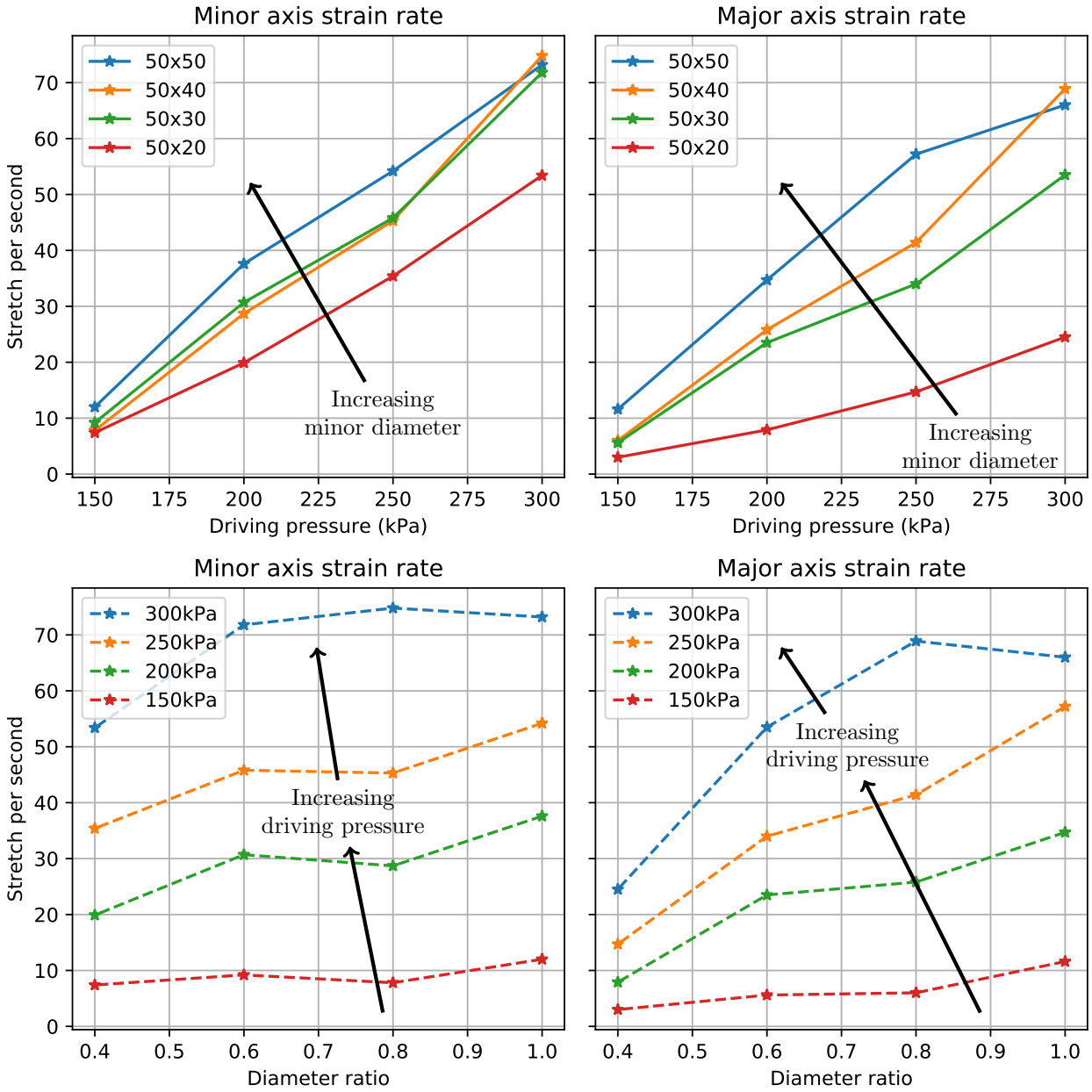

Figure 7.8 Apex strain rate in major and minor axis directions vs driving pressure and membrane diameter ratio for 2mm thick Mold Max 60 membranes with a 600g piston and open vents

Table 7.6 *Average strain rate (stretch per second) from 10ms to 30ms for various membrane geometries and driving pressures. R^2 value indicates goodness of fit for constant strain rate curve fit. Used to plot fig. 7.8*

Diameter ratio	**Axis**	**Driving pressure (kPa)**							
		150		200		250		300	
		$\dot{\lambda}$	R^2	$\dot{\lambda}$	R^2	$\dot{\lambda}$	R^2	$\dot{\lambda}$	R^2
1.0	X	12.0	0.987	37.6	0.95	54.2	0.958	73.2	0.985
	Y	11.6	0.988	34.7	0.955	57.2	0.956	66.0	0.99
0.8	X	7.8	0.961	28.7	0.968	45.3	0.95	74.8	0.959
	Y	6.0	0.965	25.8	0.959	41.4	0.939	68.9	0.956
0.6	X	9.2	0.936	30.7	0.968	45.8	0.965	71.8	0.939
	Y	5.6	0.95	23.5	0.955	34.0	0.95	53.5	0.914
0.4	X	7.4	0.98	19.9	0.984	35.4	0.956	53.4	0.938
	Y	3.0	0.98	7.9	0.964	14.7	0.901	24.5	0.871

7.3.2.3 Burst pressure vs membrane geometry, driving pressure

As membrane minor diameter decreases, the burst pressure increases – this is expected, and predicted by cylinder theory. The burst pressure also increases as the driving pressure increases - this latter result is likely due to:

1. Viscous damping effects - at higher strain rates, viscous damping effects of the silicone increase the apparent modulus of the material due to inherent visco-elasticity
2. Membrane inertia - at higher driving pressures the membrane is accelerated forwards faster. As a result, driving pressure at a given strain state increases, as the inertial forces have increased
3. Increasing fracture strain - for both uniaxial and biaxial tension tests, Mold Max 60 silicone appeared to have a positive correlation between strain rate and fracture strain.

Table 7.7 *Maximum pressure vs membrane geometry and driving pressure for 2mm thick Mold Max 60 membranes with a 600g piston and open vents. Membranes which burst are indicated by an asterisk*

Diameter ratio	Driving pressure (kPa)					
	150	**170**	**200**	**230**	**250**	**300**
1.0	95.9	124.5	174.6*		212.3*	229.6*
0.8	98.2		191.5	225.9*	251.4*	248.8*
0.6	105.9	156.0	218.3*		268.1*	293.4*
0.4	122.1		246.2	335.1	421.0*	511.9*

7.3.3 Textile reinforced silicone

The textile reinforced silicone samples exhibited wide inter-sample variability. Combined with the small number of tests conducted relative to the Mold Max 60, this resulted in a dataset with a high degree of scatter.

7.3.3.1 Detecting warp and weft axis

One of the advantages of bulge testing over other planar tension test methods is that the direction of anisotropy is not presupposed before the test, but rather detected during the test[1]. As a result, it is important that the direction of anisotropy is detectable.

Whilst the elliptical textile reinforced specimens were cast with the weft axis parallel to the major axis, the circular specimens were deliberately not cast in a specific alignment. This meant that the axis of anisotropy was not visually detectable in the DIC images, and had to be detected from the deformation field measured by the DIC measurement. Note that they axis of anisotropy could be visually detected on the back (non-speckled) surface of the membranes, allowing for validation of the axis of anisotropy detected by DIC.

For an anisotropic membrane with a circular boundary, the z displacement contours will be elliptical, and the x and y displacements will be symmetric about the axis of anisotropy. Tonge (2014) [1] detected the direction of anisotropy by looking at the direction of the major and minor axis of the z displacement contours, as well as the symmetry of the x and y displacements.

In this investigation, it was found that examining the distance between the membrane surface and a best fit sphere (BFS) was the easiest method for determining the direction of the fibres. If the membrane is homogenous, the principal strains at the apex should align with the axis of anisotropy, with minimal shear.

Figure 7.9 shows the displacement contour of a textile reinforced silicone membrane specimen. Note that the direction of the axis of anisotropy is significantly more detectable in fig. 7.9b than in fig. 7.9a.

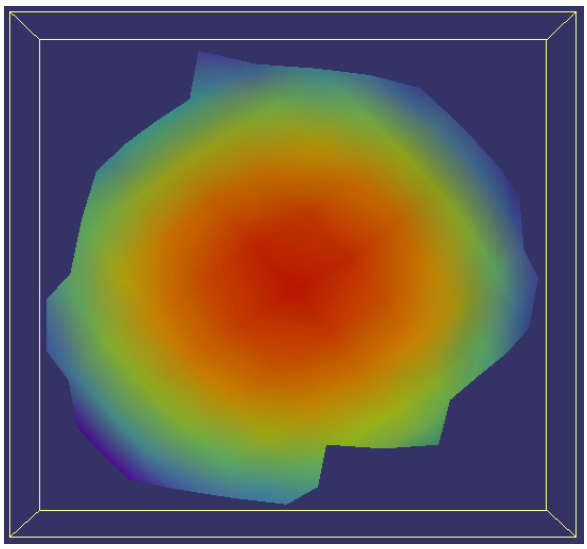

(a) Z displacement contour of textile reinforced specimen, with elliptical contour major axis horizontally aligned

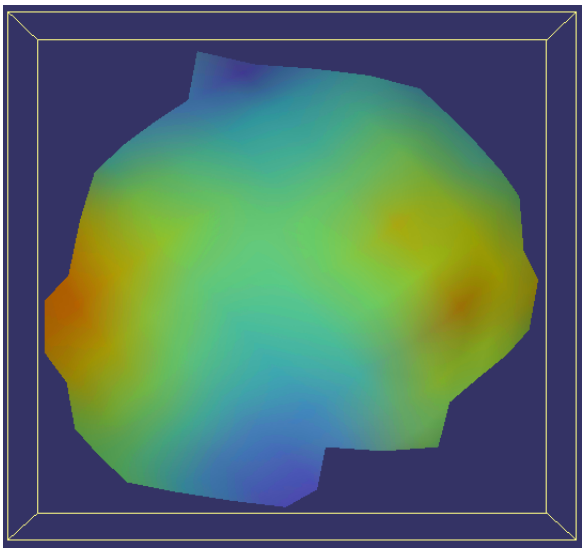

(b) Distance to best fit sphere (BFS). Direction of anisotropy is significantly more easily detected.

Figure 7.9 Displacement countour of a textile reinforced silicone membrane. Both images are of the same membrane. In both images blue represents a small value and red a large displacement, however it is difficult to detect anisotropy in fig. 7.9a. In contrast, fig. 7.9b clearly shows that the axis of anisotropy is left:right; the red lobes represent where the ellipsoidal shape deviates furthest from a spherical fit.

7.3.3.2 Effect of driving pressure

Figure 7.10 shows the apex stretch ratio vs time for five circular textile reinforced membranes tested at a variety of driving pressures with a 600g piston and open vents. All five membranes were 3mm thick with 2 layers of textile reinforcement. Increasing the driving pressure clearly increases the strain rate, but there is significant variance in the strain rate as well as strain rate profile across specimens. This is likely to be as a result of inter-specimen variability, as the textile reinforced specimens exhibited significant heterogeneity.

7.3.3.3 Effect of membrane geometry

Eight tests were conducted on textile reinforced membranes with varying geometry, but only five of these tests yielded useful data due to teething issues with the high speed cameras. Figure 7.11 shows the effect of membrane geometry on apex strain profile for given driving pressure. Due to the small number of data-points, and high degree of specimen variability, conclusions cannot be drawn with a high degree of confidence. The tests at 250kPa driving pressure suggest that the apex displacement increases as the minor diameter increases; this result is expected and consistent with both cylinder theory and other tests.However, the tests conducted at 300kPa driving pressure show the opposite. Given that only two tests were successfully conducted at 300kPa, it is likely that the unexpected results from these tests are due to specimen variability rather than a genuine effect. More tests are required before firm conclusions can be drawn.

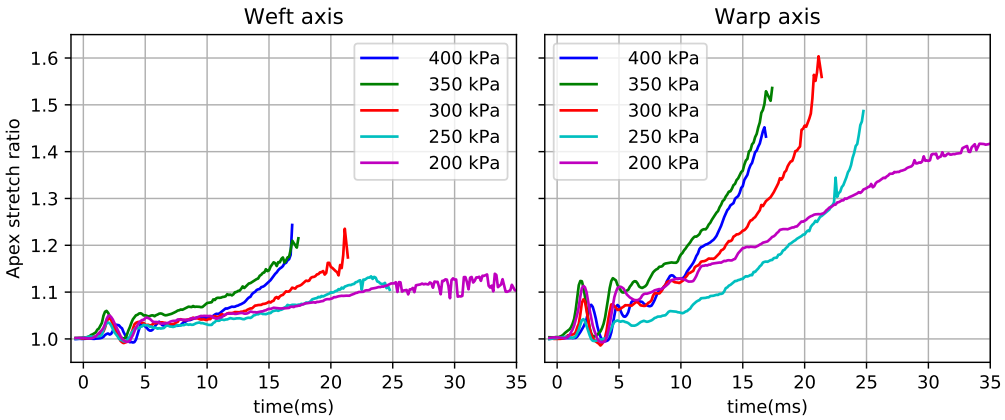

Figure 7.10 Apex stretch in warp and weft axis vs time for 50mm diameter, 3mm thickness textile reinforced silicone membranes for a variety of driving pressures with a 600g piston and open vents

7.3.3.4 Quality of strain rate

Much like the Mold Max 60 membranes, the initial portion of the bulge test was dominated by inertial effects, with a highly non-constant strain rate. The initial oscillations died down significantly faster however, and had predominantly damped down by $5ms$.

Due to the high degree of material non-linearity and heterogeneity exhibited by the textile reinforced specimens, the strain rate profile was inferior to the strain rate profile exhibited by the Mold Max 60 specimens.

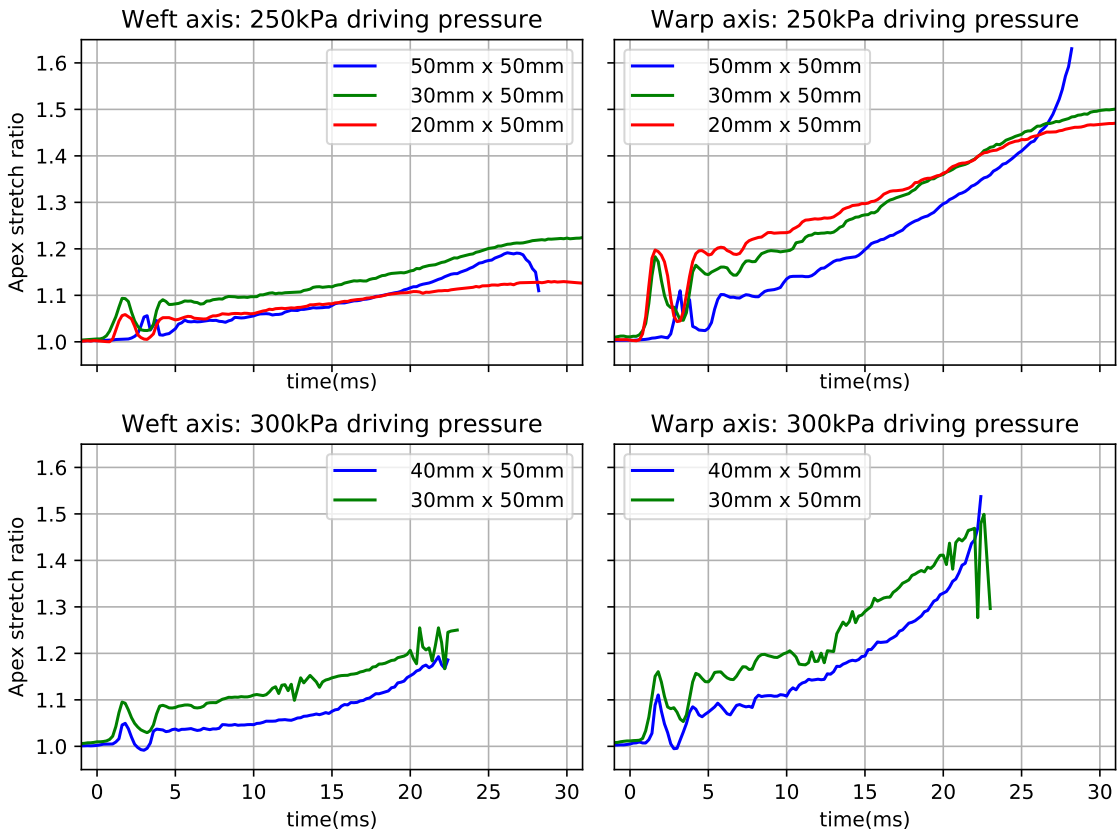

Figure 7.11 Apex stretch in warp and weft axis vs time for 2mm thick textile reinforced silicone membranes with two layers of textile reinforcement and varying membrane geometry. Pressure is constant for each plot, and each test uses a 600g piston and open vents.

7.3.4 Dragon Skin 10

The Dragon Skin 10 membranes were the first membranes tested, and experienced significant teething problems with one of the high speed cameras. Images from one of the cameras were often lost, likely due to a damaged data cable. Given that the burst pressure for the Dragon Skin 10 membranes was of a similar order of magnitude to the resolution of the pressure signal, the tests with lost data were not repeated. It was instead decided that additional tests on the Mold Max 60 material would be of more experimental value.

Given the low number of tests with data, meaningful conclusions about intermediate strain rate tests on Dragon Skin 10 cannot be drawn. Only the extreme (very high or very low strain rate) tests on Dragon Skin 10 are shown. These results are shown in sections 7.3.5 and 7.3.6.

7.3.5 Minimum strain rate tests

In order to evaluate the lowest achievable strain rate, tests were conducted with closed vents and a 1600g piston on both Mold Max 60 and Dragon Skin 10 membranes. All membranes tested were circular, with a diameter of 50mm and a thickness of 2mm.

7.3.5.1 Mold Max 60

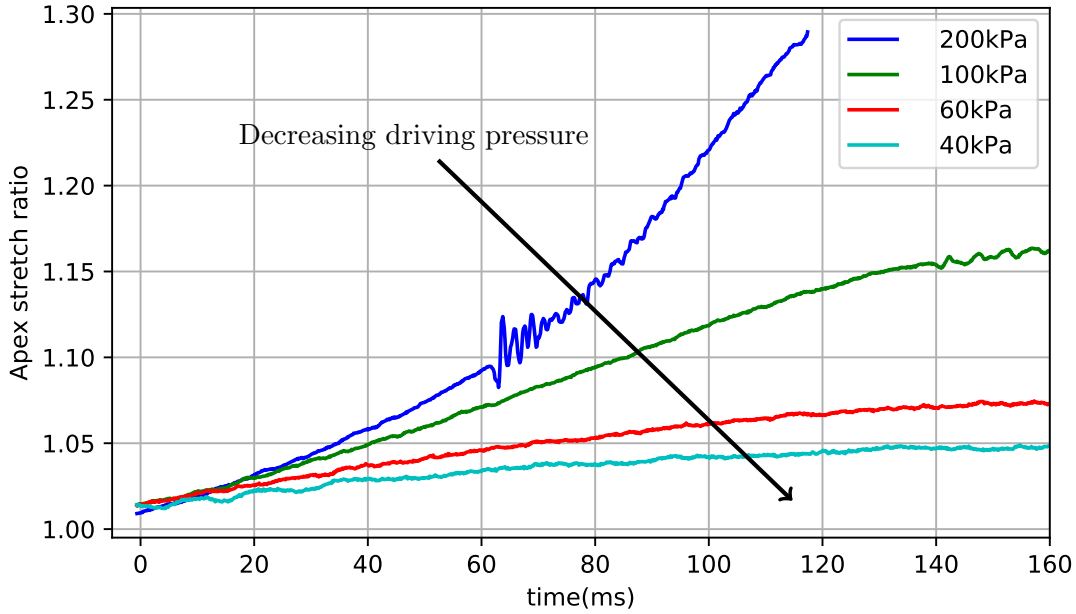

Figure 7.12 Apex stretch vs time for circular, 50mm diameter, 2mm thick Mold Max 60 membranes at a variety of driving pressures. Vents are closed for each test, and a 1600g piston is used.

Figure 7.12 shows the results of these tests on Mold Max 60. Note that the apex stretch at time zero is not unity. This is an artefact of how the start of the test was defined, and not a result of spurious DIC strain measurements. The start of each test was defined as the time at which the membrane pressure rose above 2kPa, and each test was plotted from 5 frames prior to the "start" of the test. For high strain rate tests (i.e. light piston, open vents, high driving pressure), this is a perfectly adequate measure of the start of the test, as the pressure rises rapidly and the membrane displacement lags the pressure by approximately $1ms$. With closed vents and a heavy piston, the pressure rises very slowly at first, allowing the membrane to undergo a small amount of deformation before the pressure reaches 2kPa.

Strain rate Defining the start of the test to be when the pressure reached 2kPa, and the end of the test to be when the pressure reached a maximum, best fit straight lines were fitted to the stretch:time curves shown in fig. 7.12.

Test at 200kPa Unlike the other low strain rate tests, the test at 200kPa exhibited early fracture and significant vibration. The vibration at $65ms$ is likely caused by the edge of the piston hitting the central vents, briefly accelerating the entire bulge tester forwards slightly and vibrating the membrane.

Table 7.8 *Strain rate vs driving pressure for 50mm diameter, 2mm thick Mold Max 60 membranes with closed vents and a 1600g piston*

Driving pressure (kPa)	**Strain rate** (s^{-1})	**Goodness of fit** (R^2)
200	2.28	0.941
100	1.09	0.997
60	0.468	0.992
40	0.263	0.954

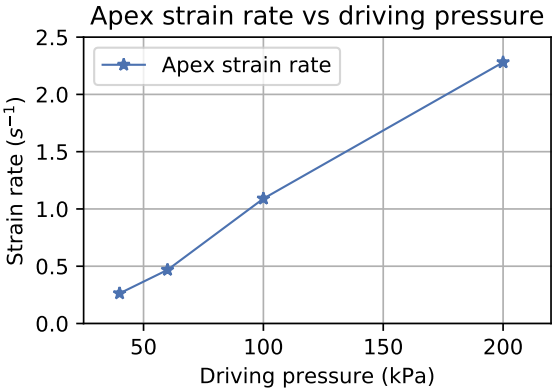

All other Mold Max 60 membranes burst at stretch ratios of over 1.6, with the initial crack starting near the apex. Examination of the high speed video showed that this membrane burst from the edges inwards, indicating a weak point in the membrane. It is possible that this weak point was caused by the same impact that caused the vibration at $65ms$, or by a casting defect.

7.3.6 Maximum strain rate tests

Only two maximum strain rate tests were conducted, both on circular, 50mm diameter, 2mm thick membranes using open vents and a 400g piston. The first test was conducted on a Mold Max 60 membrane with a driving pressure of 630kPa, and the second on a Dragon Skin 10 membrane with a driving pressure of 700kPa.

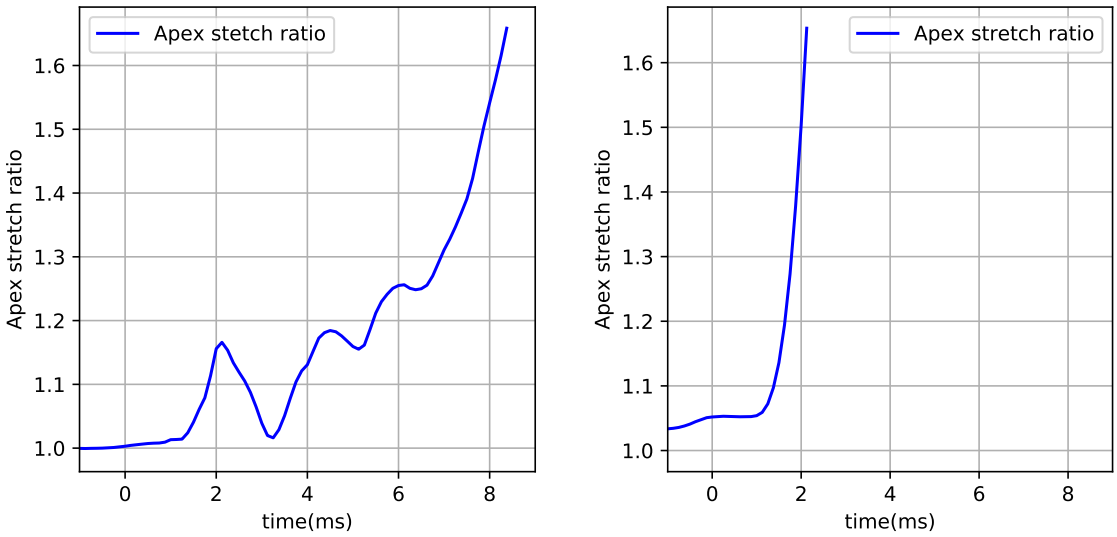

(a) Mold Max 60, 630kPa driving pressure **(b)** Dragon Skin 10, 700kPa driving pressure

Figure 7.13 Apex stretch ratio vs time for high strain rate tests. Note that fig. 7.13b ends when reliable correlation is lost, significantly before bursting occured

DIC correlation for most frames was lost early on in the test of the Dragon Skin 10 shown in fig. 7.13b due to heavy motion blur. The DIC software achieved correlation for some isolated frames

Table 7.9 *Strain rate for high strain rate bulge tests*

	Strain rate (s^{-1})	**Goodness of fit** (R^2)
Mold Max 60, 630 kPa	302	0.99
Dragon Skin 10, 700 kPa	827	0.97
Dragon Skin 10, 700kPa*	≈ 2500	–

later on in the test, implying an average strain rate of approximately $2000 - 3000s^{-1}$. As a result, two strain rates for this test are shown in table 7.9: one strain rate for early in the test when all frames had correlation, and one strain rate implied by the isolated frames captured later in the test. The second strain rate has a high degree of uncertainty associated with it, but shows that a very high average strain rate was achieved during the test. Very little can be said about the quality of this strain rate due to equipment limitations.

Note that the Dragon Skin 10 membrane bulges slightly prior to the beginning of the test. The central vents don't completely vent the pressure in the pump tube prior to the firing stage (particularly at higher piston velocities). This (combined with the very low stiffness of the Dragon Skin 10 membrane) results in a slight strain prior to the start of the test. This effect is not easily visible on the Mold Max 60 membrane due to significantly higher stiffness.

7.3.7 Membrane properties from inverse iteration scheme

Given the difficulties encountered with the inverse iteration scheme (further described in appendix D), only one membrane geometry (circular) and material (Mold Max 60) combination was modelled. The average membrane shown in fig. 7.6 was modelled, in order to minimise the effects of material variability. The material was modelled with two Ogden terms and 1 Maxwell damping term, for a total of 6 material parameters.

Picking initial estimate for material parameters

The elastic properties for Mold Max 60 extracted in section 7.1 were used for the initial estimate of the Ogden parameters. The strain hardening exponents were kept the same, but the shear moduli were decreased. This is because the tests in section 7.1 measured the instantaneous modulus at various strain rates[7], but the visco-elastic material model used the long term elastic moduli[8].

Updating of parameter estimate

The FE simulation was run using these initial estimated properties, and the L2 Norm of the error was calculated. Next the gradient of the error norm was numerically calculated with respect to each of the parameters, and a downhill optimisation scheme followed. Given the significant time cost of each update step, only one update step was undertaken [9]

Table 7.10 *Material parameters and associated error norm for parameter identification process.*

Iteration	Material parameters						Error norm	
	μ_1 (kPa)	μ_2 (kPa)	α_1	α_2	S_1	τ_1 (ms^{-1})	$\boldsymbol{L_2}$ (mm)	$\boldsymbol{L_1}$ (mm)
0	0.2	0.08	2.9	3.8	0.5	0.1	15.83	3.25
1	0.3	0.1	1.9	2.8	1	1	3.46	1.54

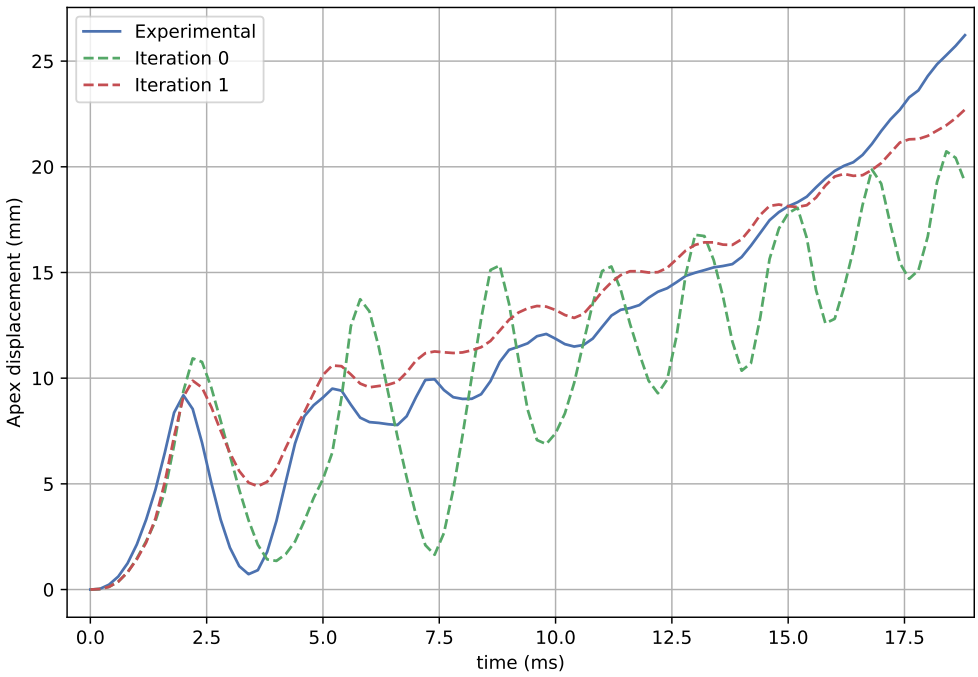

Figure 7.14 Experimental vs simulated apex displacement for parameter optimisation process.

Results

Figure 7.14 shows the simulated apex displacement for the parameter optimisation process, as well as the experimentally measured apex displacement. Table 7.10 shows the changing material parameters and associated error norms for the initial estimate and the first iteration. Note that the $\boldsymbol{L_2}$ norm decreased significantly faster than the $\boldsymbol{L_1}$ norm - this is unsurprising, as the $\boldsymbol{L_2}$ error norm was the parameter selected to be minimised.

As only one iteration was run, it is not possible to evaluate whether the result would converge fully. It is likely that more than one Maxwell term would be required in order to converge however. The updated parameters significantly improved the error from approximately 5ms onwards, but increased the error between 0 and 5ms - implying that at least two Maxwell terms are required in order to

[7] i.e. the sum of both viscous and elastic behaviour
[8] i.e. the elastic behaviour alone
[9] appendix D describes this in greater detail.

capture behaviour at different time scales. Additionally, there is likely to be damping due to the interaction between the membrane and the air - damping which was not included in the numerical model. It may well be necessary to model the membrane, piston and air in the pump tube in order to accurately capture the experimental behaviour.

Chapter 8

Conclusions and Recommendations

Contents

The apparatus performed successfully, as did the experimental methodology. High strain rate bulge tests with a high degree of repeatability were successfully conducted over a wide range of strain rates ($0.26 - 827s^{-1}$) for a wide range of materials. The achieved strain rate profile was superior to the strain rate profiles achieved for similar tests in the literature [34].

8.1 Evaluation of bulge test apparatus, methodology

8.1.1 Repeatability

As shown in table 7.5 and fig. 7.6, the pressure supply profile was highly repeatable at higher reservoir pressures, with minimal variance between repeated tests. At reservoir pressures below $150kPa$ the repeatability was not as good. This is to be expected, as the device was designed primarily for higher pressures and strain rates.

8.1.2 DIC measurement

The DIC measurement method performed well. Spatial resolutions were generally well below $0.09mm$(0.5 pixels), with worst case spatial resolutions of $0.27mm$(1.5 pixels) occurring in the frames immediately preceding loss of correlation.

Particularly at high strain rates, the DIC images occasionally suffered from motion blur. This could be solved via shorter shutter times, but would require more lighting or a wider aperture with the lenses used. Increasing the aperture was found to decrease depth of field unacceptably. Future tests may wish to either increase the lighting (doubling the lighting would halve the acceptable shutter time) or use lenses with a greater focal length.

8.1.3 Pressure measurement

The piezoelectric pressure sensor (Dytran 2300V3) used for these tests was able to adequately capture the pressure for the Mold Max 60 and textile reinforced silicone membranes, but had insufficient sensitivity to adequately capture the membrane pressure for the Dragon Skin 10 membranes.

If greater resolution is needed, the Dytran 2300V1 could be used instead, but this is not expected to be a problem. The Dragon Skin 10 membranes were far more pliable than the device was designed for. Future tests using this device are expected to focus on skin, which is significantly stiffer than Dragon Skin 10.

8.1.4 Strain:time profile

8.1.4.1 Variance from a constant strain rate

The first 5ms of each test were dominated by dynamic effects, leading to a variable strain rate in the initial portion of the test. The strain profile after this was significantly more linear, particularly for the Mold Max 60 membranes. Compared to high strain rate biaxial tests in the literature such as those of Bentil *et al* (2016)[34], a highly consistent strain rate was achieved. Figure 8.1 shows a comparison of a high strain rate test conducted as part of this dissertation, and a high rate test from the literature. Note that while the first 5 ms of fig. 8.1a are non-linear and dominated by dynamic effects, the entirety of fig. 8.1b is non-linear and dominated by dynamic effects.

8.1.4.2 Range of strain rates achieved

A wide range of strain rates was achieved, ranging from a minimum of approximately $0.26s^{-1}$ up to a maximum of approximately $2500s^{-1}$. The very low strain rate tests achieved low peak strains however, and the very high strain rate tests were poorly measured due to equipment limitations and motion blur. As a result, the very low and very high strain rate tests were not particularly useful. Tests at strain rates from $3.0s^{-1}$ up to $302s^{-1}$ were reliably conducted and captured by the DIC technique with a high degree of accuracy and repeatability. This is the useful range of strain rates achievable by the apparatus without resorting to equipment changes (the camera system in particular).

8.1.4.3 Range of strain ratios achieved

Varying the geometry of the clamp system allowed for the apex strain ratio to vary by a factor of approximately 2 (when using an elliptical boundary with a diameter ratio of 0.4). Higher apex strain ratios were expected based on preliminary calculations, but the strain ratio control was still successful.

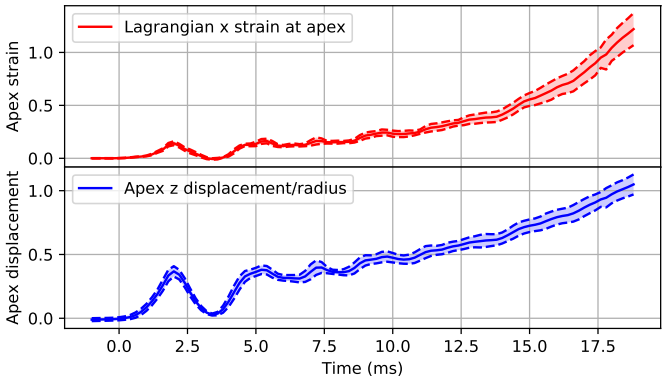

(a) Example of displacement and strain vs time for tests conducted

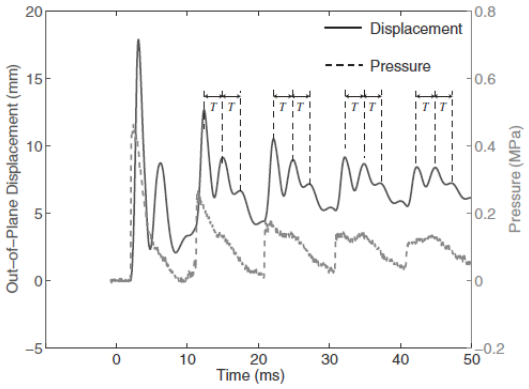

(b) Example of displacement profile for test conducted in the literature [34]

Figure 8.1 Comparison of displacement and strain profile for tests conducted in this dissertation (fig. 8.1a), compared to displacement profile for tests in the literature (fig. 8.1b). Note neither test achieves a constant gradient, but that fig. 8.1a is significantly closer to exhibiting a constant gradient than fig. 8.1b.

Table 8.1 *Range of strain rates achieved by the apparatus*

Strain rate (s^{-1})	$0.26 - 3.0$	$3.0 - 302$	$302 - 2500$
Adequately captured by DIC?	Yes	Yes	No
Useful range of strain achieved?	No	Yes	Yes

It should be noted that Jayyosi *et al* (2017) [36] conducted bulge tests with elliptical boundaries, and found that their apex strain ratios matched those predicted by the same preliminary calculations conducted in this work. Unlike this work, their tests were at low strain rates, which may explain the difference.

8.2 Evaluation of skin simulants used

8.2.1 Dragon Skin 10

The Dragon Skin 10 membranes served their purpose in that they allowed the DIC method to be validated at strains significantly higher than expected from skin.

Dragon Skin 10 is a poor skin simulant at high strains however, as it has lower shear moduli and strain hardening exponents than skin. Dragon Skin 10 is expected to be more useful as a skin simulant for tests at very low strains (where the collagen fibres have not straightened out yet, and elastin dominates).

8.2.2 Mold Max 60

The Mold Max 60 membranes performed as designed, exhibiting higher stiffness than most skin simulants used in the literature. This allowed the device to be validated for higher forces than expected when testing skin.

One major downside of the Mold Max 60 specimens was the complete lack of observable ductility. This caused any flaws in the specimens to cause premature fracture, greatly increasing variability across samples. Additionally, Mold Max 60 exhibits significantly lower strain hardening than skin ($alpha = 4vs9$), resulting in a very different pressure:strain profile.

8.2.3 Textile reinforced silicone

The textile reinforced silicone specimens performed as designed. They exhibited significant anisotropy, and strong strain stiffening behaviour.

8.2.3.1 Repeatability

These specimens were highly heterogeneous, exhibiting a high inter-specimen variability. This makes testing more challenging, but more closely emulates skin (which possesses far higher inter-specimen variability[1]). Making use of textile reinforcement from a more consistent source would likely reduce this variability.

8.2.3.2 Strain stiffening profile

The strain stiffening profile in the warp direction exhibited the same "J shaped curve" as skin, but transitioned to the linear region at a higher stretch ratio than skin.

The textile reinforced silicone exhibited negligible strain stiffening in the weft direction, showing quasi-linear-elastic behaviour.

The strain stiffening profile and degree of anisotropy could relatively easily be controlled by making use of two sets of warp fibres, laid down perpendicular to each other with varying density and crimp angle.

8.3 Evaluation of specimen fixation method, speckle method

8.3.0.1 Fixation method

The specimen fixation method performed well, removing the clamp induced initial deformation of the membrane associated with friction based clamp methods. Slipping at the membrane perimeter was eliminated for Dragon Skin 10 and Mold Max 60 membranes, and eliminated for most textile reinforced silicone membranes. Appendix G covers this in greater depth.

8.3.0.2 Speckle pattern

The speckle pattern performed as designed, allowing the DIC method to measure the membrane deformation field with a high degree of accuracy. Both speckle patterns (graphite based and silicone based) allow for far greater strains than the traditional spray paint based speckle pattern.

In addition to high strain rate testing of polymers, the silicone based speckle pattern shows promise for blast testing at high strains. Appendix E discusses this in greater detail. Both speckle pattern application methods are superior to the more common spray paint based approach commonly used in the literature.

8.4 Evaluation of material parameter extraction

The parameter extraction from the uniaxial tensile tests performed as expected, resulting in a model that closely followed experimental data.

Automated parameter extraction from the bulge tests was not successful, given difficulties with the LS-Opt software used. Manual parameter extraction appeared to be feasible, but only one iteration was undergone given the high time cost in semi-manually solving the optimisation problem.

8.5 Summary and recommendations for future work

In conclusion, the goals set out at the beginning of the project were met. The apparatus performed as designed, and achieved a wide range of strain rates on a wide range of skin simulant materials. The strain rate profile, specimen fixture method, and speckle pattern generation method in particular were a significant improvement on methods currently used in the literature. The device and methodology were validated on simulant materials, and can now be used for biological materials such as skin. The inverse iteration parameter extraction did not work as planned however, and did not give particularly useful results. The reasons for this are further covered in appendix D. Some comments on the scope of the project are made in appendix I

It is recommended that the following changes are made before the device is used for biological tissue:

8.5.1 Encapsulation of membrane

The current tests shielded the cameras from membrane fragments, but allowed the membrane fragments to enter the lab. In future it is suggested that the end of the device be contained in a perspex chamber in order to prevent biological tissue from entering the lab. Additionally, a small amount of negative pressure in this chamber would likely reduce the dynamic effects that dominated the initial 5ms of the test, as the membrane would not start the test in the flat position.

8.5.2 Parameter extraction

8.5.2.1 FEA based inverse iteration

Parameter extraction for the high strain rate bulge test was not successful. In future it is suggested that the FEA model of the experiment include the piston and the air in the pump tube, in order to more accurately capture the experimental effects.

8.5.2.2 Use of the Virtual Fields Method (VFM)

Given that the 3D DIC captures rich full-field spatial data about the experiment, it may well be more efficient to make use of VFM in order to extract material parameters from the test. Not only would VFM be less computationally expensive, it would give a spatial distribution of material properties across the membrane rather than simply the average material property.

References

[1] Theresa Koys Tonge, *Micro-Mechanical Approaches for the Heirarchical Modeling of SOft Biological Tissues*, Phd, Johns Hopkins University, 2014.

[2] Y. Lanir & Y. Fung, "Two-dimensional mechanical properties of rabbit skin—ii. experimental results", *Journal of Biomechanics*, vol. 7.

[3] R. Ogden, "Large deformation isotropic elasticity—on the correlation of theory and experiment for incompressible rubberlike solids", *Rubber Chemistry and Technology*, vol. 46.

[4] J. Weiss, B. Maker & S. Govindjee, "Finite element implementation of incompressible, transversely isotropic hyperelasticity", *Computer methods in applied mechanics and engineering*, vol. 135, (1996), pp. 107–128.

[5] S. Roth, J. Raul, B. Ludes & R. Willinger, "Finite element analysis of impact and shaking inflicted to a child", *International Journal of Legal Medicine*, vol. 121, (2007), pp. 223–228.

[6] K. Whittle, J. Kieser, I. Ichim, M. Swain, N. Waddell, V. Livingstone & M. Taylor, "The biomechanical modelling of non-ballistic skin wounding: blunt force injury", *Forensic Science, Medicine and Pathology*, vol. 4, (2007), pp. 33–39.

[7] G. Wilkes, I. Brown & R. Wildnauer, "The biomechanical properties of skin", *Critical Reviews in Bioengineering*.

[8] T. Sugihara, T. Ohura, K. Homma & H. Igawa, "The extensibility in human skin: variation according to age and site", *British Journal of Plastic surgery*, pp. 418–422.

[9] K. Langer, "On the anatomy and physiology of the skin", *The Imperial Academy of Science, Vienna*.

[10] M. Ridge & V. Wright, "The directional effects of skin. a bio-engineering study of skin with particular reference to langer's lines", *Journal of Investigative Dermatology*, vol. 46, (1966), pp. 341–346.

[11] C. Kraissl, "The selection of appropriate lines for elective surgical incisions", *Plastic and reconstructive surgery*.

[12] A.J. Gallagher, Aisling Annaidh, K. Bruyere, M. Ottenio, H. Xie & M.D. Gilchrist, "Dynamic tensile properties of human skin", *IRCOBI Conference 2012*.

[13] A. Ni Annaidh, K. Bruyere, M. Destrade, M. Gilchrist & M. Ottenio, "Characterization of the anisotropic mechanical properties of excised human skin", *Journal of the Mechanical Behaviour of Biomedical Materials*, vol. 5, (2012), pp. 139–148.

[14] W. Yang, V. Sherman, B. Gludovatz, E. Shraible, P. Stewart, R. Ritchie & M. Meyers, "On the tear resistance of skin", *Nature Communications*.

[15] C. Jacquemoud, K. Bruyere-Garnier & M. Coret, "Methodology to determine failure characteristics of planar soft tissues using a dynamic tensile test", *Journal of Biomechanics*, vol. 40, (2007), pp. 468–475.

[16] R. Rivlin, "Large elastic deformations of isotropic materials. iv. further developments of the general theory", *Philosophical Transactions Mathematical Physical and Engineering Sciences*, vol. 241.

[17] C. FLynn, A. Taberer & P. Nielsel, "Measuring the mechanical properties of human skin in vivo using 3d force-sensitive micro robot and finite element analysis", *Biomechanics and modeling mechanobiology*, vol. 10, (2011), pp. 27–38.

[18] Y. Fung & P. Tong, "The stress:strain relationship for the skin", *Journal of Biomechanics*, vol. 9, (1976), pp. 649–657.

[19] Y. Lanir, "A structural theory for the homogeneous biaxial stress-strain relationships in flat collagenous tissues", *Journal of Biomechanics*, vol. 12.

[20] T. Gasser, R. Ogden & G Holzapfel, "Hyperelastic modelling of arterial layers with distributed collagen fibre orientations", *Journal of The Royal Society Interface*, vol. 3.

[21] M. Puso & J. Weiss, "Finite element implementation of anisotropic quasi-linear viscoelasticity using a discrete spectrum approximation", *Journal of Biomedical Engineering*, vol. 1998, (1998), pp. 62–70.

[22] O. Shergold, N. Fleck & D. Radford, "The uniaxial stress versus strain response of pig skin and silicone rubber at low and high strain rates", *international Journal of Impact Engineering*, vol. 32, (2006), pp. 1384–1402.

[23] N. Karajan, D. Fressmann, T. Erhart & P. Schumacher, *Biomechanical Material Models in LS-DYNA*, LD-DYNA, 2013.

[24] J. Bischoff, E. Arruda & K. Grosh, "Finite element modeling of human skin using an isotropic, nonlinear elastic constitutive model", *Journal of Biomechanics*, vol. 33, (2000), pp. 645–652.

[25] M. Comninou & L. Yannas, "Dependence of stress-strain nonlinearity of connective tissue on the geometry of collagen fibres", *Journal of Biomechanics*, vol. 9, (1976), pp. 427–433.

[26] R. Groves, S. Coulman, J. Birchall & S. Evans, "An anisotropic, hyperelastic model for skin: Experimental measurements, finite element modelling and identification of parameters for human and murine skin", *Journal of the Mechanical Behaviour of Biomedical Materials*, pp. 167–180.

[27] Y. Lanir & Y. Fung, "Two-dimensional mechanical properties of rabbit skin—i. experimental system", *Journal of Biomechanics*, vol. 7.

[28] K. Billiar & M. Sacks, "Biaxial mechanical properties of the natural and glutaraldehyde treated aortic valve cusp—part i: Experimental results", *Journal of Biomechanical Engineering*, vol. 122.

[29] A. Skulborstad, S. Swartz & N. Goulbourne, "Biaxial mechanical characterization of bat wing skin", *Bioinspiration and Biomimetics*, vol. 10.

[30] A.J. Ranta-Eskola, "Use of the hydraulic bulge test in biaxial tensile testing", *International Journal of Mechanical Sciences*, vol. 21, (1979), pp. 457–465.

[31] J. Strikwerda & J. Considine, "Deformation of a membrane under uniform static pressure", .

[32] V. Grolleau, G. Gary & D. Mohr, "Biaxial testing of sheet materials at high strain rates using viscoelastic bars", *Experimental Mechanics*, vol. 48, (2007), p. 293.

[33] M. Ramezani & Z. Ripin, "Combined experimental and numerical analysis of bulge test at high strain rates using split hopkinson pressure bar apparatus", *Journal of Materials Processing Technology*, vol. 210, (2010), pp. 1061–1069.

[34] S. Bentil, K. Ramesh & T. Nguyen, "A dynamic inflation test for soft materials", *Experimental Mechanics*, vol. 56, (2016), pp. 759–769.

[35] J. Chakrabarty & J. Alexander, "Hydrostatic bulging of circular membranes", *Journal of strain analysis*, vol. 5, (1970), pp. 155–161.

[36] C. Jayyosi, K. Bruyere-Garnier & M. Coret, "Geometry of an inflated membrane in elliptic bulge tests: evaluation of an ellipsoid shape approximation by stereoscopic digital image correlation measurements", *HAL*.

[37] R. Curry, *Response of plates subjected to air-blast and buried explosions*, Phd, University of Cape Town, 2017.

[38] D. Einstein, P. Reinhall, M. Nicosia, R. Cochran & K. Kunzelman, "Dynamic finite element implementation of nonlinear, anisotropic hyperelastic biological membranes", *Computer Methods in Biomechanics and Biomedical Engineering*, vol. 6.

[39] N. Stander, W. Roux, A. Basudhar, T. Eggleston, T. Goei & K. Craig, *LS-OPT User's Manual: A design optimisation and probabilistic analysis tool for the engineering analyst*, Livermore Software Technology Corporation.

[40] J. Seng, *Inverse Modelling of Material Parameters for Rubber-like material: Create a New Methodology of Predicting the Material Parameters using Indentation Bending Test*, Phd, Liverpool John Moores University, 2015.

[41] M. Sutton, J. Orteu & H. Schreier, *Image Correlation for Shape, Motion and Deformation Measurements*, Springer, 2007.

[42] W. Peters & W. Ranson, "Digital imaging techniques in experimental stress analysis", *Optical Engineering*, vol. 21, (1982), pp. 427–431.

[43] M. Sutton, W. Wolters, W. Peters, W. Ranson & S. McNeill, "Determination of displacements using an improved digital correlation method", *Image and Vision Computing*, vol. 1, (1983), pp. 133–139.

[44] Dantec Dynamics, "Q-480 handheld dic for 'point and shoot' displacement and strain measurement", Online information Brochure, 2018, URL `https://www.dantecdynamics.com/q-480-handheld-dic-for-point-and-shoot-displacement-strain-measurement`, most recently accessed: June 2018.

[45] F. Devernay & O. Fauergas, "Computing differential properties of 3-d shapes from stereoscopic images without 3-d models", IEEE, 1994, pp. 208–213.

[46] Dantec Dynamics, "Measurement principles of (dic)", Online Information Brochure, 2018, URL https://www.dantecdynamics.com/measurement-principles-of-dic, most recently accessed: June 2018.

[47] H. Schreier, J. Braasch & M. Sutton, "Systematic errors in digital image correlation caused by intensity interpolation", *Optical Engineering*, vol. 11, (2000), pp. 2915–2921.

[48] J. Park, S. Yoon, T. Kwon & K. Park, "Assessment of speckle-pattern quality in digital image correlation based on gray intensity and speckle morphology", *Optics and Lasers in Engineering*.

[49] V. Aune, E. Fagerholt, K. Hauge, M. Langseth & T. Borvik, "Experimental study on the response of thin aluminium and steel plates subjected to airblast loading", *International Journal of Impact Engineering*.

[50] N. Long & D. Clark, "High speed cameras help digital image correlation show its strength", Online, URL https://www.phantomhighspeed.com/-/media/project/ameteksxa/visionresearch/documents/whitepapers/english/web/webdic.pdf?la=en, accessed June 2018.

[51] A. Sundaramurthy & N. Chandra, "A parametric approach to shape field-relevant blast wave profiles in compressed-gas-driven shock tube", *Frontiers in Neurology*, vol. 5.

[52] E. Arruda & M. Boyce, "A three dimensional constitutive model for the large stretch behaviour of rubber elastic materials", *Journal of the Mechanics and Physics of Solids*, vol. 41.

[53] G. Voyiadjis & P. Kattan, "On the theory of elastic undamageable materials", *Journal of Engineering Materials and Technology*, vol. 135.

[54] C. Buffinton, K. Tong, R. Blaho, E. Buffinton & D. Ebenstein, "Comparison of mechanical testing methods for biomaterials: Pipette aspiration, nanoindentation, and macroscale testing", *Journal of the Mechanical Behavior of Biomedical Materials*, vol. 51.

[55] L Sparks, N Vavalle, K Kasting, B Long, M Tanaka, P Sanger, K Schnell & T Conner-Kerr, "Use of silicone materials to simulate tissue biomechanics as related to deep tissue injury", *Advances in Skin and Wound Care*, vol. 28.

[56] Smooth-On Corporation, "Dragon skin series: Addition cure silicone rubber compounds data-sheet", Online, URL https://www.amtcomposites.co.za/sites/default/files/media/data-sheets/Dragon_Skin.pdf.

[57] Smooth-On Corporation, "Silicone thinner: Silicone rubber thinning fluid data-sheet", Online, URL https://www.amtcomposites.co.za/sites/default/files/media/data-sheets/Silicone_Thinner.pdf.

[58] Smooth-On Corporation, "Silc pig pigments: For tin and platinum silicone rubbers", Online, URL https://www.amtcomposites.co.za/sites/default/files/media/data-sheets/Silc_Pig_Pigments.pdf.

[59] Smooth-On Corporation, "Mold max 60: High heat resistant silicone rubber compound", Online, URL https://www.amtcomposites.co.za/sites/default/files/media/data-sheets/MOLD_MAX_60.pdf.

[60] C. McCarthy, M. Hussey & M. Gilchrist, "On the sharpness of straight edge blades in cutting soft solids: Part i – indentation experiments", *Engineering Fracture Mechanics*, vol. 74.

[61] W. Press & S. Teukolsky, "Savitzky-golay smoothing filters", *Computers in Physics*, vol. 4, (1990), pp. 669–672.

[62] A. Savitzky & M. Golay, "Smoothing and differentiation of data by simplified least squares procedures.", *Analytical Chemistry*, vol. 36, (1964), pp. 1627–1639.

[63] ASTM subcommittee D11.10, *D412-16 Standard Test Methods for Vulcanized Rubber and Thermoplastic Elastomers–Tension*, American Society for Testing and Materials.

[64] A. Spiess & N. Neumeyer, "An evaluation of r^2 as an inadequate measure for nonlinear models in pharmacological and biochemical research: a monte carlo approach", *BMC Pharmacology*, vol. 10.

[65] P. Wriggers, *Nonlinear Finite Element Methods*.

Appendices

Appendix A

Spherical Bulge Derivations

If more detailed material models for large scale deformations are required, hyperelastic strain energy functions are needed. Rewriting the the equations in section 2.5.3.1 in continuum notation (and retaining the spherical deformation assumption), the deformation gradient at the apex will be:

$$\boldsymbol{F}_{apex} = \begin{bmatrix} \frac{R\theta}{r} & 0 & 0 \\ 0 & \frac{R\theta}{r} & 0 \\ 0 & 0 & \frac{t}{t_0} \end{bmatrix} = \begin{bmatrix} \frac{(h^2+r^2)}{2hr} sin^{-1}\left(\frac{2rh}{h^2+r^2}\right) & 0 & \\ 0 & \frac{(h^2+r^2)}{2hr} sin^{-1}\left(\frac{2rh}{h^2+r^2}\right) & 0 \\ 0 & 0 & \frac{t}{t_0} \end{bmatrix} = \begin{bmatrix} \lambda_1 & 0 & 0 \\ 0 & \lambda_2 & 0 \\ 0 & 0 & \lambda_3 \end{bmatrix} \tag{A.1}$$

If the material in question is incompressible, the volume ratio J will be 1.

$$J = 1 = det(\boldsymbol{F}) = \left(\frac{R\theta}{r}\right)^2 \frac{t}{t_0} \tag{A.2}$$

Rearranging:

$$t = t_0 * \left(\frac{r}{R\theta}\right)^2 \tag{A.3}$$

Applying the thin walled sphere assumption, and assuming that radial (z) stress is negligible, the Cauchy stress tensor $\mathbf{T}$ due to geometry (curvature) and pressure will be:

$$\boldsymbol{T} = \begin{bmatrix} \frac{PR}{t} & 0 & 0 \\ 0 & \frac{PR}{t} & 0 \\ 0 & 0 & 0 \end{bmatrix} = \frac{P(h^2+r^2)^3 (sin^{-1}(\frac{2hr}{h^2+r^2}))^2}{8t_0 r^2 h^3} \begin{bmatrix} 1 & 0 & 0 \\ 0 & 1 & 0 \\ 0 & 0 & 0 \end{bmatrix} \tag{A.4}$$

For a given strain energy density function $\boldsymbol{\Psi}$, the Cauchy stress is:

$$\boldsymbol{T} = \frac{2}{J}\boldsymbol{F} \cdot \frac{\partial \boldsymbol{\Psi}}{\partial \boldsymbol{B}} \cdot \boldsymbol{F}^T \tag{A.5}$$

In the case of an isotropic material, the above simplifies to:

$$\boldsymbol{T} = \frac{2}{J}\boldsymbol{B} \cdot \frac{\partial \boldsymbol{\Psi}}{\partial \boldsymbol{B}} \tag{A.6}$$

The Cauchy stress tensor for an isotropic incompressible Ogden material is given in terms of the principal stretches by:

$$\boldsymbol{T}_{Ogden^{inc}} = 2\boldsymbol{B}\cdot\frac{\partial\boldsymbol{\Psi}}{\partial\boldsymbol{B}} + p\boldsymbol{I} = 2\begin{bmatrix}\lambda_1^2 & 0 & 0\\ 0 & \lambda_2^2 & 0\\ 0 & 0 & \lambda_3^2\end{bmatrix}\cdot\begin{bmatrix}\frac{\partial\Psi}{\partial\boldsymbol{B}_{11}} & 0 & 0\\ 0 & \frac{\partial\Psi}{\partial\boldsymbol{B}_{22}} & 0\\ 0 & 0 & \frac{\partial\Psi}{\partial\boldsymbol{B}_{33}}\end{bmatrix} - p\boldsymbol{I} \tag{A.7}$$

Where $\frac{\partial\boldsymbol{\Psi}}{\partial\boldsymbol{B}_{ii}}$ is given by:

$$\frac{\partial\boldsymbol{\Psi}}{\partial\boldsymbol{B}_{ii}} = \sum_{p=1}^{N}\frac{\mu_p}{2}\lambda_i^{\alpha_p-2} \tag{A.8}$$

This evaluates to:

$$\boldsymbol{T}_{Ogden^{inc}} = -p\boldsymbol{I} + \sum_{p=1}^{N}\mu_p\begin{bmatrix}\lambda_1^{\alpha_p} & 0 & 0\\ 0 & \lambda_2^{\alpha_p} & 0\\ 0 & 0 & \lambda_3^{\alpha_p}\end{bmatrix} = -p\boldsymbol{I} + \sum_{p=1}^{N}\mu_p\begin{bmatrix}\lambda_1^{\alpha_p} & 0 & 0\\ 0 & \lambda_2^{\alpha_p} & 0\\ 0 & 0 & \left(\frac{1}{\lambda_1\lambda_2}\right)^{\alpha_p}\end{bmatrix} \tag{A.9}$$

Equating the stress distribution due to internal pressure and geometry (eq. (A.4)) with the stress distribution due to the deformation of the membrane (eq. (A.9)) results in:

$$-p\boldsymbol{I} + \sum_{p=1}^{N}\mu_p\begin{bmatrix}\lambda_1^{\alpha_p} & 0 & 0\\ 0 & \lambda_2^{\alpha_p} & 0\\ 0 & 0 & \left(\frac{1}{\lambda_1\lambda_2}\right)^{\alpha_p}\end{bmatrix} = \frac{P(h^2+r^2)^3(sin^{-1}(\frac{2hr}{h^2+r^2}))^2}{8t_0r^2h^3}\begin{bmatrix}1 & 0 & 0\\ 0 & 1 & 0\\ 0 & 0 & 0\end{bmatrix} \tag{A.10}$$

Given that $\lambda_1 = \lambda_2$, and that $\boldsymbol{T}_{33} = 0$, the hydrostatic pressure p can be solved for:

$$p = \sum_{p=1}^{N}\mu_p\lambda_1^{-2\alpha_p} \tag{A.11}$$

$$\therefore \boldsymbol{T}_{11} = \boldsymbol{T}_{22} = \sum_{p=1}^{N}\mu_p\left(\lambda_1^{\alpha_p} - \lambda_1^{-2\alpha_p}\right) = \frac{P(h^2+r^2)^3(sin^{-1}(\frac{2hr}{h^2+r^2}))^2}{8t_0r^2h^3} \tag{A.12}$$

In terms of h, r, t_0 and P:

$$\sum_{p=1}^{N}\mu_p\left(\frac{(h^2+r^2)sin^{-1}(\frac{2hr}{h^2+r^2})}{2hr}\right)^{\alpha_p} - \sum_{p=1}^{N}\mu_p\left(\frac{(h^2+r^2)sin^{-1}(\frac{2hr}{h^2+r^2})}{2hr}\right)^{-2\alpha_p} = \frac{P(h^2+r^2)^3(sin^{-1}(\frac{2hr}{h^2+r^2}))^2}{8t_0r^2h^3} \tag{A.13}$$

This allows for one to model the relation between driving pressure and bulge height for an incompressible Ogden material membrane of a given radius and initial thickness. From the bulge height, various other parameters of interest can be derived, such as the principle stretch ratios $(\lambda_1, \lambda_2, \lambda_3)$ and hence stresses.

Appendix B

Failed Skin simulants

B.1 3D printed sinusoidal collagen simulant

3D printed sinusoidal fibres were embedded in a silicone matrix in an attempt to emulate the behaviour of (sinusoidal) collagen fibres in an elastin matrix.

The available 3D printers used either ABS or PLA, so ABS was selected as the fibre material. Due to limitations on resolution of the 3D printer (an Ultimaker 2+ with a 0.2mm nozzle), each sine wave had a square cross section of 0.5mm, a period of 10mm and an amplitude of 1 mm. These were printed in bulk sheets, repeating every 2mm. Two layers of collagen simulant were embedded in a 2mm thick layer of *Dragon Skin 10* silicone in order to manufacture each membrane. Both layers were aligned the same way, in order to cause anisotropic membrane behaviour.

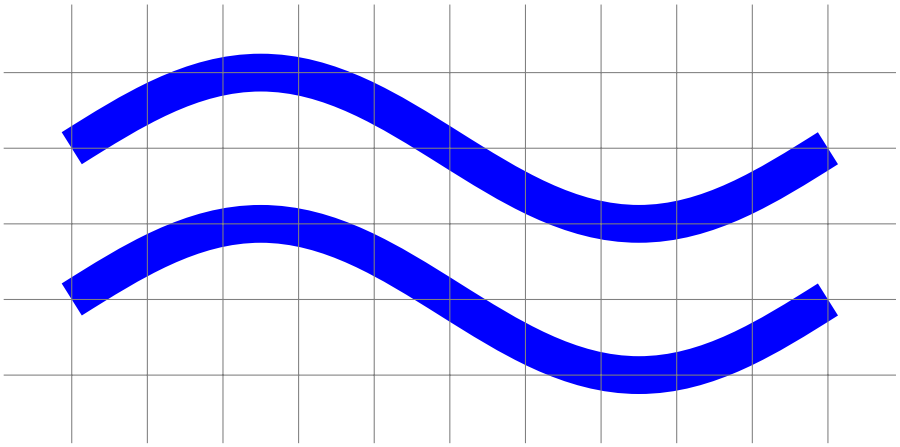

Figure B.1 To scale (1cm=1mm) figure of repeating unit of 3D printed collagen simulant. Each grid block represents 1mm

In addition to the bulk sheets of sinusoidal beams, several tensile dogbone specimens were printed in order to test real world behaviour against numerically expected behaviour.

B.1.1 Fibre:matrix bond

The 3D printed ABS did not bond to the silicone matrix at all, leading to significant delamination at strains of approximately 10%. This was clearly not a suitable skin simulant.

B.1.2 Uniaxial behaviour of collagen simulant

Uniaxial tensile specimens were tested in order to compare behaviour to the theoretically expected behaviour of a sinusoidal elastica beam.

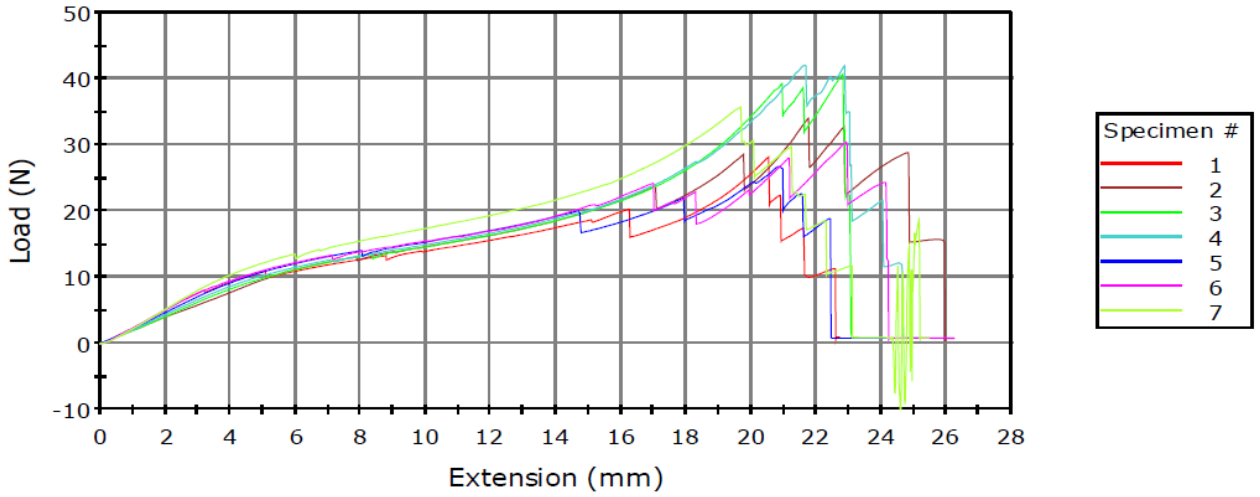

Figure B.2 Force:Extension results for 70mm gauge section 3D printed collagen simulant

Micro-cracks appeared in the 3D printed specimens at approximately 4mm extension, resulting in the flattening of the force curve from 4mm to 16mm. By 20mm extension the sinusoidal fibres had almost entirely straightened, but they then began to fracture.

This behaviour is not entirely unexpected, given the notoriously poor mechanical properties exhibited by most 3D printed parts.

B.1.3 Suitability of simulant

This simulant was found to be entirely unsuitable due to the lack of bonding between the fibres and the matrix as well as the poor mechanical properties of the fibres. This work led directly to the textile reinforced skin simulant, which was far more successful.

If skin simulants of this type are explored in future, it is recommended that the fibres be cast from high stiffness silicone (such as Mold Max 60), and embedded in a matrix of low stiffness silicone such as Dragon Skin 10. Using an elastomer for the fibres would prevent the early onset micro-cracking and plasticity exhibited by the ABS. The moulds for the fibres could easily be 3D printed, and this would allow for a wide range of fibre crimp angles to be explored.

B.2 Mold Star 15

Mold Star 15 silicone was initially experimented with instead of *Dragon Skin 10* as it was opaque[1] (obviating the need for silicone pigment) and slightly stiffer than *Dragon Skin 10*. This silicone was not used however, as parts A and B had a very short shelf life, resulting in highly variable material properties between each batch.

[1]Figure 4.3 shows a *Mold Star 15* sample, which is opaque and bright teal

Appendix C

Selected Design calculations

A conservative yield strength of $220MPa$ was assumed for all steel parts. In reality, most parts will have a significantly higher yield strength.

C.1 Pressurisation

The mid-flange was connected to the rear flange with 12 M10 bolts, and compressed onto the reservoir tube. The tie rods holding the reservoir together were mild steel bolts, with a lower tensile area than the reservoir tube ($696mm^2$ vs $1709mm^2$). The tie rods were torqued to 12.5 Nm (nominally $6.25kN$ per bolt), resulting in a total axial clamp force of $75kN$. Note that the bolt torque:bolt tension relationship has significant uncertainty. The bolt torque upper and lower limits were nominally $25Nm$ and $3.3Nm$.

C.1.1 Joint separation

Joint separation - elastic The preload force was $75kN$, and the joint stiffness ratio C was 0.289. The joint separation force is given by:

$$F_{sep} = \frac{F_{PL}}{1-C} = \frac{75kN}{1-0.289} = 105.5kN \tag{C.1}$$

The pressure (in MPa) required to cause joint separation is[1]:

$$P_{sep} = \frac{F_{sep}}{A_{flange}} = \frac{105.5kN}{\pi(66^2-30^2)} = 9.72MPa = 97bar \tag{C.2}$$

This shows that the reservoir will leak due to elastic joint separation before the bolts enter the plastic regime. Note that the O-ring seals on the piston are rated for 60 bar, so leaking past the piston would occur before joint separation.

[1]Note that these calculations ignore the effects of Poisson's ratio. The hoop stress and Poisson's ratio will cause the reservoir to shorten slightly, reducing clamp force. It was found that including this effect in calculations made a negligible difference, particularly as the joint stiffness ratio was so low. If the joint stiffness ratio was significantly higher, this effect would have to be considered. Ignoring the effect of Poisson's ratio increases the calculated elastic joint separation pressure.

Joint separation - plastic Assuming pressurisation continues after elastic joint separation, the pressure (in MPa) required to cause yielding in the tie rods is:

$$P_{Yield} = \frac{S_y A_{bolts}}{A_{flange}} = \frac{220 \times 696}{10857} = 14.1MPa = 141bar \tag{C.3}$$

This meant that in the event of the device being over-pressurised, the tie rods would stretch and then start to yield while the (original) reservoir was still in the elastic regime. Once the bolts started to stretch, compression between the flanges and the reservoir would be lost and significant leaks would occur. This would result in a "safe" failure mode (loss of reservoir pressure), rather than a catastrophic failure mode.
Inducing a catastrophic failure due to pressure would require overtorquing the tie rods well into the plastic regime (inducing necking), and then pressurising the reservoir.

C.1.2 Plastic failure of reservoir

The originally specified reservoir was replaced with a lower thickness reservoir due to difficulty obtaining materials. Shown below are calculations for the revised reservoir thickness.

C.1.2.1 Replacement reservoir

The replacement reservoir had a wall thickness of $4.5mm$ (rounded down to $4mm$), and an internal diameter of $132mm$. The hoop stress due to internal pressure is therefore $\sigma_h = \frac{Pr}{t} = 16.5 \times P$. The axial compressive force is given by $F_a = -F_{PL} + (1 - C)F_{app}$. Prior to joint separation, the axial stress in the reservoir is therefore:

$$\sigma_a = \frac{-75kN}{1709mm^2} + 0.711\frac{P \times 10857mm^2}{1709mm^2} = -43.9MPa + P \times 4.52 \tag{C.4}$$

The von-Mises equivalent stress (in MPa) in terms of pressure (in MPa) is:

$$\sigma_{vM} = \sqrt{\frac{1}{2}} \times \sqrt{(16.5P - 43.9 + 4.52P)^2 + (-43.9 + 4.52P)^2 + (16.5P)^2} \tag{C.5}$$

Assuming a conservative yield stress of $220MPa$ for the steel of the reservoir, an internal pressure of $7.06MPa \approx 70bar$ is required in order to cause yielding in the reservoir walls.

C.1.2.2 Piston containment

In the event of a "dry firing", the piston will hit the membrane fixture at high speed. It is important that the piston remain contained within the device even in the event of a failure. Should the piston hit the membrane fixture at high speed, the energy will be transferred into the 6 M12 tie rods bolting the membrane fixture to the central flange.
These bolts are preloaded to $3Nm$, equivalent to $1.25kN$ of preload per bolt. Assuming that the mild steel bolts yield at 220 MPa, it will take $18.5kN$ per bolt to induce plasticity (i.e. $111kN$ in total). The energy taken to do this is given by $\frac{1}{2}K(d_1^2 - d_0^2)$. The stiffness is:

$$k_{total} = \left[\left(\frac{6 \times 84.3 \times 200 \times 10^3}{0.85}\right)^{-1} + \left(\frac{12 \times 58 \times 200 \times 10^3}{0.6}\right)^{-1}\right]^{-1} = 78.66kN/mm \tag{C.6}$$

The energy taken to load the bolts with $111kN$:

$$E_{yield} = 0.5\frac{F_1^2 - F_{preload}^2}{K_{total}} = 0.5\frac{12.26 \times 10^9}{78.66 \times 10^6} = 78J \tag{C.7}$$

This shows that a relatively small amount of energy is required to induce plasticity in the tie rods if the piston is allowed to directly impact the clamp fixture.

Appendix D

LS Opt failed parameter extraction

D.1 Entering parameters

D.1.1 Graphical interface

When entering material properties in LS Dyna, there are two graphical input methods: input to a text box, and adding to a list. This is shown in fig. D.1, where text box properties are surrounded by a green box, and list type properties are surrounded by a red box.

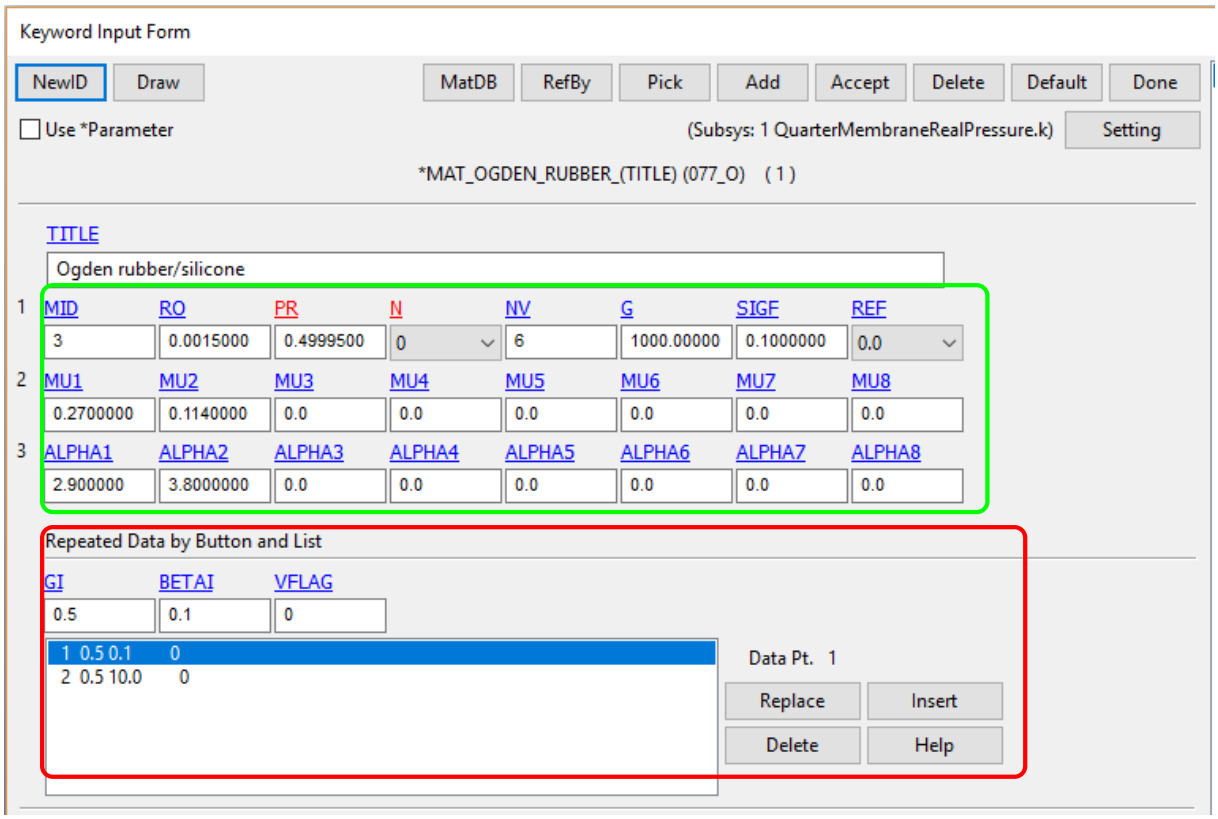

Figure D.1 Material property input window for Ogden Rubber in LS Dyna. Text box properties are shown in the green section, and list type properties are shown in the red section

Entering parameters (variables) as material properties in text boxes works well, but entering parameters as material properties in lists does not work. Unfortunately the viscous damping properties are input as a list, and the viscous damping properties are the material properties that are unknown.

D.1.2 Direct editing of K file

LS Dyna stores FEA simulations as human readable text (.k) files, and these files can be directly edited in a text editor such as Notepad++. Inputting parameters as text box type material properties via direct editing of the k file worked, but the k file was corrupted when this same process was followed for list type data. This implies that there is an intrinsic difference between these two data-types beyond the input method.

D.2 Attempted work-arounds

After consulting other LS-Dyna users on the LS-Dyna usergroup, and Richard Curry (whose PhD involved heavy use of LS Dyna and LS Opt), no direct solution to the problem was found. Instead, various workarounds were attempted. Many of these workarounds were promising, but were rapidly moving outside of the scope of the project.

D.2.1 Use of a different material model

Other materials in LS-Dyna include viscous damping effects, and input viscous properties in text boxes rather than lists. Unfortunately, none of these materials adequately capture the hyper-elastic behaviour of the silicone.

Modelling the visco-elastic membrane as two co-incident membranes (one which captures viscous effects only and one which captures elastic effects only) was considered, but this would be questionably accurate.

Writing a custom material model into LS Dyna would allow for all material properties to be entered into text boxes, but this was far outside the scope of the project.

Appendix E

Speckle pattern suitability for blast loading

The silicone based speckle method is well suited to generating a speckle pattern on a silicone surface, but it was not clear if it would be suitable for blast loaded plates. Aune *et al* (2015) [49] found that spray paint tended to flake off plates undergoing high strains during blast events; the author was curious about the suitability of the silicone speckle method. Whilst silicone is capable of undergoing high strains before breaking, it was not clear if it would adhere to the plates or simply spall off under the harsh conditions of a blast wave.

E.1 Specimen preparation

BISRU Labs were already blast testing thin steel plates as part of an unrelated project. One of these plates was sanded and then cleaned with acetone before having a silicone based speckle pattern applied. This plate was then loaded onto the blast pendulum and underwent an airblast which caused significant local deformation.

E.2 Results

No observable spalling of the silicone was observed, and all silicone speckles appeared to have remained in contact with the blast plate. This result is promising, and warrants further investigation - particularly on thin aluminium plates undergoing airblast events.

Appendix F

1D model of closed ended cylinder and free piston

A closed ended cylinder pressurised by a free piston of a given mass was modelled using a 1D Lagrangian approach. This CFD model was simple, and modelled each element as a 0^{th} order inviscid, compressible volume of air undergoing isentropic compression. Each time-step was incremented using a forward Euler approach (i.e. explicit, second order)

F.1 Lagrangian vs Eulerian approach

Most CFD codes use an Eulerian approach to model the fluid. A Lagrangian approach was used for two reasons: automatic spatial refinement, and lack of an upwinding term.

F.1.1 Automatic mesh refinement

At the beginning of the compression cycle, the mesh can be fairly coarse. Pressures, temperatures, and densities are relatively low, and there are few sharp gradients. Near the end of the compression cycle, the mesh needs to be significantly finer: pressures, temperatures, and densities are a lot higher, and spatial gradients are a lot sharper.

With an Eulerian approach, this requires that the elements next to the piston are coarse, with mesh refinement increasing as the elements get further from the piston starting position and closer to the end of the tube. The elements do not move, and the piston leaves elements behind as it compresses the gas.

With a Lagrangian approach, the elements move with the piston, and the mesh is automatically refined as compression increases. No elements are left behind, and all elements are part of the simulation for the entire stroke of the piston.

F.1.2 Upwinding term

For a given quantity ϕ contained in a reference volume V at time t, the time derivative of ϕ is given by the Reynolds Transport Theorem:

$$\frac{D}{Dt}\int\limits_{V(t)} \phi dV = \int\limits_{V(t)} \frac{\partial \phi}{\partial t} + (\nabla \cdot \phi)\, dV \tag{F.1}$$

As a result, the momentum conservation term of the Navier-Stokes equation is significantly simpler in the Lagrangian description:

$$\underbrace{\int_{V(t)} \frac{D(\rho \boldsymbol{u})}{Dt} dV}_{Lagrangian} = \underbrace{\int_{V(t)} \frac{\partial(\rho \boldsymbol{u})}{\partial t} + \nabla \cdot (\rho \boldsymbol{u} \otimes \boldsymbol{u})\, dV}_{Eulerian} \tag{F.2}$$

F.2 Geometric and material model

The fluid was modelled as an inviscid, ideal gas. Shock dynamic effects were ignored, and each node had only 3 material properties: mass, pressure, specific heat ratio ($\frac{C_p}{C_v} \approx 1.4$ for air). Each node had two spatial properties: position and velocity.

The tube was modelled as a uniform, 1D cylinder, and the piston was modelled as a 1D particle with mass, velocity and position properties. In reality there is a constriction in the cylinder near the clamp fixture, but this was ignored.

F.3 Suitability of model

It was initially assumed that this numerical model was too crude, and shock dynamic effects of gas would have to be included in the calculations. However, this numerical model showed a similar pressure profile to the experimentally measured pressure profile. As a result, it was not worth writing higher fidelity code. This code had served its purpose of confirming that the measured oscillations in pressure were not spurious, and had a simple physical explanation.

Appendix G

Clamp method evaluation

G.0.1 Quality of boundary conditions

The clamp method worked well for the Mold Max 60 and the Dragon Skin 10 membranes, but less well for the textile reinforced silicone membranes.

G.0.1.1 Mold Max 60, Dragon Skin 10

No delamination at the boundaries was observed when examining post-test pure silicone membranes. Additionally, no boundary slippage was visible when examining the high speed video footage of tests. This indicates that the clamp method worked as designed, and provided a consistent no-slip boundary condition for the pure silicone membranes.

G.0.1.2 Textile reinforced silicone

Rather than bursting, some of the textile reinforced silicone membranes delaminated from the Masonite clamp ring. This is likely due to the low shear strength of the bond (pure Dragon Skin 10 silicone) relative to the textile reinforced membrane's bulk material.

This could be solved by "sewing" the textile membrane to the Masonite clamp ring, or changing the clamp geometry to make use of capstan friction. These clamp methods have been used for planar tension tests of skin [27] and to clamp drum membranes respectively.

This delamination is not a significant issue however, as the textile reinforced silicone is only intended as a skin simulant. When testing skin, a different clamp method will have to be used given that skin isn't castable.

G.0.2 Membrane seal

The membrane clamp method provided an excellent seal for Dragon Skin 10 membranes. The quality of the seal for Mold Max 60 and textile reinforced silicone membranes is less clear.

G.0.2.1 Dragon Skin 10

During low strain rate tests of Dragon Skin 10, the membrane didn't burst, and the piston didn't rebound (due to friction and low pressures). This resulted in an inflated "balloon" of Dragon Skin

10, a picture of which is shown in fig. G.1. This image was taken approximately 2 minutes after the bulge test took place, indicating that the membrane clamp had negligible leaks. A pressure reading was not taken due to limitations on the pressure sensor [1] and recording equipment[2].

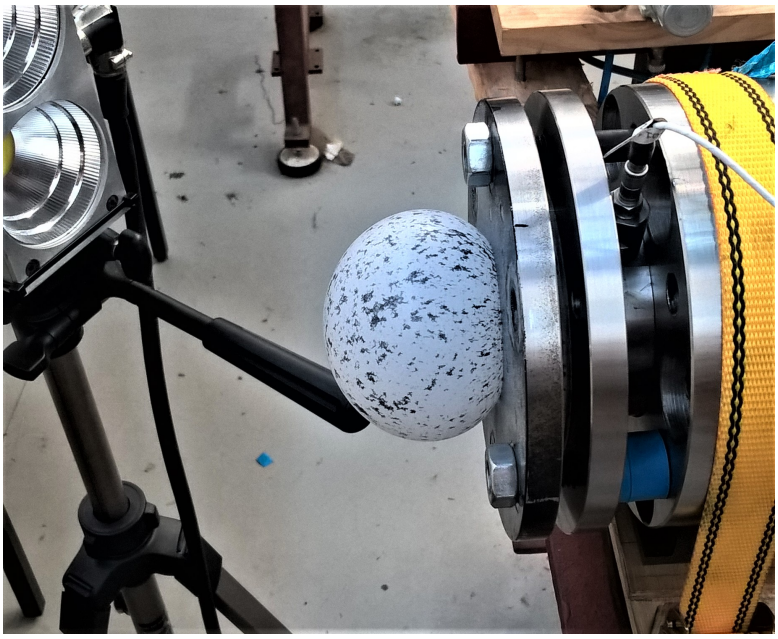

Figure G.1 Dragon Skin 10 membrane approximately 2 minutes after low strain rate test. Balloon diameter is approximately $100 - 150mm$.

G.0.2.2 Mold Max 60, Textile reinforced silicone

Due to the high stiffness and low extension at break [3] experienced by the Mold Max 60 and textile reinforced silicone membranes, "balloon" behaviour was not observed. This made it difficult to directly observe the quality of the seal for these membranes.

It is expected that the seal for the textile reinforced membranes is of similar quality to the Dragon Skin 10 membranes, as the contact surfaces are identical. No reinforcing fibres are exposed to the surface of the membranes.

The Mold Max 60 membrane seal is likely to be of worse quality than the Dragon Skin 10 seal, as the Mold Max 60 membranes are less pliant. This makes them less able to fill any voids or leak paths. Any minor leaks are not expected to have a significant impact on results, given the short duration of the test events.

[1] The piezoelectric sensor was not able to reliably take pressure readings of events with a frequency of $5s$.

[2] The Picoscope used to record the pressure was only capable of taking 78125 samples. This limited the possible recording duration, if the bulge event itself was to be recorded with a sufficient sampling frequency.

[3] Relative to Dragon Skin 10

Appendix H

Engineering Drawings

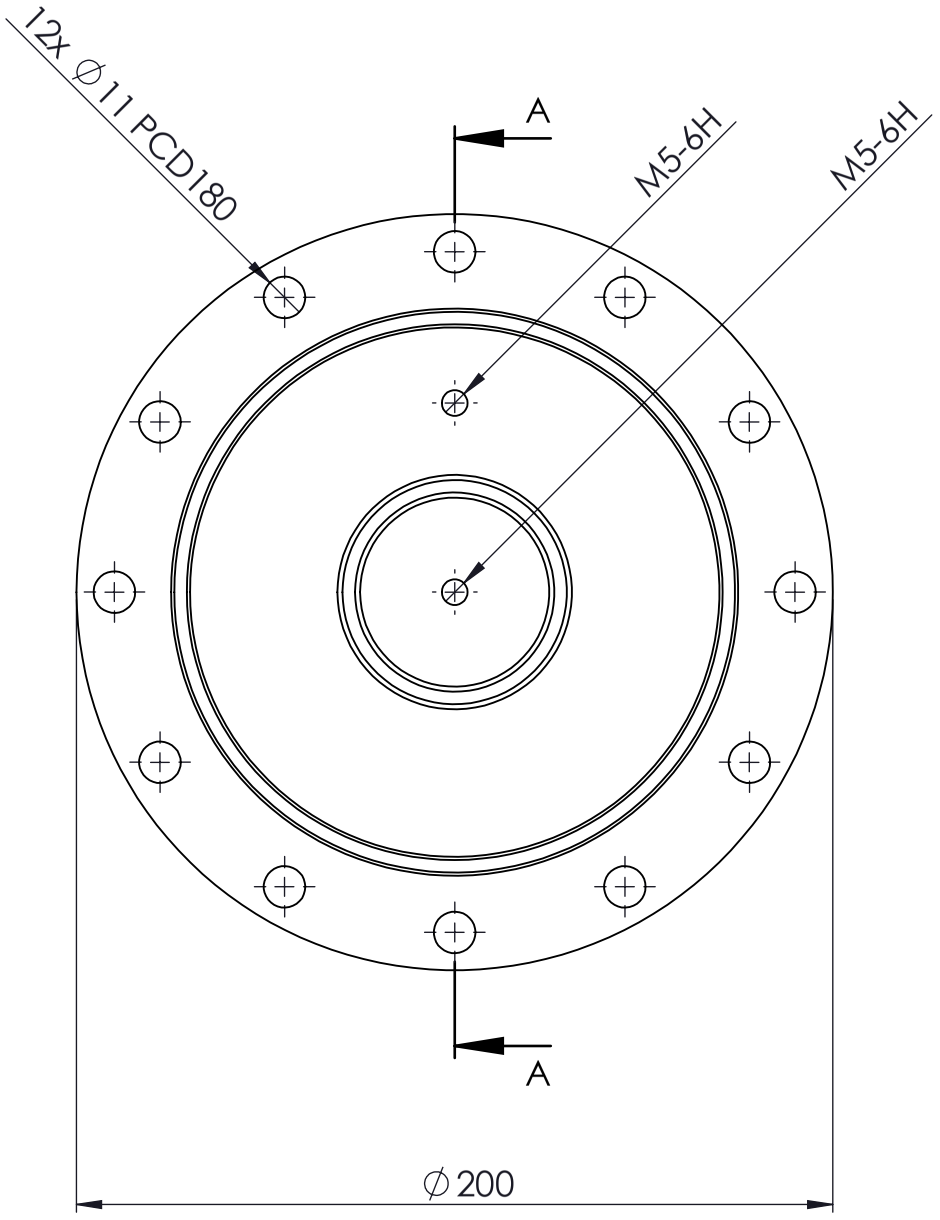

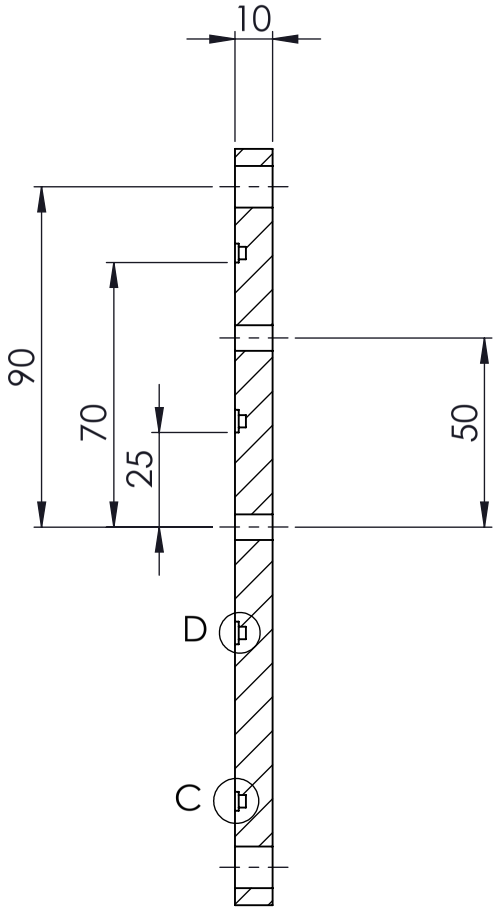

SECTION A-A
SCALE 1 : 2

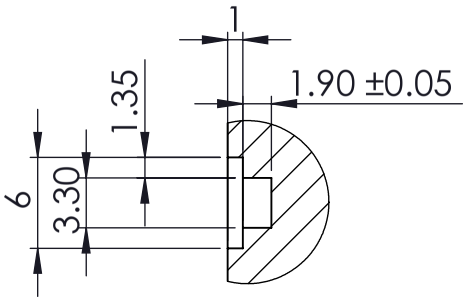

DETAIL D
SCALE 2 : 1

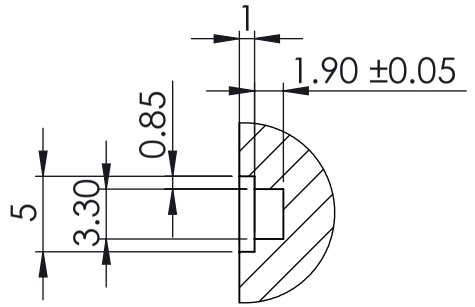

DETAIL C
SCALE 2 : 1

A4 Landscape	University of Cape Town Department of Mechanical Engineering				
	Title: EndCap				
Quantity: 1	Part Finish	Date: 09/04/2018	Scale: 1:5	EndCap	of 15
Material: Mild Steel	Drawn By: GRHAAR001			Drawing Number 2	

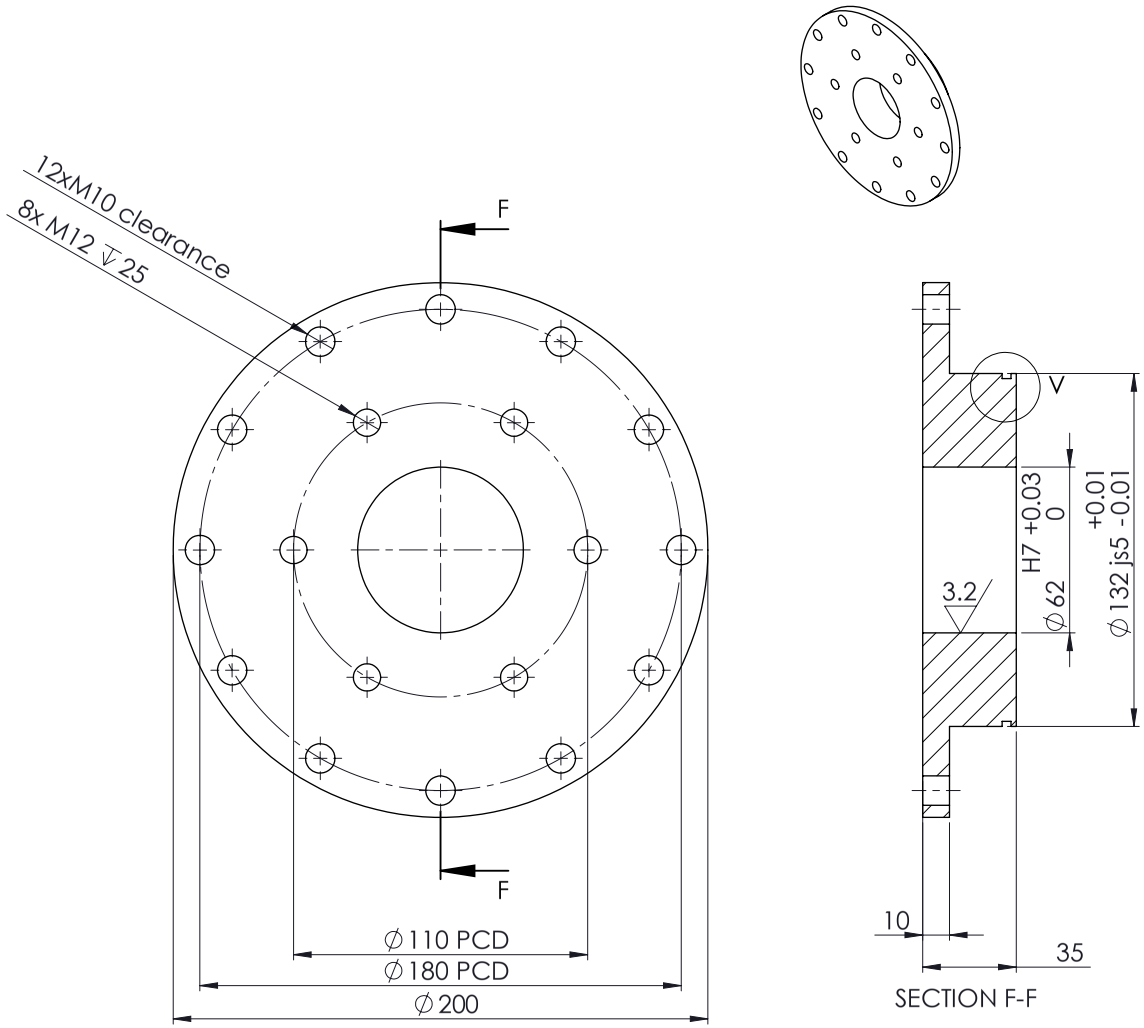

SECTION F-F

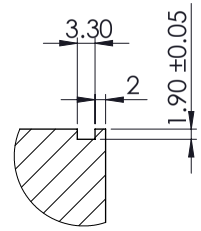

DETAIL V
SCALE 1 : 1

SOLIDWORKS Educational Product. For Instructional Use Only

A3 Landscape	University of Cape Town Department of Mechanical Engineering				
	Title: Mid Flange				
Quantity: 1	Part Finish	Date: 09/04/2018	Scale: 1:2	MidCap	of 15
Material: Mild Steel	Drawn By: GRHAAR001			Drawing Number 3	

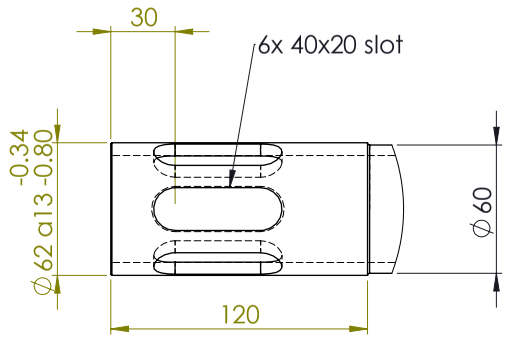

DETAIL J
SCALE 2 : 5

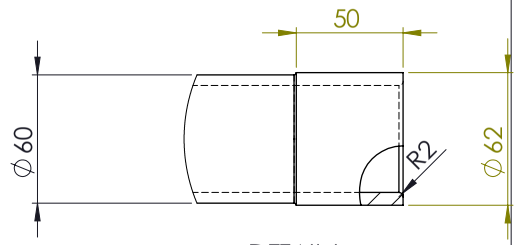

DETAIL I
SCALE 2 : 5

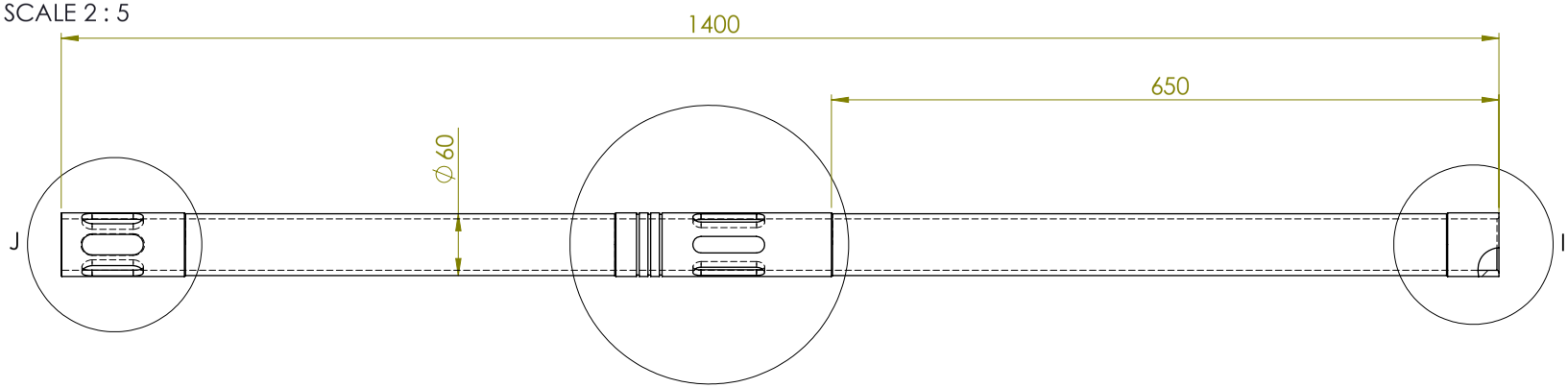

E

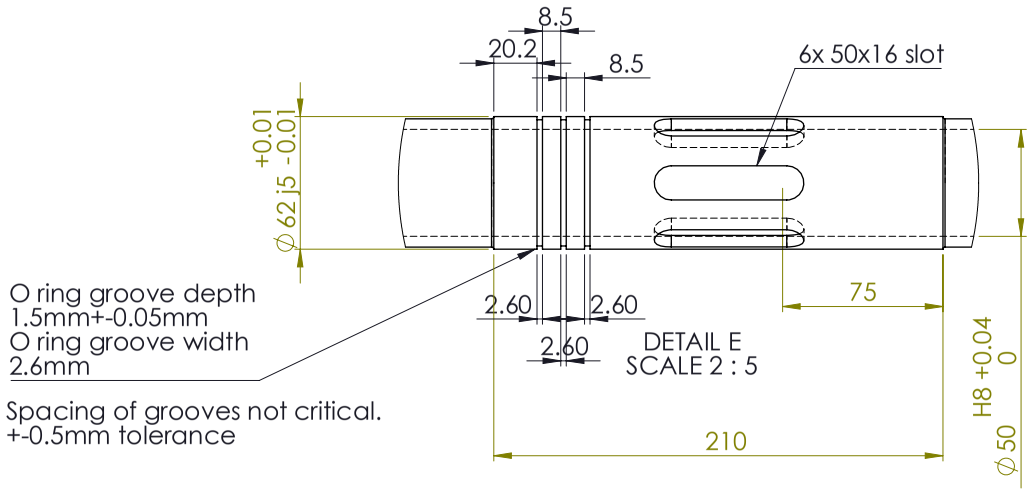

DETAIL E
SCALE 2 : 5

All edges 0.5x45° chamfer unless otherwise stated.

Inner surface supplied honed, and not to be machined where possible

A3 Landscape	University of Cape Town Department of Mechanical Engineering				
	Title: Barrel				
Quantity: 1	Part Finish	Date: 09/04/2018	Scale: 1:10	Barrel	of 15
Material: Steel	Drawn By: GRHAAR001			Drawing Number 4	

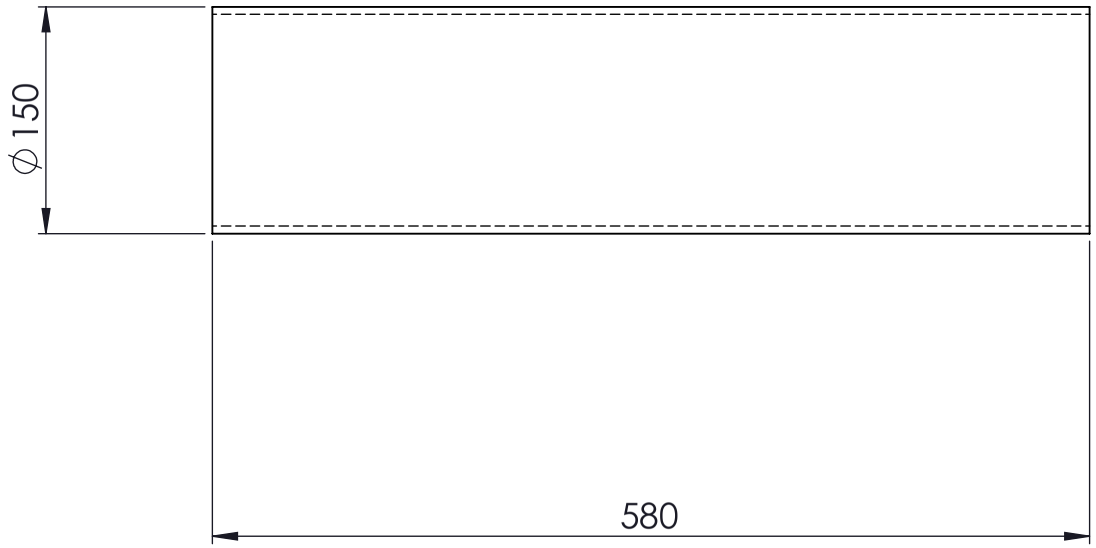

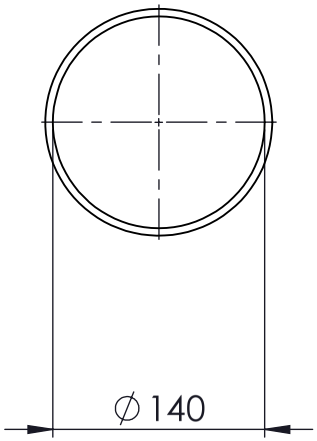

SOLIDWORKS Educational Product. For Instructional Use Only

A4 Landscape	University of Cape Town Department of Mechanical Engineering				
	Title: Reservoir				
Quantity: 1	Part Finish	Date: 09/04/2018	Scale: 1:5	Reservoir	of 15
Material: Mild Steel	Drawn By: GRHAAR001			Drawing Number 5	

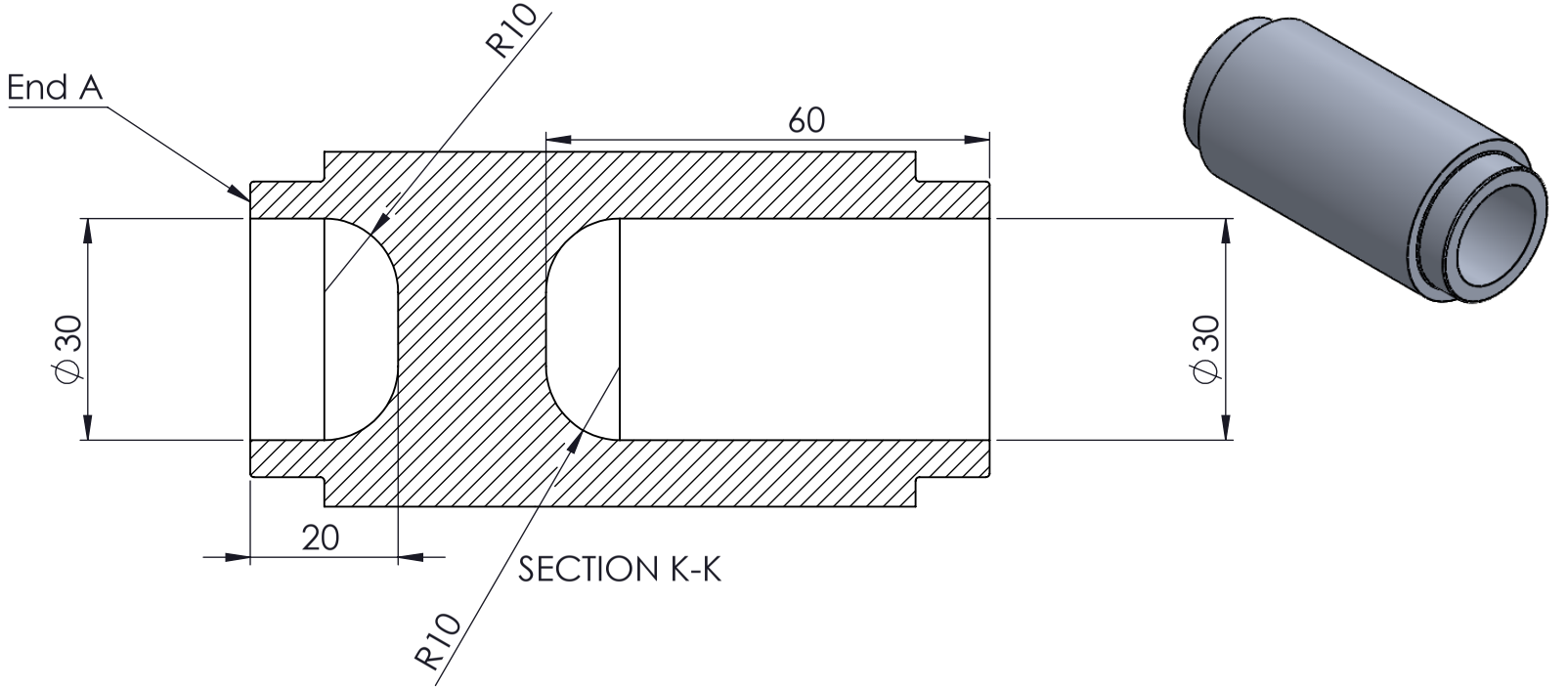

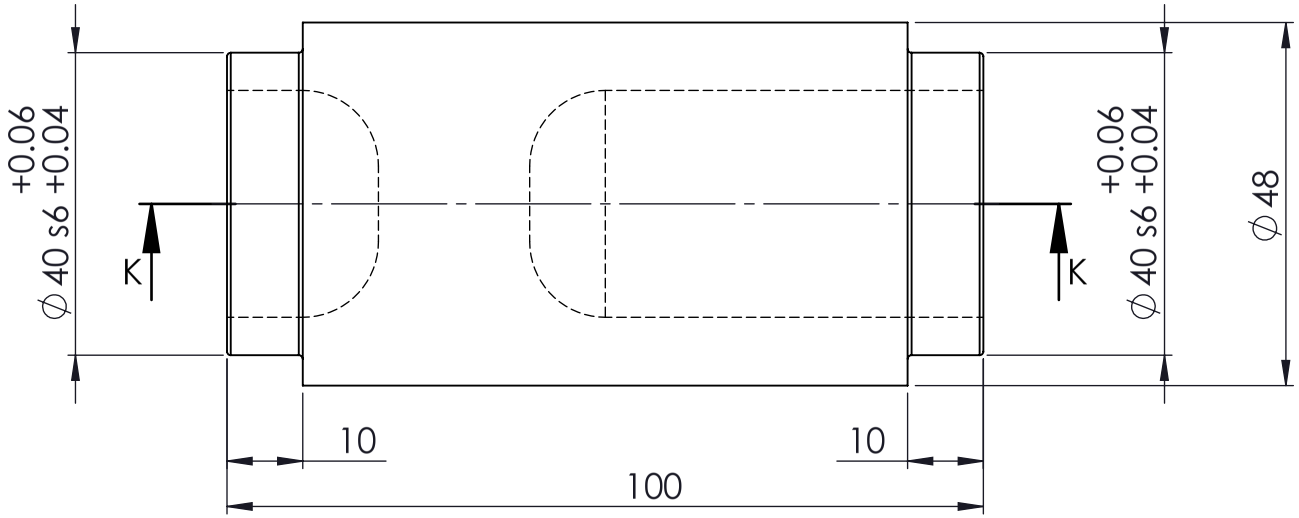

2x Phosphor Bronze bushing to be pressed onto ends. End A to be ground flat after bushing is pressed on

A4 Landscape	University of Cape Town Department of Mechanical Engineering				
	Title: BiMetallic Piston				
Quantity: 1	Part Finish	Date: 09/04/2018	Scale: 1:1	BiMetallic Piston	of 15
Material: Al 7075 T6	Drawn By: GRHAAR001			Drawing Number 6	

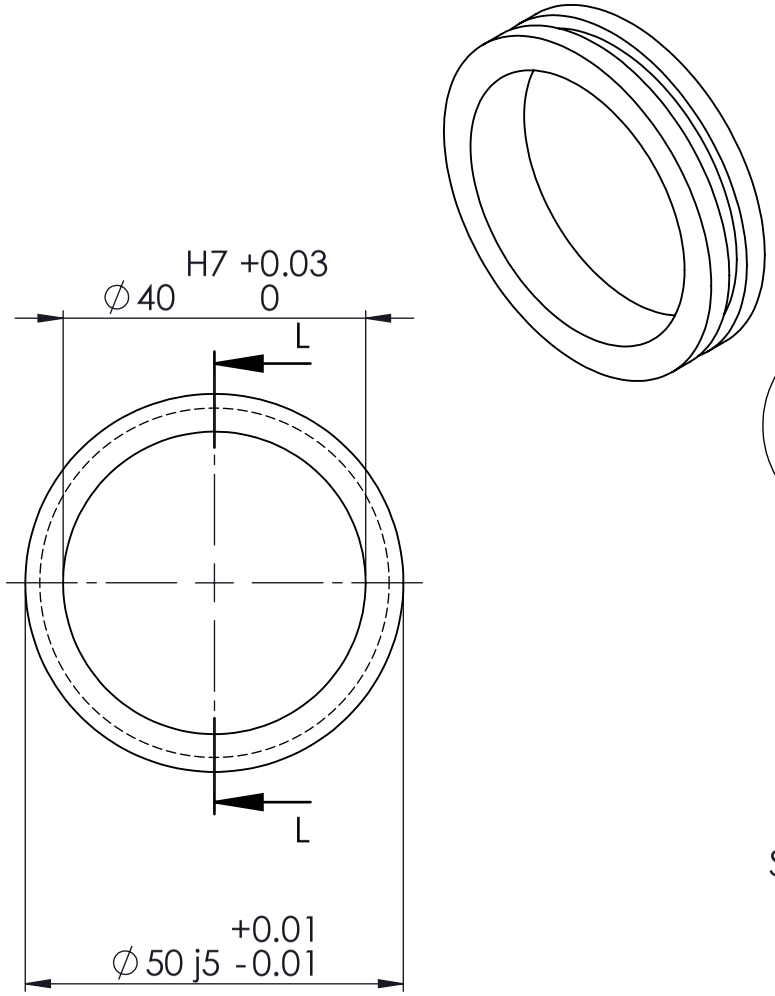

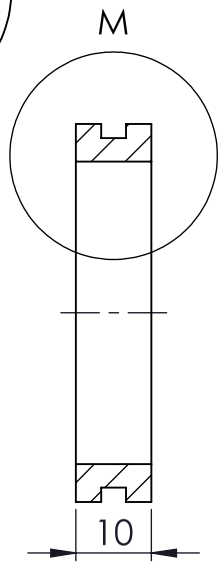

SECTION L-L

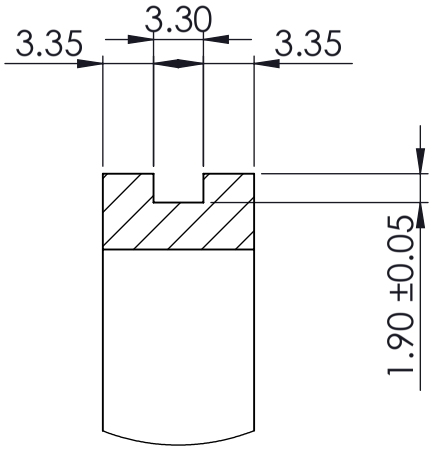

DETAIL M
SCALE 2 : 1

To be pressed onto BiMetallic Piston ends

A4 Landscape	University of Cape Town Department of Mechanical Engineering				
	Title: Bushing				
Quantity: 2	Part Finish	Date: 09/04/2018	Scale: 1:1	Bushing	of 15
Material: Phosphor Bronze	Drawn By: GRHAAR001			Drawing Number 7	

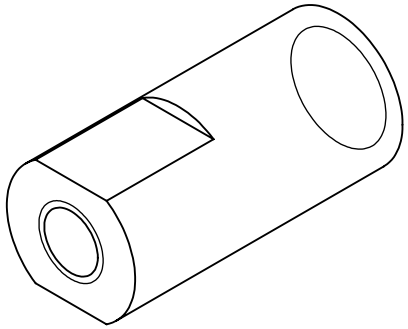

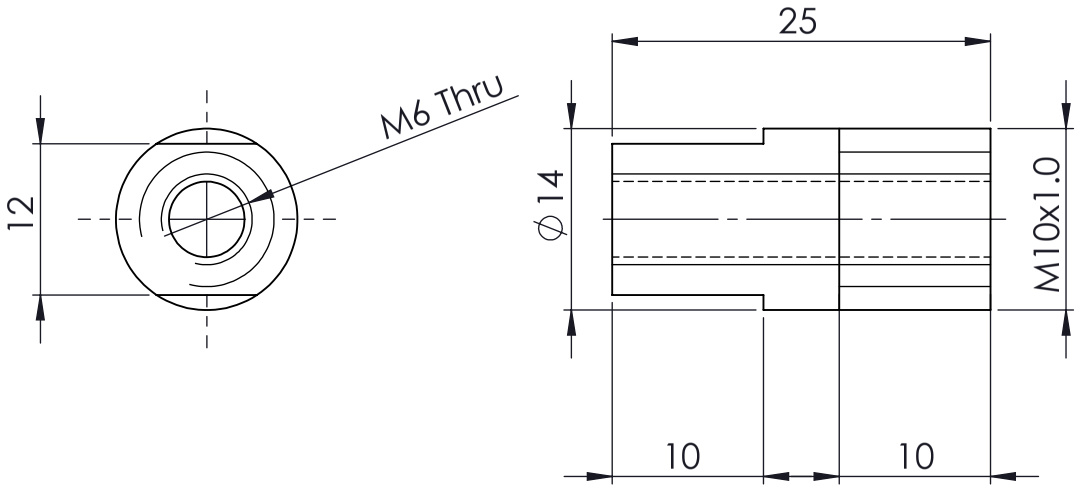

A4 Landscape	University of Cape Town Department of Mechanical Engineering				
	Title: Adapter				
Quantity: 1	Part Finish	Date: 09/04/2018	Scale: 2:1	Adapter	of 15
Material: Stainless steel	Drawn By: GRHAAR001			Drawing Number 8	

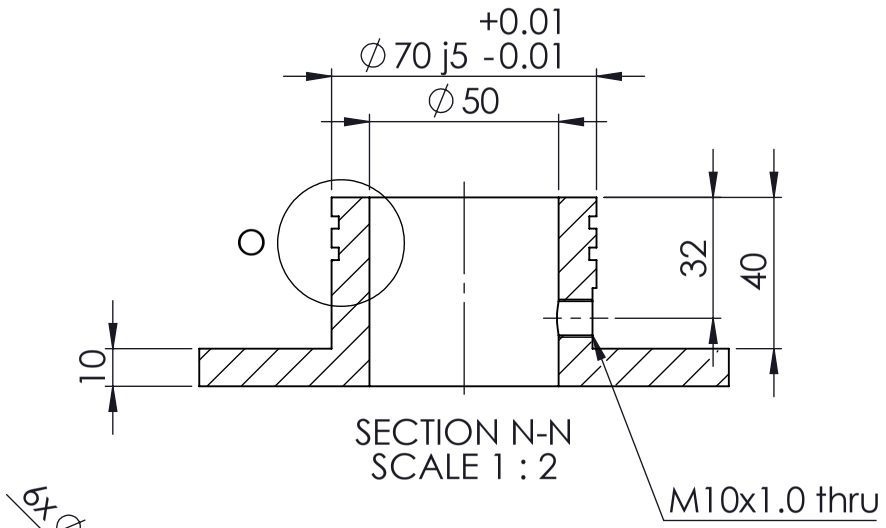

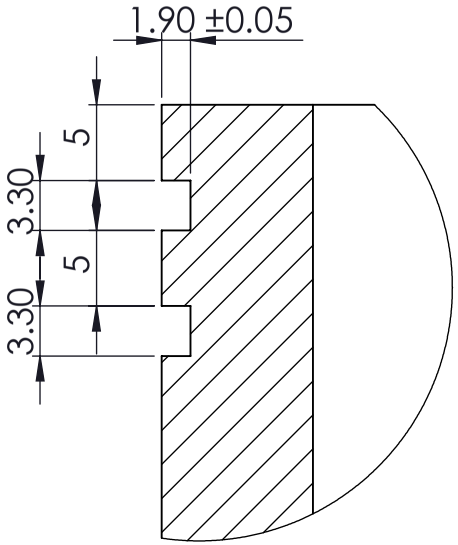

DETAIL O
SCALE 2 : 1

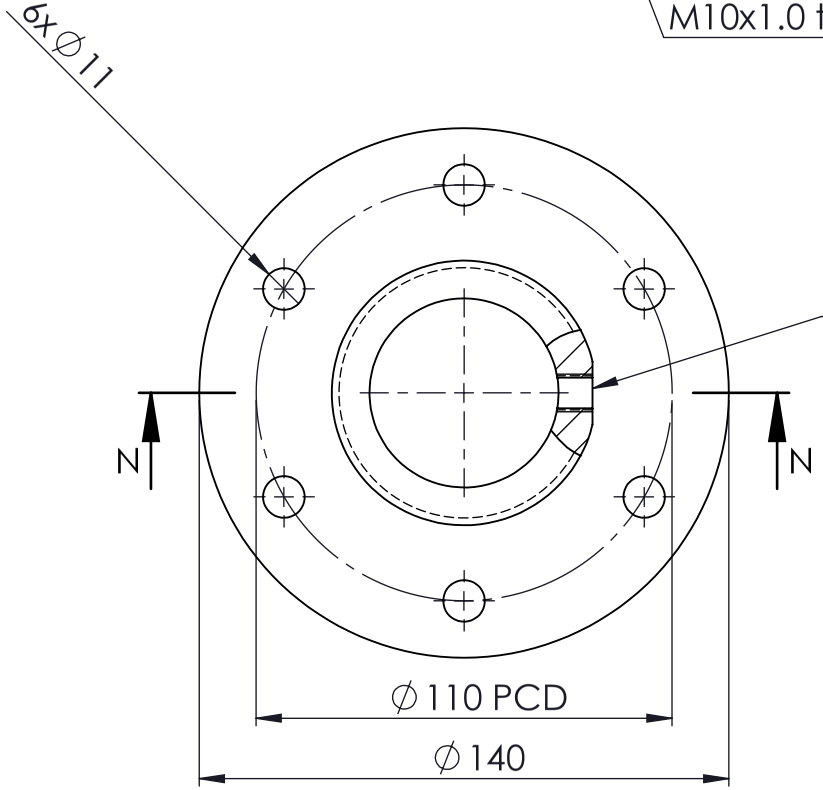

SOLIDWORKS Educational Product. For Instructional Use Only

A4 Landscape	University of Cape Town Department of Mechanical Engineering				
	Title: Clamp 2				
Quantity: 1	Part Finish	Date: 09/04/2018	Scale: 1:5	Clamp2	of 15
Material: Stainless Steel	Drawn By: GRHAAR001			Drawing Number 9	

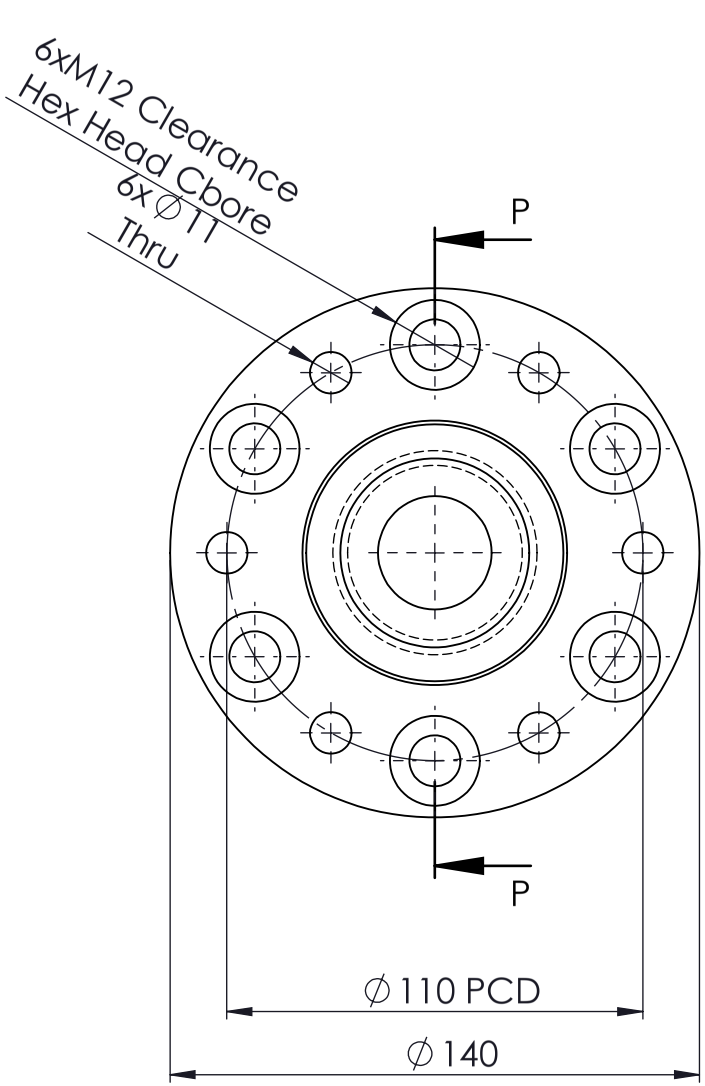

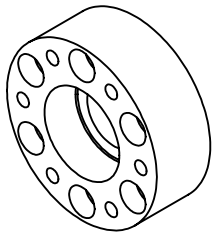

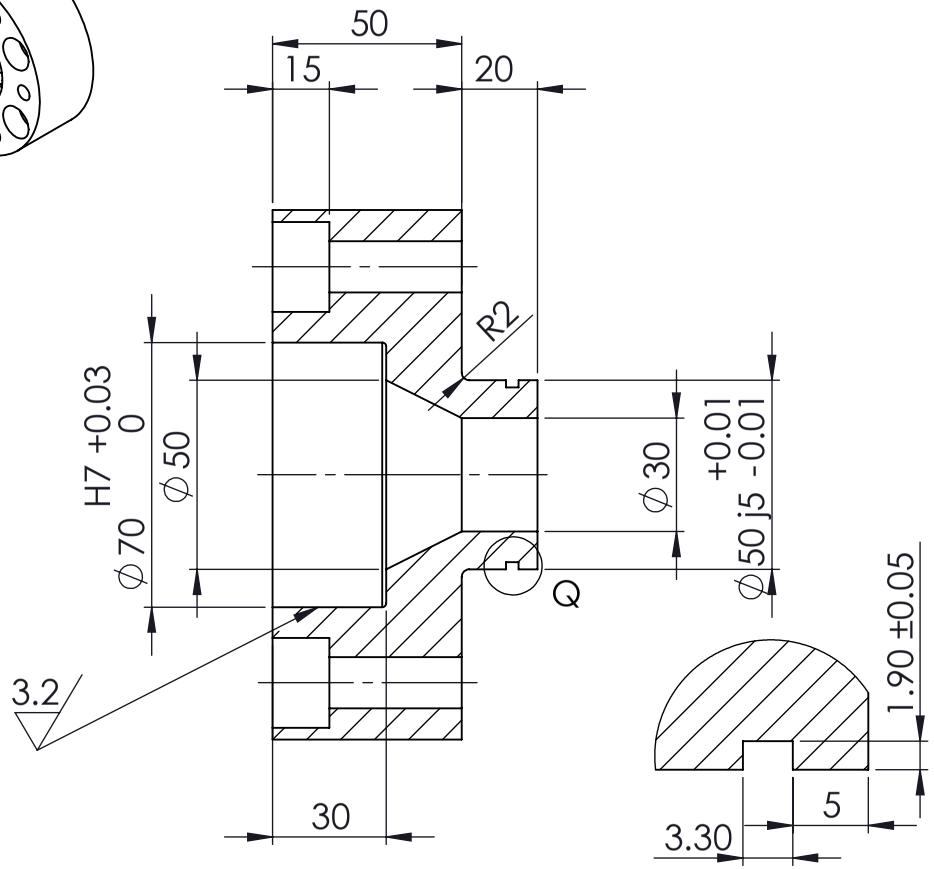

SECTION P-P
SCALE 1 : 2

DETAIL Q
SCALE 2 : 1

A4 Landscape	University of Cape Town Department of Mechanical Engineering				
	Title: EndCap small				
Quantity: 1	Part Finish	Date: 09/04/2018	Scale: 1:5	EndCapSmall	of 12
Material: AL 7075 T6	Drawn By: GRHAAR001			Drawing Number 10	

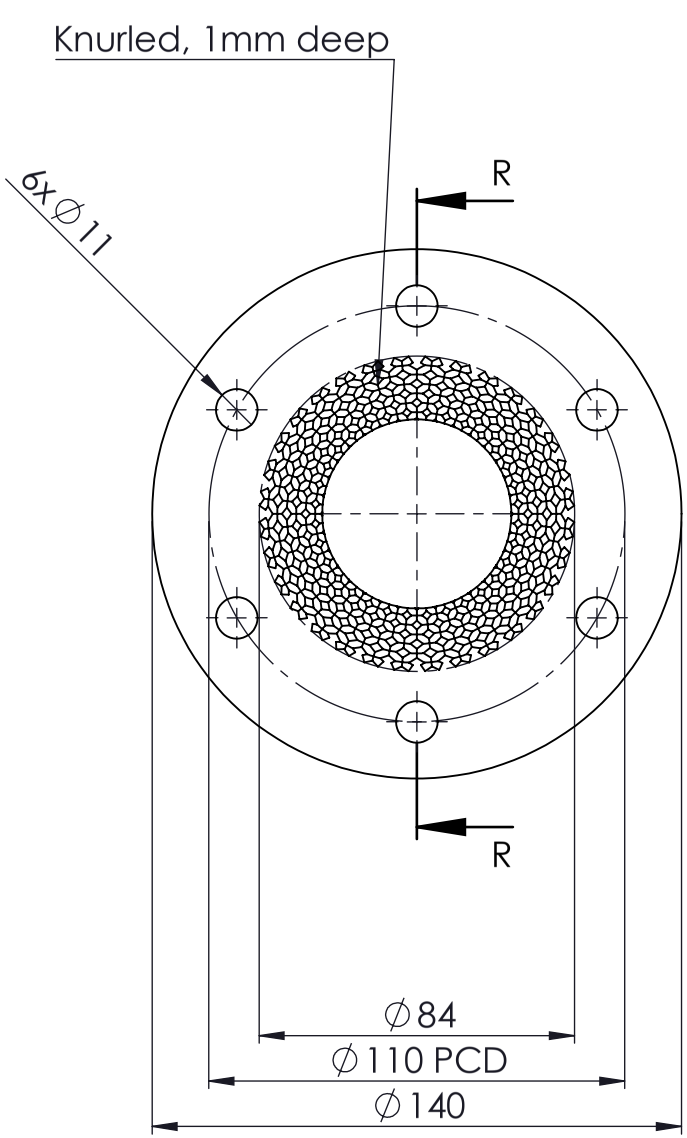

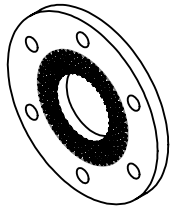

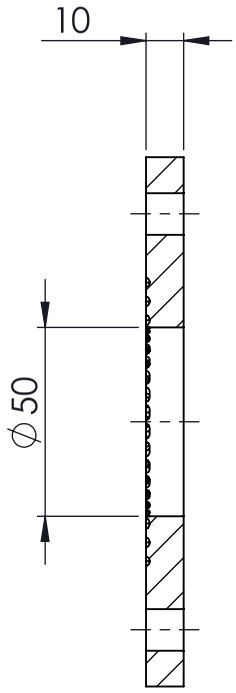

SECTION R-R
SCALE 1 : 2

Knurled section to be Knurled to a depth of 1mm

A4 Landscape	University of Cape Town Department of Mechanical Engineering				
	Title: Membrane Clamp				
Quantity: 1	Part Finish	Date: 09/04/2018	Scale: 1:5	Membrane Clamp	of 15
Material: Stainless Steel	Drawn By: GRHAAR001			Drawing Number 11	

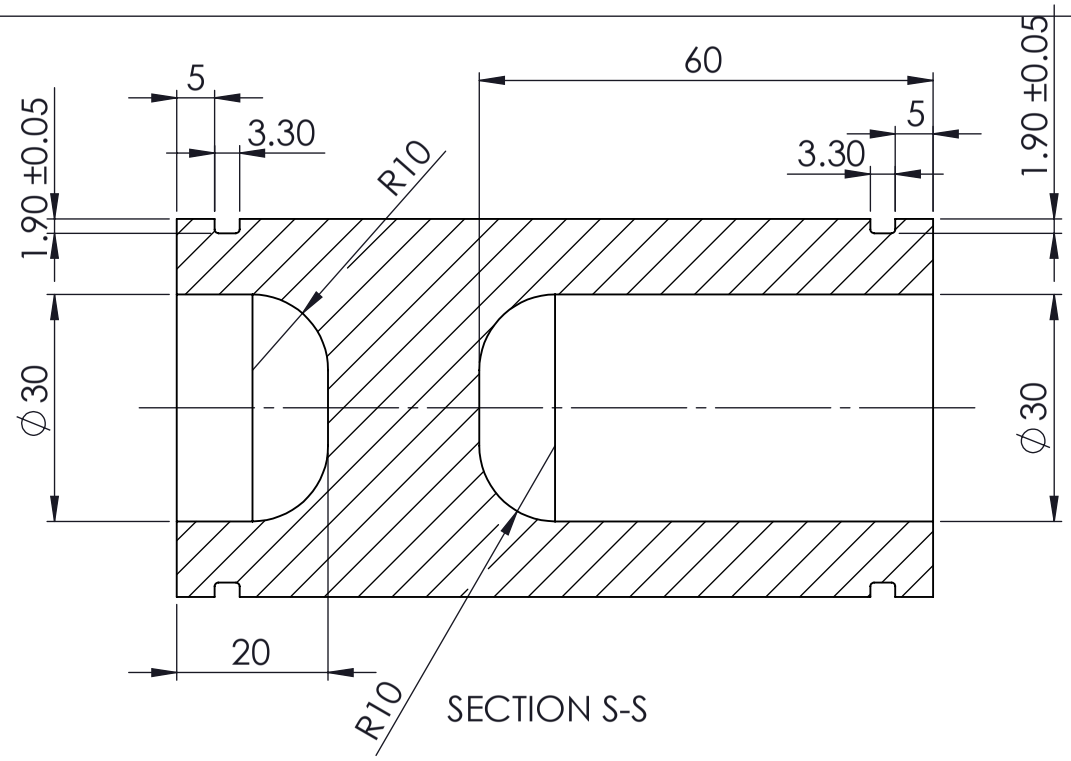

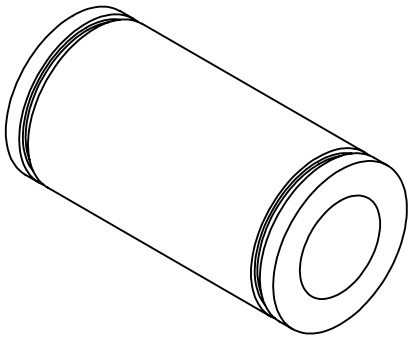

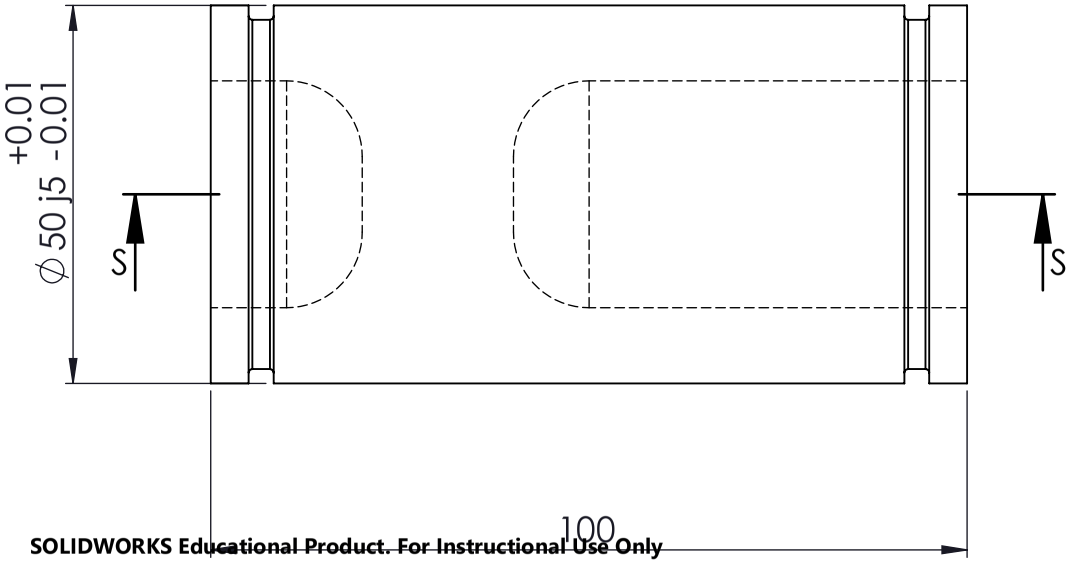

A4 Landscape	University of Cape Town Department of Mechanical Engineering				
	Title: Homogenous Piston				
Quantity: 1	Part Finish	Date: 09/04/2018	Scale: 1:1	Homogenous piston	of 15
Material: Al 7075 T6	Drawn By: GRHAAR001			Drawing Number 12	

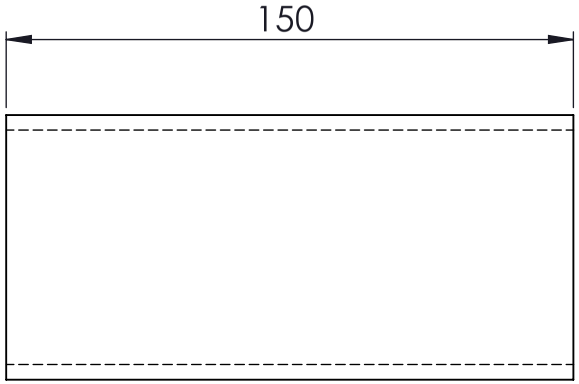

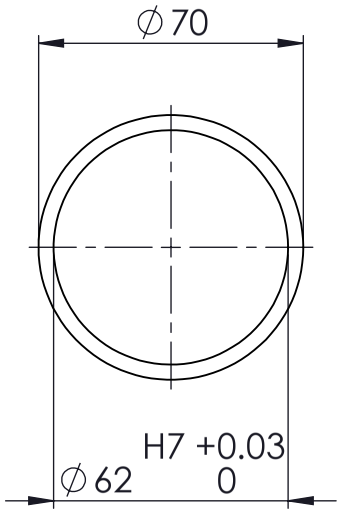

OD not important. Can range from 68 to 75 depending on material available

A4 Landscape	University of Cape Town Department of Mechanical Engineering				
	Title: Sleeve valve				
Quantity: 1	Part Finish	Date: 09/04/2018	Scale: 1:2	Sleeve Valve	of 15
Material: Steel	Drawn By: GRHAAR001			Drawing Number 13	

Some fasteners etc ommitted for clarity

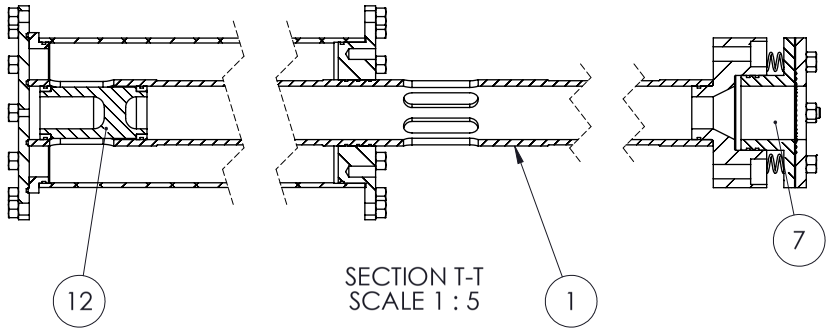

SECTION T-T
SCALE 1 : 5

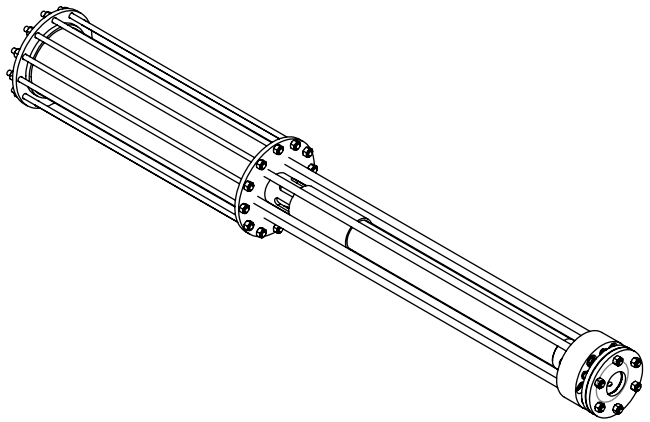

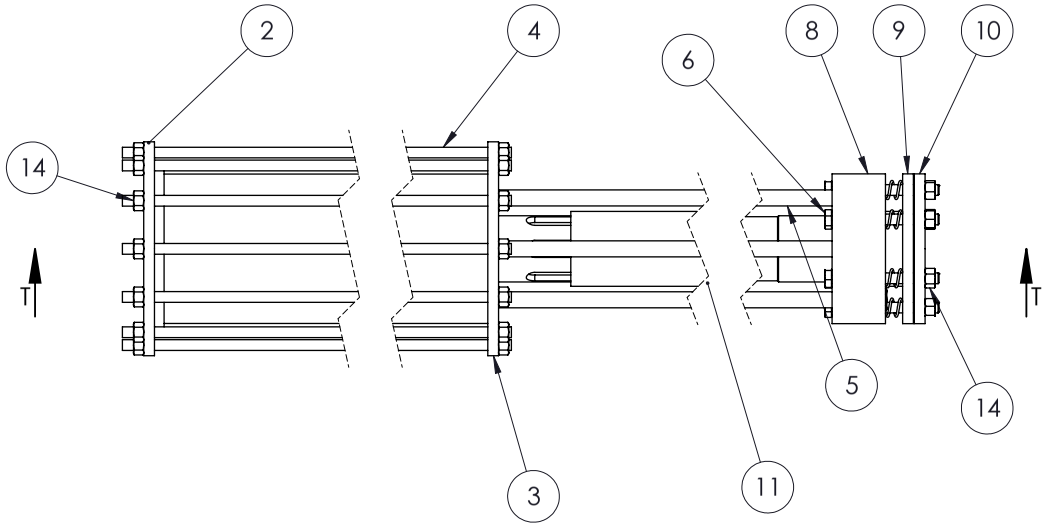

ITEM NO.	PART NAME	QTY.
1	Barrel	1
2	EndCap	1
3	MidCap	1
4	M10x640 threaded rod	12
5	M12x875 threaded rod	6
6	M10x110 hex bolt	6
7	spring	6
8	EndCapSmall2	1
9	clamp2	1
10	membrane clamp	1
11	sleeve valve	1
12	Piston bimetallic	1
14	M10 hex nut	30
15	M12 hex nut	6
16	Interface	1
17	Reservoir New	1

A3 Landscape

University of Cape Town
Department of Mechanical Engineering

Title:

Assembly Drawing

Scale: 1:50

Date: 09/04/2018

Assembly of 15

Drawn By: GRHAAR001

Drawing Number 1

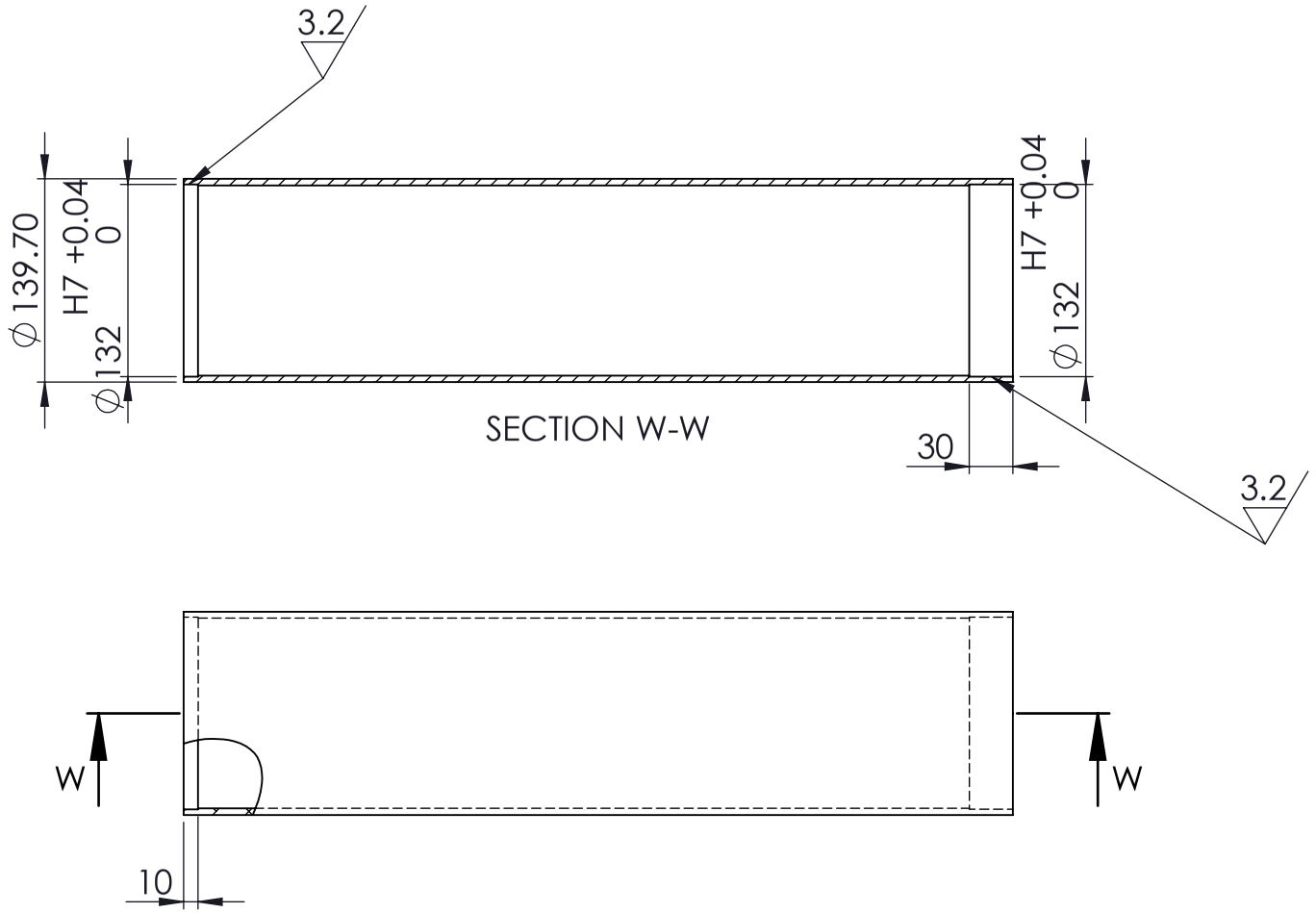

A4 Landscape	University of Cape Town Department of Mechanical Engineering				
	Title: ReservoirNew				
Quantity: 1	Part Finish	Date: 09/04/2018	Scale: 1:5	ReservoirNew	of 15
Material: Steel	Drawn By: GRHAAR001			Drawing Number 14	

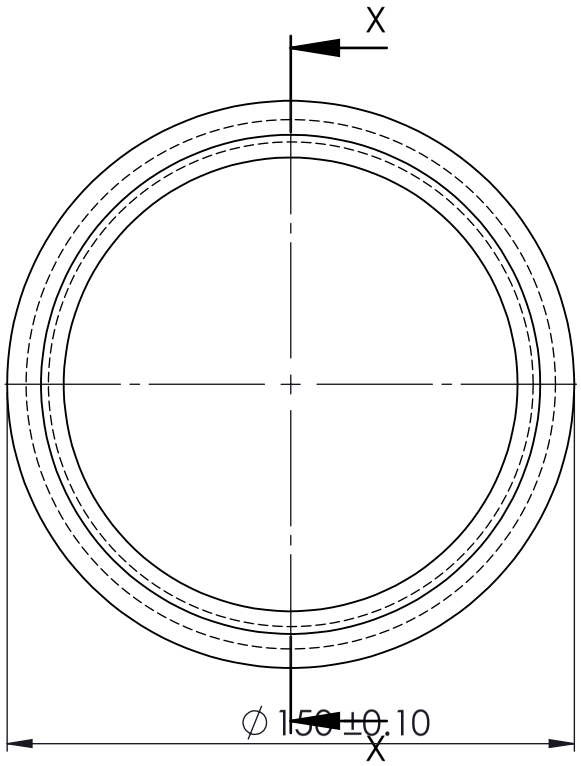

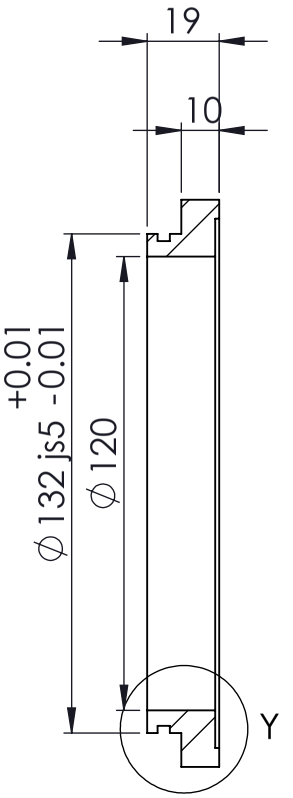

SECTION X-X

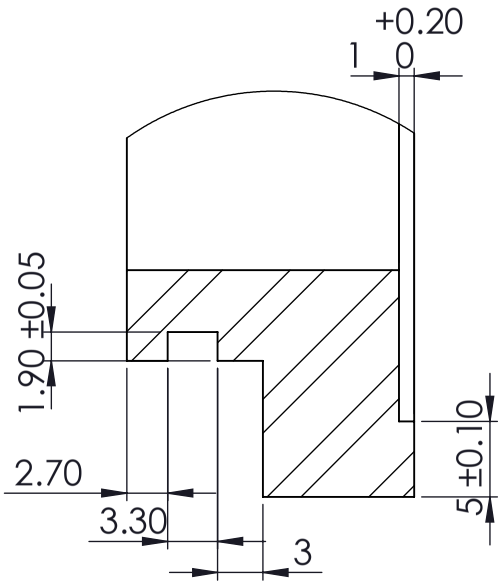

DETAIL Y
SCALE 2 : 1

A4 Landscape	University of Cape Town Department of Mechanical Engineering				
	Title: Interface				
Quantity: 1	Part Finish	Date: 09/04/2018	Scale: 1:2	Interface	of 15
Material: Mild Steel	Drawn By: GRHAAR001			Drawing Number 15	

Appendix I

Scope of project

The scope of this project did not initially include the selection and development of skin simulants and design of a viable specimen fixture and speckle pattern generation method. As this dissertation is a sub-set of a larger bulge testing project at the University of Cape Town, it had been planned that all three sub-projects (quasi-static, intermediate rate, and high strain rate bulging) would use the same simulants, clamp methodology and speckle pattern generation method. Given the significantly lower amount of design and analysis inherent in low strain rate testing, it had been anticipated that the development of a specimen fixture methodology and speckle pattern generation method would fall under that project.

Unfortunately the methodology used/developed initially in the quasi-static bulge test project was not successful, and a significant amount of time was taken from this project in order to develop the aforementioned methodology. This methodology was then used across the larger project.

As a result of this, there was reduced time available for numerical modelling and use of alternative methods of inverse iterative parameter identification.

Appendix J

Code

```
# -*- coding: utf-8 -*-
"""
Created on Tue Jul 24 22:48:58 2018

@author: Aaron Graham
"""

from matplotlib import pyplot as plt
plt.style.use('seaborn-deep')# Please see https://www.researchgate.net/publication/
6419747_Rainbow_Color_Map_Still_Considered_Harmful
import csv
from IndividualProcesser import ProcessCollateData as IP
from IndividualProcesser import plotter
from IndividualProcesser import plotStats
from IndividualProcesser import bfSL


metaFileName = 'MetaDataUpdated.csv'
metaData = [['PressureData'],['xStrain'],['yStrain'],['zDisplacement'],['ProcessedName'],['fps'],['frame0'],
['frameEnd'],['Material'],['Minor Diameter'],['Membrane Thickness'],['Driving Pressure']]

lagrangian = 0 # calculates lagrangian strain if 1, stretch ratio if 0
triggerPressure = 2*10**-3 #trigger pressure which is considered to be the zero point
generate = 1 #whether to generate files of collated data
plotAll = 0 #whetehr to plot each dataset as it is generated

plotConditions = [[0,11],['60Duro',630]]#in format column, condition
plotCols1 = [0,2]
plotCols2 = [0,3]
plotFactors = [1,1]
plotLables = [' ','Y strain','Apex z displacement (mm)']
plotMarkers = ['-','--']
plotXLable = 'Time (ms)'
plotTitle = 'Pressure and apex strain vs time for circular 60 Duro silicone samples at 250kpa Driving
pressure'
colour = ['b','g','r','c','m','y','k']
fSize=(8,4)

#%%% Reading from metaData file, getting information about each test
f = open(metaFileName,"r")
reader = csv.reader(f)
```

```
r = 0
class Found(Exception): pass
try:
    for row in reader:
        if(r>0):
            c = 0
            for col in row:
                if(col=='skip'):
                    r-=1
                    break
                if(col is None or col == "" and c<13):#bit of an overkill to raise an error, but such is life
                    raise Found
                if(c>0):
                    if(c<6):
                        metaData[c-1].append(col+'.csv')
                    elif(c<9):
                        metaData[c-1].append((float)(col))
                    elif(c==9):
                        metaData[c-1].append(col)
                    elif(c<13):
                        metaData[c-1].append((float)(col))
                    if(c==12):
                        break
                c+=1

#                 if(c==1):
#                     pNames.append(col+'.csv')
#                 if(c==2):
#                     xNames.append(col+'.csv')
#                 if(c==3):
#                     yNames.append(col+'.csv')
#                 if(c==4):
#                     zNames.append(col+'.csv')
#                 if(c==5):
#                     outNames.append(col+'.csv')
#                 if(c==6):
#                     fps.append((float)(col))
#                 if(c==7):
#                     f0.append((float)(col))
#                 if(c==8):
#                     fEnd.append((float)(col))
```

```
#                 if(c>8):
#                     break
#                 c+=1
        r+=1
except Found:
    print('Row that casued crash: '+(str)(r))

nFiles = r
#%%% Generating processed data files
if(generate):
    for i in range(1,nFiles):

        try:
            #IP(pNames[i],xNames[i],yNames[i],zNames[i],outNames[i],fps[i],f0[i],fEnd[i],plotAll,triggerPressu
re)
            IP(metaData[0][i],metaData[1][i],metaData[2][i],metaData[3][i],metaData[4][i],metaData[5]
[i],metaData[6][i]
           ,metaData[7][i],plotAll,triggerPressure,fSize,lagrangian)
        except Exception as e:
            print('Error in ',metaData[0][i]+' : '+(str)(i))
            print(e)

#%%%%Plotting stuff

fig,ax = plt.subplots(1,2,sharey=True,figsize=fSize)
testNo = 0
plNames = []
for i in range(1,nFiles):
    found = 1#assume that we have found what we need
    #print('\n\n\n')
    #print(i)
    for j in range(len(plotConditions[0])):
        c = plotConditions[0][j]
        if not ((str)(plotConditions[1][j]) in (str)(metaData[c][i])):
          #  print((str)(plotConditions[0][j]))
           # print((str)(metaData[c][i])+'!='+(str)(plotConditions[1][j]))
            found = 0#we didn't find what we need
    if(found):
        print('found :'+metaData[0][i]+';'+(str)(i))
#        plotter(ax,metaData[4][i],plotCols,plotMarkers,plotLables,testNo,colour[testNo],plotFactors)
        plotter(ax[0],metaData[4][i],plotCols1,plotMarkers,plotLables,(str)((int)(metaData[11][i]))+'
```

```
kpa',colour[testNo],plotFactors)
        plotter(ax[1],metaData[4][i],plotCols2,plotMarkers,plotLables,(str)((int)(metaData[11][i]))+'
kpa',colour[testNo],plotFactors)
        testNo+=1
        plNames.append(metaData[4][i])
    #else:
        #print(metaData[0][i])
plt.xlabel(plotXLable)
ax[0].set_ylabel('Apex stretch ratio')
ax[0].set_xlabel('time (ms)')
ax[0].grid()
ax[0].legend()
ax[1].legend()
ax[0].set_title('X stretch')
ax[1].set_title('Y stretch')
ax[0].grid(which='minor', axis='both', linestyle='-')
ax[1].set_xlabel('time (ms)')
ax[1].grid()
ax[1].grid(which='minor', axis='both', linestyle='-')
#plt.title(plotTitle)
fig.subplots_adjust(wspace=0.05)

#plt.savefig('eg.pdf')
#%%% Stats plot thing
#fig,(ax1,ax2,ax3) = plt.subplots(3,1,sharex=True,figsize=fSize)
#fig.subplots_adjust(hspace=0)
#plotStats(ax1,plNames,0,1,'g','Membrane pressure',10**3)
#ax1.legend()
#plotStats(ax2,plNames,0,2,'r','X stretch ratio',1)
#ax2.legend()
#plotStats(ax3,plNames,0,4,'b','Apex Z displacement',(1))
#ax3.legend()
##plt.grid()
##plt.grid(which='fine')
##plt.ylabel(r'Pressure ($10^5$ kPa)')
#
#ax1.grid()
#ax1.grid(which='minor', axis='both', linestyle='-')
#ax2.grid()
#ax2.grid(which='minor', axis='both', linestyle='-')
#ax3.grid()
```

```
#ax3.grid(which='minor', axis='both', linestyle='-')
#ax1.set_ylabel(r'Pressure (kPa)')
#ax2.set_ylabel(r'Apex stretch ratio')
#ax3.set_ylabel(r'Apex displacement (mm)')
#plt.xlabel(plotXLable)
#fig.tight_layout()
#fig.subplots_adjust(hspace=0)

#%% big grid plot 60 Duro
#D5050 = [10,12,13,14];
#D5040 = [15,16,17,18];
#D5030 = [19,21,22,23];
#D5020 = [24,25,27,28];

#D5050 = [14,13,12,10];
#D5040 = [18,17,16,15];
#D5030 = [23,22,21,19];
#D5020 = [28,27,25,24];
#lst = [D5050,D5040,D5030,D5020];
#xMin = -1;
#xMax = 32.0;
#fig, axs = plt.subplots(4,2,True,True,figsize=(9,9));
#for i in range(4):
#    for j in range (len(lst[i])):
#        plotter(axs[i,0],metaData[4][lst[i][j]],[0,2],plotMarkers,plotLables,(str)((int)(metaData[11][lst[i]
[j]]))+' kPa',colour[j],plotFactors)
#        plotter(axs[i,1],metaData[4][lst[i][j]],[0,3],plotMarkers,plotLables,(str)((int)(metaData[11][lst[i]
[j]]))+' kPa',colour[j],plotFactors)
#
#
#    axs[i,0].set_title('50x'+(str)((int)(metaData[9][lst[i][1]]))+'mm: Minor axis')
#    axs[i,1].set_title('50x'+(str)((int)(metaData[9][lst[i][1]]))+'mm: Major axis')
#    axs[i,0].grid()
#    axs[i,1].grid()
#    axs[i,0].legend()
#    axs[i,1].legend()
#    axs[i,0].set_ylabel('Apex stretch ratio')
#    axs[3,0].set_xlabel('time(ms)')
#    axs[3,1].set_xlabel('time(ms)')
#axs[0,0].set_xlim(xMin,xMax);
#fig.subplots_adjust(wspace=0.02)
```

```
#fig.tight_layout()
#%% circular textile varying pressure
#xMin = -1;
#xMax = 35.0;
##N = [29,30,31,32,33]
#N = [33,32,31,30,29]
#fig,axs = plt.subplots(1,2,True,True,figsize=(8,3.5))
#for i in range(5):
#    plotter(axs[0],metaData[4][N[i]],[0,2],plotMarkers,plotLables,(str)((int)(metaData[11][N[i]]))+'
kPa',colour[i],plotFactors)
#    plotter(axs[1],metaData[4][N[i]],[0,3],plotMarkers,plotLables,(str)((int)(metaData[11][N[i]]))+'
kPa',colour[i],plotFactors)
#axs[0].grid()
#axs[1].grid()
#axs[0].legend()
#axs[1].legend()
#axs[0].set_xlabel('time(ms)')
#axs[1].set_xlabel('time(ms)')
#axs[0].set_ylabel('Apex stretch ratio')
#axs[0].set_xlim(xMin,xMax)
#axs[0].set_ylim(0.95,1.65)
#axs[0].set_title('Weft axis')
#axs[1].set_title('Warp axis')
#fig.subplots_adjust(wspace=0.02)
#fig.tight_layout()

#%% constant pressure, varying geometry textile
#xMin = -1;
#xMax = 31.0;
##N = [29,30,31,32,33]
#N = [5,4,3,2,1]
#N250 = [5,2,1]
#N300 = [4,3]
#fig,axs = plt.subplots(2,2,True,True,figsize=(8,6))
#N = N250
#for i in range(3):
#    plotter(axs[0,0],metaData[4][N[i]],[0,3],plotMarkers,plotLables,(str)((int)(metaData[9][N[i]]))+'mm x
50mm',colour[i],plotFactors)
#    plotter(axs[0,1],metaData[4][N[i]],[0,2],plotMarkers,plotLables,(str)((int)(metaData[9][N[i]]))+'mm x
50mm',colour[i],plotFactors)
#axs[0,0].grid()
```

```
#axs[0,1].grid()
#axs[0,0].legend()
#axs[0,1].legend()
#axs[0,0].set_xlabel('time(ms)')
#axs[0,1].set_xlabel('time(ms)')
#axs[0,0].set_ylabel('Apex stretch ratio')
#axs[0,0].set_xlim(xMin,xMax)
#axs[0,0].set_ylim(0.95,1.65)
#axs[0,0].set_title('Weft axis: 250kPa driving pressure')
#axs[0,1].set_title('Warp axis: 250kPa driving pressure')
#
#N = N300
#for i in range(2):
#    plotter(axs[1,0],metaData[4][N[i]],[0,3],plotMarkers,plotLables,(str)((int)(metaData[9][N[i]]))+'mm x
50mm',colour[i],plotFactors)
#    plotter(axs[1,1],metaData[4][N[i]],[0,2],plotMarkers,plotLables,(str)((int)(metaData[9][N[i]]))+'mm x
50mm',colour[i],plotFactors)
#axs[1,0].grid()
#axs[1,1].grid()
#axs[1,0].legend()
#axs[1,1].legend()
#axs[1,0].set_xlabel('time(ms)')
#axs[1,1].set_xlabel('time(ms)')
#axs[1,0].set_ylabel('Apex stretch ratio')
#axs[1,0].set_xlim(xMin,xMax)
#axs[1,0].set_ylim(0.95,1.65)
#axs[1,0].set_title('Weft axis: 300kPa driving pressure')
#axs[1,1].set_title('Warp axis: 300kPa driving pressure')
#fig.subplots_adjust(wspace=0.02)
#fig.tight_layout()

#%% Low strain rate stuff, 60 Duro
#N = [36,37,38,39]
#N = [39,38,37,36]
#nd = [115,140,100,120]
#fig,ax = plt.subplots(figsize=(7,4))
#for i in range(4):
#    plotter(ax,metaData[4][N[i]],[0,2],plotMarkers,plotLables,(str)((int)(metaData[11][N[i]]))
+'kPa',colour[i],plotFactors)
#plt.legend()
#plt.xlim(-5,160)
```

```
#plt.ylabel('Apex stretch ratio')
#plt.xlabel('time(ms)')
#plt.grid()
#plt.grid(which='fine')
#
#for i in range(4):
#    rate,rSq = bfSL(metaData[4][N[i]],0,2,0,nd[i],10**-3)
#    print(metaData[4][N[i]])
#    print(rate)
#    print(rSq)

#%% Low strain rate stuff, 10 Duro
#N = [39,38,37,36]
#nd = [115,140,100,120]
#fig,ax = plt.subplots(figsize=(7,4))
#for i in range(4):
#    plotter(ax,metaData[4][N[i]],[0,2],plotMarkers,plotLables,(str)((int)(metaData[11][N[i]]))
+'kPa',colour[i],plotFactors)
#plt.legend()
#plt.xlim(-5,160)
#plt.ylabel('Apex stretch ratio')
#plt.xlabel('time(ms)')
#plt.grid()
#plt.grid(which='fine')
#
#for i in range(4):
#    rate,rSq = bfSL(metaData[4][N[i]],0,2,0,nd[i],10**-3)
#    print(metaData[4][N[i]])
#    print(rate)
#    print(rSq)

#%% Just plotting stuff quick for another section
#P = (40,60,100,200)
#SR = (0.263,0.468,1.09,2.28)
#fig,ax = plt.subplots(figsize=(4,5))
#ax.plot(P,SR,'-*',linewidth=1,label='Apex strain rate')
#ax.set_ylabel(R'Strain rate ($s^{-1}$)')
#plt.legend()
#plt.grid()
#plt.grid(which='fine')
#plt.xlabel('Driving pressure (kPa)')
```

```
#plt.title('Apex strain rate vs driving pressure')
#fig.tight_layout()

#%% High strain rate stuff, 60 Duro
#N = [41]
#nd = [115,140,100,120]
#fig,ax = plt.subplots(figsize=(4,4))
#for i in range(1):
#    plotter(ax,metaData[4][N[i]],[0,2],plotMarkers,plotLables,(str)((int)(metaData[11][N[i]]))
+'kPa',colour[i],plotFactors)
#plt.legend()
#plt.xlim(-1,2.5)
#plt.ylabel('Apex stretch ratio')
#plt.xlabel('time(ms)')
#plt.grid()
#plt.grid(which='fine')
#
#for i in range(1):
#    rate,rSq = bfSL(metaData[4][N[i]],0,2,140.5,150,10**-3)
#    print(metaData[4][N[i]])
#    print(rate)
#    print(rSq)
```

```
# -*- coding: utf-8 -*-
"""
Created on Fri Jul 20 20:15:00 2018

@author: Aaron Graham
"""
import numpy as np
from matplotlib import pyplot as plt
import csv
from scipy import signal
from scipy import stats
from scipy.interpolate import interp1d

def
ProcessCollateData(pName,xStrName,yStrName,zName,outputName,fps,frame0,frameEnd,plot,triggerPressure,fSize,lag
rangian):
    tStart = frame0/fps
    tEnd = frameEnd/fps
    pUnitConv = 661050.81495*10**-6#MPa per volt
    tV = np.zeros((78125,3))
    tPXYZ = np.zeros(((int)(frameEnd-frame0+1),7))
    DICLength = 0 #length of the data vector captured byt eh DIC software
    #%%%%%%%%
    ## Obtaining pressure data
    file = open(pName,"r")
    reader = csv.reader(file)
    r = 0
    for row in reader:
        if(r==1):
            c = 0
            for col in row:
                if(c == 0):
                    tUnit = col
                    if(tUnit == '(s)'):
                        pTimeUnit = 1.0
#                        print(pName)
                    if(tUnit == '(ms)'):
                        pTimeUnit = 10**-3
                if(c == 1):
                    vUnit = col
                    if(vUnit == '(mV)'):
```

```
                        #pUnitConv = pUnitConv*(10**-3)#Pa per mV
                        pUnitConv = 661050.81495*10**-9#MPa per mV
                        #print(pName)
                    c+=1
            if(r>3):
                c = 0
                for col in row:
                    if(c == 0):
                        tV[r-4,0] = (float)(col)
                    if(c == 1):
                        tV[r-4,1] = (float)(col)
                    c +=1
                if(r-4==78124):
                    break
            r +=1
        file.close()
        offset = tV[0:7812,1].mean()#finding the zero point voltage
        tV[:,2] = signal.savgol_filter(tV[:,1]-offset,41,3)#subtracting zero point voltage, smoothing out gaussian
    noise

        startIndex = 0
        endIndex = 0
        for i in range(78125):#finding start of pressure
            if(tV[i,0])*pTimeUnit>=tStart:
                startIndex = i-500
                break
        for i in range(78125):#finding end of pressure
            if(tV[i,0]*pTimeUnit >=tEnd):
                endIndex = i+500
                break
        if(endIndex>78124 or endIndex==0):
            endIndex = 78124
        if(startIndex<0):
            startIndex = 0

        endIndex = (int)(endIndex)
        startIndex = (int)(startIndex)
    #    print(tEnd,tStart)
    #    print(endIndex,startIndex)
    #    print(pTimeUnit)
        tP = np.empty((endIndex-startIndex,2))
```

```
    tP[:,0] = tV[startIndex:endIndex,0]*pTimeUnit#time in seconds
    tP[:,1] = tV[startIndex:endIndex,2]*pUnitConv#pressure in MPa
#    if(vUnit=='(mV)'):
#        print(pName)
#        print(pUnitConv)
#        print(pTimeUnit)
#        plt.figure()
#        plt.plot(tP[:,0],tP[:,1])
#        plt.title(pName)
#        print(pName)
#        print(startIndex)
#        print(endIndex)
#    plt.figure()
#    plt.plot(tP[:,0],tP[:,1]*10**3)
#    plt.title(pName)
    #%%% obtaining lagrangian x and y strain, as well as apex height
    file = open(xStrName,"r")
    reader = csv.reader(file)
    r = 0
    for row in reader:
        if(r>2):
            c = 0
            for col in row:
                if(c==0):
                    tPXYZ[r-3,0] = (frame0+(float)(col))/fps
                if(c == 1):
                    if(col is None or col == ""):
                        tPXYZ[r-3,2]= (float)('nan')#to catch blank bits
                    else:
                        if(lagrangian):#lagrangian strain
                            tPXYZ[r-3,2] = (float)(col)*10**-3
                            DICLength = r-2
                        else:#stretch ratio
                            s = (float)(col)*10**-3
                            tPXYZ[r-3,2] = (2*s+1)**0.5
                            DICLength = r-2
                c+=1
        r+=1
        if(r>frameEnd-frame0+2):
            break
    file.close()
```

```
file = open(yStrName,"r")
reader = csv.reader(file)
r = 0
for row in reader:
    if(r>2):
        c = 0
        for col in row:
            if(c == 1):
                if(col is None or col == ""):
                    tPXYZ[r-3,3]= (float)('nan')#to catch blank bits
                else:
                    if(lagrangian):
                         tPXYZ[r-3,3] = (float)(col)*10**-3
                    else:
                        s = (float)(col)*10**-3
                        tPXYZ[r-3,3] = (2*s+1)**0.5
            c+=1
    r+=1
    if(r>frameEnd-frame0+2):
        break
file.close()

file = open(zName,"r")
reader = csv.reader(file)
r = 0
for row in reader:
    if(r>2):
        c = 0
        for col in row:
            if(c == 1):
                if(col is None or col == ""):
                    tPXYZ[r-3,4]= (float)('nan')#to catch blank bits
                else:
                    tPXYZ[r-3,4] = (float)(col)
            c+=1
    r+=1
    if(r>frameEnd-frame0+2):
        break
file.close()
```

```
    #%%%Chopping up pressure data

#    j = 0
#    for i in range(len(tP[:,0])):
#        if(tP[i,0]<=tPXYZ[j,0] and tP[i+1,0]>=tPXYZ[j,0]):
#            tPXYZ[j,1] = (tP[i,1]*(tPXYZ[j,0]-tP[i,0])+tP[i+1,1]*(-tPXYZ[j,0]+tP[i+1,0]))/(tP[i+1,0]-tP[i,
0])#interpolating pressure
#            j+=1
#            if(j>frameEnd-frame0-1):
#                break
    f = interp1d(tP[:,0],tP[:,1],kind='quadratic',fill_value='extrapolate')
    for i in range(len(tPXYZ[:,0])):
        tPXYZ[i,1] = f(tPXYZ[i,0])
    #%%% Sorting out holes in data
    prev = 0
    nxt = 0
    i = 0
    while(i<frameEnd-frame0-1):
        if(not (np.isnan(tPXYZ[i,2]))):
            prev = i
            i+=1 #move on to the next number
        else:
            while(1):#run until I tell it to break, finds the end of the section of missing data
                nxt = i+1
                i+=1
                if(not np.isnan(tPXYZ[i,2])):
                    break
            for j in range(prev+1,nxt):
                tPXYZ[j,2:5] = (tPXYZ[prev,2:5]*(j-prev)+tPXYZ[nxt,2:5]*(nxt-j))/(nxt-prev)#fill values with
linear interpolation


    #%%%% Zeroing time, switching to ms
    tOff = 0
    zeroPoint = 0
    for i in range(DICLength):
        if(tPXYZ[i,1]>=triggerPressure):
            tOff = tPXYZ[i,0]
            zeroPoint = i-5
#            if(pTimeUnit>0.1):
#                print(pName)
```

```
#                print('zero time: '+(str)(tOff))
            break
    tPXYZ[:,0] = (10**3)*(tPXYZ[:,0]-tOff)
#    tenPoint = zeroPoint + (int)(10*fps*10**-3)+5
#    endPoint = zeroPoint + (int)(30*fps*10**-3)+5
#    if(endPoint>DICLength):
#        endPoint = DICLength;

#    print('\n\n')
#    print(outputName)
#    print((str)(np.round(np.max(tP[:,1])*10**3,1)))
#    print('xLin')
#    slope,intercept,rVal,pVal,stderr = stats.linregress(tPXYZ[tenPoint:endPoint,
0]*10**-3,tPXYZ[tenPoint:endPoint,2])
#    print('& '+(str)(np.round(slope,1))+' & '+(str)(np.round(rVal**2,3)))
#    print('yLin')
#    slope,intercept,rVal,pVal,stderr = stats.linregress(tPXYZ[tenPoint:endPoint,
0]*10**-3,tPXYZ[tenPoint:endPoint,3])
#    print('& '+(str)(np.round(slope,1))+' & '+(str)(np.round(rVal**2,3)))


#    xLinear,res,rank,sv,rcond = np.polyfit(tPXYZ[tenPoint:endPoint,0]*10**-3,tPXYZ[tenPoint:endPoint,2],
1,full=True)
#    print('xLin')
#    print(xLinear)
#    print(100*((res/((float)(endPoint-tenPoint)))**0.5)/np.mean(tPXYZ[tenPoint:endPoint,2]))
#
#    yLinear,res,rank,sv,rcond = np.polyfit(tPXYZ[tenPoint:endPoint,0]*10**-3,tPXYZ[tenPoint:endPoint,3],
1,full=True)
#    print('yLin')
#    print(yLinear)
#    print(100*((res/((float)(endPoint-tenPoint)))**0.5)/np.mean(tPXYZ[tenPoint:endPoint,2]))

#    xQuad,res,rank,sv,rcond = np.polyfit(tPXYZ[tenPoint:endPoint,0],tPXYZ[tenPoint:endPoint,2],2,full=True)
#    print('xQuad')
#    print(xQuad)
#    print(((res/((float)(endPoint-tenPoint)))**0.5)/np.mean(tPXYZ[tenPoint:endPoint,2]))
#
#    yQuad,res,rank,sv,rcond = np.polyfit(tPXYZ[tenPoint:endPoint,0],tPXYZ[tenPoint:endPoint,2],2,full=True)
#    print('yQuad')
#    print(yQuad)
```

```
#    print(((res/((float)(endPoint-tenPoint)))**0.5)/np.mean(tPXYZ[tenPoint:endPoint,2]))

    #%%%Getting strain rates

    for i in range(1,DICLength):
        tPXYZ[i,5] = (tPXYZ[i+1,2]-tPXYZ[i-1,2])*fps/2
        tPXYZ[i,6] = (tPXYZ[i+1,3]-tPXYZ[i-1,3])*fps/2
    tPXYZ[0,5] = (tPXYZ[1,2]-tPXYZ[0,2])*fps
    tPXYZ[DICLength-1,5] = (tPXYZ[DICLength-1,2]-tPXYZ[DICLength-2,2])*fps
    tPXYZ[0,6] = (tPXYZ[1,3]-tPXYZ[0,3])*fps
    tPXYZ[DICLength-1,6] = (tPXYZ[DICLength-1,6]-tPXYZ[DICLength-2,6])*fps

    tPXYZ[0:DICLength,5] = signal.savgol_filter(tPXYZ[0:DICLength,5],21,2)
    tPXYZ[0:DICLength,6] = signal.savgol_filter(tPXYZ[0:DICLength,6],21,2)


    #%%%%%%%Plotting
    if(plot):
        #fig,(ax1,ax2) = plt.subplots(1,2)
#        ratio = np.empty(DICLength)
#        for i in range(DICLength):
#            if(tPXYZ[i,2]*tPXYZ[i,3]>0):
#                ratio[i] = tPXYZ[i,2]/tPXYZ[i,3]
        fig,(ax1,ax2,ax3) = plt.subplots(3,1,sharex=True,figsize=fSize) # figure(figsize=fSize)
        #plt.plot(tPXYZ[0:DICLength,0],tPXYZ[0:DICLength,1]*10,label = 'Pressure (bar)')
        ax3.plot(tPXYZ[zeroPoint:DICLength,0],tPXYZ[zeroPoint:DICLength,2],label = 'X')
        ax3.plot(tPXYZ[zeroPoint:DICLength,0],tPXYZ[zeroPoint:DICLength,3],label = 'Y')
        ax3.legend()
        ax2.plot(tPXYZ[zeroPoint:DICLength,0],tPXYZ[zeroPoint:DICLength,4]-tPXYZ[zeroPoint,4],label = 'Apex z
displacement')
        ax2.legend()
        ax1.plot(tPXYZ[zeroPoint:DICLength,0],tPXYZ[zeroPoint:DICLength,1]*10**3,label = 'Membrane Pressure')
        ax1.legend()
        #plt.plot(tPXYZ[0:DICLength,0],ratio,label = 'apex strain ratio')
        #plt.plot(tPXYZ[:,0],tPXYZ[:,4]*10**-1,label = 'Apex z displacement(cm)')
        ax1.set_ylabel(r'Pressure (kPa)')
        ax2.set_ylabel(r'Apex displacement (mm)')
        ax3.set_ylabel(r'Apex stretch ratio')
        plt.xlabel('time(ms)')
        ax1.grid()
        ax2.grid()
```

```
        ax3.grid()
        ax1.grid(which='minor')
        ax2.grid(which='minor')
        ax3.grid(which='minor')
        #fig.tight_layout()

        fig.subplots_adjust(hspace=0)
        fig.suptitle(pName[3:-4])
        #fig.align_labels()
        #plt.title(pName[3:-3])
        #ax1.plot(tPXYZ[0:DICLength,0],tPXYZ[0:DICLength,1]*10,label = 'Pressure (bar)')
        #ax1.plot(tPXYZ[0:DICLength,0],tPXYZ[0:DICLength,2],label = 'Lagrangian x strain')
        #ax1.plot(tPXYZ[0:DICLength,0],tPXYZ[0:DICLength,3],label = 'lagrangian y strain')

    #%%%%Making CSV of Processed data
    f = open(outputName,"w")
    f.write('t(s),P(MPa),Str X,Str Y,Z disp (mm),Str rate X, Str rate Y \n')
    for i in range(zeroPoint,DICLength):
        for j in range(6):
            f.write((str)(tPXYZ[i,j])+',')
        f.write((str)(tPXYZ[i,6])+'\n')
    f.close()
    #print(outputName+'strain ratio: '+(str)(np.average(np.absolute(tPXYZ[:,2]-1))/
np.average(np.absolute(tPXYZ[:,3]-1))))
#%%% Plot chosen datasets
def plotter(fig,name,cols,markers,labels,testNo,colour,plFactor):
    n = len(cols)
    vals = [[] for i in range(n)] #yVals#more efficient to build a big list and then convert to an array
(O(n), rather than dynamically sizing an array (O(sum(range(n)))))
    f = open(name,"r")
    reader = csv.reader(f)
    r = 0
    for row in reader:
        if(r>0):
            c = 0
            j = 0
            for col in row:
                if(c == cols[j]):
                    vals[j].append((float)(col))
                    j+=1
                    if(j==n):
```

```
                        break
                c+=1
        r+=1
    f.close()
    for j in range(1,n):
        fig.plot(np.array(vals[0]),np.array(vals[j])*plFactor[j-1],colour+markers[j-1],label = labels[j-1]+'
'+(str)(testNo))

def plotStats(fig,names,xCol,yCol,colour,lab,multFact):
    nData = len(names)
    x = []
    y = [[]for i in range(nData)]
    pts = np.zeros(nData)
    for i in range(nData):
        f = open(names[i],"r")
        reader = csv.reader(f)
        r = 0
        for row in reader:
            if(r>0):
                c = 0
                for col in row:
                    if(c==xCol):
                        if(i == 0):
                            x.append((float)(col))
                    if(c == yCol):
                        y[i].append((float)(col))
                    c+=1
            r+=1
        f.close()
        pts[i] = r

    length = (int)(np.min(np.min(pts)))
    print('Length:'+(str)(length))
    Y = np.zeros((nData,length))
    for i in range(nData):
        tmp = np.array(y[i])
        Y[i,0:length-1] = tmp[0:length-1]
    mean = np.zeros(length)
    sdev = np.zeros(length)
    minim = np.zeros(length)
    maxim = np.zeros(length)
```

```
    for i in range(length-1):
        minim[i] = np.min(Y[:,i])
        maxim[i] = np.max(Y[:,i])
        for j in range(nData):
            mean[i]+=y[j][i]
        mean[i] = mean[i]/nData
        for j in range(nData):
            sdev[i]+=(mean[i]-y[j][i])**2
        sdev[i] = (sdev[i]/nData)**0.5

    #for i in range(nData):
     #   fig.plot(np.array(x[0:length]),Y[i,0:length-1],colour)
    fig.plot(np.array(x[0:length]),(mean[0:length-1]-sdev[0:length-1])*multFact,colour+'--')
    fig.plot(np.array(x[0:length]),(mean[0:length-1])*multFact,colour,label = lab)
    fig.plot(np.array(x[0:length]),(mean[0:length-1]+sdev[0:length-1])*multFact,colour+'--')
    fig.fill_between(np.array(x[0:length]),(mean[0:length-1]-sdev[0:length-1])*multFact,(mean[0:length-1]
+sdev[0:length-1])*multFact,facecolor = colour,alpha = 0.2)
    print(lab)
    #for i in range(length-1):
    #    print((str)(np.round(x[i],2)))
    for i in range(length-1):
        print((str)(np.round(mean[i],4)))
    #print(mean[0:length-1])

def bfSL(name,xCol,yCol,x0,xEnd,xScale):
    x = []
    y = []
    f = open(name,"r")
    reader = csv.reader(f)
    r = 0
    for row in reader:
        if(r>0):
            c = 0
            for col in row:
                if(c==xCol):
                    x.append((float)(col))
                if(c == yCol):
                    y.append((float)(col))
                c+=1
        r+=1
    f.close()
```

```
X = np.array(x)
Y = np.array(y)
sIndex = 0
eIndex = len(X)
for i in range(len(X)):
    if(X[i]>=xEnd):
        eIndex = i+1
        break
for i in range(len(X)):
    if(X[i]>=x0):
        sIndex=i
        break
print(X[sIndex:eIndex])
print(Y[sIndex:eIndex])
X = X*xScale
slope,intercept,rVal,pVal,stderr = stats.linregress(X[sIndex:eIndex],Y[sIndex:eIndex])
return(slope,rVal**2)
```